

Alma Mater Studiorum – Università di Bologna

DOTTORATO DI RICERCA IN

ASTROFISICA

Ciclo 31

Settore Concorsuale: 02/C1

Settore Scientifico Disciplinare: FIS/05

TITOLO TESI

**NON-THERMAL EMISSION IN THE LOBES OF
RADIO GALAXIES**

Presentata da: Massimo PERSIC

Coordinatore Dottorato
Prof. Francesco R. FERRARO

Supervisore
prof. Gabriele GIOVANNINI

Supervisore esterno
Prof. Yoel REPHAELI
(Tel Aviv U.; U. California, San Diego)

Esame finale anno 2020

SUMMARY

Radio and γ -ray measurements of large lobes of several radio galaxies provide adequate basis for determining whether emission in these widely separated spectral regions is largely by non-thermal (NT) electrons. This is very much of interest as there is yet no unequivocal evidence for a significant component that arises from pion decay following NT proton interactions in the ambient lobe gas. A quantitative assessment of the hadronic yield spectral distribution necessitates full accounting of the local and background radiation fields in the lobes. • Assuming a truncated single-power-law electron energy distribution, exact calculation of the emission by NT electrons in the magnetized plasma in the lobes of Fornax A leads to the conclusion that its γ -ray emission measured by the *Fermi* Large Area Telescope (LAT) can, in fact, be accounted for by energetic electrons scattering off the ambient optical radiation field, whose energy density (which, based on recent observations, is dominated by emission from the central galaxy) is shown here to be higher than previously estimated; this result considerably weakens earlier conclusions on the hadronic origin of the emission measured by *Fermi*-LAT. • Results of similar analyses of the measured radio, X-ray and γ -ray emission from the lobes of Centaurus A, Centaurus B, and NGC 6251 confirm that the measured γ -ray emission from these lobes, too, can be accounted for by Compton scattering of the radio-emitting electrons off the superposed radiation fields in the lobes. In detail, the *Fermi*-LAT measured emissions are dominated by Compton/EBL in Cen A, by Compton/(EBL+GFL) in Cen B, by Compton/GFL in Fornax A, and by Compton/CMB in NGC 6251. The sectionalized SED modeling of each lobe of Cen A reveals a spectral evolution from the inner to the outer regions in the form of an outwardly increasing magnetic field and high-energy EED truncation (the EED spectral index remains constant). • Measured emissions of distant ($D_L > 125$ Mpc) radio-galaxy lobes are currently limited to the radio and X-ray bands, hence give no information on the presence of NT protons but are adequate to describe the properties of NT electrons. Modeling lobe radio and X-ray emission in 3C 98, Pictor A, DA 240, Cygnus A, 3C 326, and 3C 236 in the same way as we did for the previous sources, the properties of intra-lobe NT electrons are fully determined and the level of the related γ -ray emission from Compton scattering of the electrons off the CMB, EBL, and the source-specific radiation fields, are calculated. The estimated γ -ray emission in the relatively dense plasma in the lobes of Cygnus A indicate that, depending on the NT proton content in the lobes, pion-decay may yield a potentially detectable $\gtrsim 0.1$ GeV flux. • The electron-to-magnetic energy density ratios emerging from the spectral analyses presented in this thesis are in the range $u_e/u_B \sim \mathcal{O}(1-100)$, suggesting the NT energy budget to be particle-dominated in most lobes. The energy density of NT protons, u_p , is constrained by spectral considerations in the γ -ray band to be less than a few tens of eV cm^{-3} . Despite this limit, arguably $u_p \gg u_e$ – as suggested by arguments of electric neutrality of the lobe NT plasma at injection, and of lobe internal vs. external pressure. Thus the lobes' NT energy budget is suggested to be dominated by particles. Furthermore, given the low thermal energy densities, u_{th} , measured in lobes, the condition $u_B + u_e + u_p > u_{th}$ (i.e., NT energy dominance), is probably a general feature of lobe energetics. This may reflect the fact that, given the highly non-equilibrium phenomenon of AGN jets that inflate the lobes, the latter's evolution is very different from that of older galactic systems (e.g., clusters of galaxies) that have attained a state of equilibrium where thermal energy contrasts gravitation and dominates the internal energy budget.

CONTENTS

1. INTRODUCTION

1.1 Particles outside galaxies	1
1.2 Jets	2
1.2.1 Jet dynamics and energetis	2
1.2.2 Particle acceleration in jets	3
1.2.3 Jet emission	4
1.3 Lobes	5
1.3.1 Radiative properties of lobes	6
1.3.2 Scheme of lobe SED modeling	7
1.3.3 Magnetic field	8
1.4 Status of knowledge on NT emission in lobes before this thesis	8
1.5 Plan of this thesis	9
References	9

2. NT EMISSION IN THE LOBES OF FORNAX A

2.1 Introduction	11
2.2 Observations of NT emission from Fornax A	11
2.2.1 Optical radiation fields in the lobes	12
2.3 NT emission in the lobes	15
2.3.1 Radiative yields of electrons and positrons	15
2.3.2 Pion decay yields	15
2.4 Modelling the lobe SED	17
2.5 Discussion	18
References	20

3. NT EMISSION IN THE LOBES OF CENTAURUS A, CENTAURUS B, AND NGC 6251 A

3.1 Introduction	21
3.2 Lobe SED measurements	21
3.2.1 Cen A	21
3.2.2 Cen B	22
3.2.3 NGC 6251	23
3.3 Radiation fields in the lobes	23
3.4 Modeling NT emission in the lobes	25
3.4.1 Synchrotron and Compton yields	25
3.4.2 Upper limits on proton contents in lobes: the case of Cen A	27
3.4.3 On a jet origin of NT electrons in lobes: the case of Cen A	27
3.5 Discussion	29
3.6 Conclusion	30
References	30

II

4. NT EMISSION IN THE LOBES OF 3C 98, PICTOR A, DA 240, CYGNUS A, 3C 326, AND 3C 236

4.1 Introduction	31
4.2 Emission and radiation fields in the lobes	31
4.2.1 Observations of NT emission	31
4.2.2 Radiation fields	32
4.3 Modeling lobe NT emission	34
4.4 Discussion	35
4.5 Conclusion	37
References	38

5. CONCLUSION

5.1 Discussion	39
5.1.1 Electrons	39
5.1.2 Radiation fields	39
5.1.3 Protons	39
5.1.4 Magnetic fields	40
5.1.5 Energy densities	40
5.1.6 Accuracy of results	40
5.2 Summary	41
5.3 Outlook	41
References	42

Non-thermal emission in the lobes of radio galaxies

1 CHAPTER 1. INTRODUCTION

This thesis deals with the non-thermal (NT) emission in lobes of radio galaxies. I examine the spectral energy distribution (SED) of the radiation emitted by such sources and model the astrophysical environments in which relevant radiation processes take place. Although the lobes studied here were studied by different authors in the past (usually, the groups who published the original data), my approach will be based on a uniform treatment for all sources, in which I will carry out exact calculations of all relevant radiative yields.

This introduction serves the purpose of putting the thesis subject into perspective. After a prefatory section on how relativistic particles may leave their source sites in galaxies, a summary is given of our current knowledge and understanding of jets and lobes of radio galaxies. This summary is largely based on recent extensive review papers by Blandford, Meier & Readhead (2019) and Krawczynski, Böttcher & Reimer (2012), and will touch upon those aspects (jet mechanical and radiative properties, particle acceleration) that are most relevant to our subject matter and the original results contained in this thesis.

1.1 Particles outside galaxies

The SED of the radiation emitted by energetic particles outside their galactic sources are important for determining basic properties of the particle populations and for assessing the impact of particle interactions in the magnetized plasma of galactic halos and galaxy clusters.

Particles can be carried away from their galactic sources by convection (that includes submechanisms of diffusion and advection) and jets. To frame the concept of convection, let's start from the simplest form (no source term and no collision/decay and cascade loss terms) of the continuity equation (Ginzburg & Syrovatskii 1964: see Eq. 9.1 of Gaisser 1990) for the particle number density $n(\mathbf{r}, t, E)$ and its current $\mathbf{j}(\mathbf{r}, t, E)$, i.e. $\partial n/\partial t = -\vec{\nabla} \cdot \mathbf{j}$, where $\mathbf{j} = -\vec{\nabla}(Dn)$ with D the diffusion coefficient (Fick's law). Developing the gradient, we obtain a (non-directional) diffusion term and a (directional) advection term: $\mathbf{j} = -D\vec{\nabla}n - n\mathbf{u}$, with \mathbf{u} the particle velocity. So the continuity equation becomes $\partial n/\partial t = \vec{\nabla}(D\vec{\nabla}n) + (\vec{\nabla}\mathbf{u})n$. The diffusion coefficient, $D \sim \lambda_D u$ where λ_D is the diffusion mean free path (i.e. the length between particle scatterings off magnetic fluctuations), is usually parameterized as $D(E) = D_0 E^\delta$ where $D_0 \sim 10^{28} \text{ cm}^2 \text{ s}^{-1}$ and $\delta \sim 0.6$ (in the Galaxy; see section 9.3.4 of Gaisser 1990).

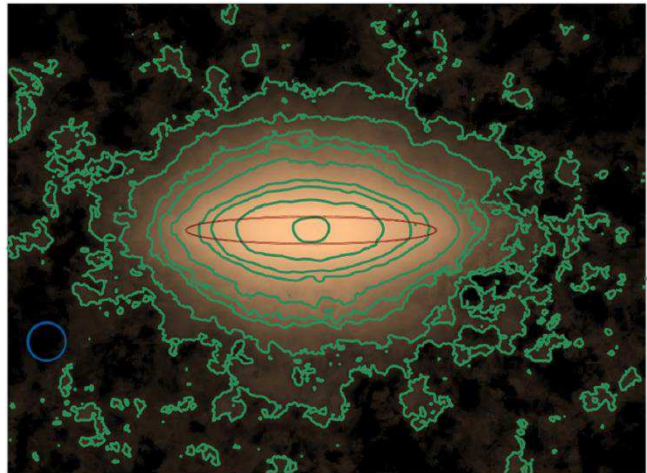


Figure 1. Radio continuum image of a median edge-on disk galaxy, resulted from stacking data for 30 individual galaxies. The red ellipse represents the disk extent, whereas the blue circle represents the average beam of the 30 galaxies. This "typical" disk galaxy is surrounded by a halo of magnetic fields and relativistic particles. (Reproduced from Fig. 6 of Wiegert et al. 2015).

If convection is isotropic ($\mathbf{u} = 0$) only diffusion is effective: over timescales $t_{\text{diff}} = h_z^2/D$ particles diffuse out of the disk (of semi-thickness h_z) and form a halo that, in the presence of a magnetic field, can be revealed through the synchrotron radiation it emits. This radiation is relatively faint in individual normal galaxies (i.e. galaxies of moderate star formation, like our own Milky Way) so co-addition of several galaxies is currently needed to reveal such radiation (Fig. 1; Wiegert et al. 2015). If convection is anisotropic ($\mathbf{u} \neq 0$) an advective gas flow (galactic wind) may develop in addition to the ongoing background diffusion: a well-known case of a galactic-wind galaxy is M 82 (Fig. 2).

Electrons such as those shining in the halo of the co-added galaxy in Fig. 1 are subject to Coulomb, bremsstrahlung, synchrotron, and Compton energy losses because they interact with (thermal) gas, magnetic fields, and photons associated with starlight and the Cosmic Microwave Background (CMB). A full-fledged diffusion model, based on a semi-analytical approach that accounts for all energy losses suffered by electrons and protons diffusing out of a star-forming galactic disk into the halo, was recently presented by Rephaeli & Sadeh (2019): it correctly models and predicts levels and spatial profiles of radio, X-ray, and γ -ray emission in the halos of two edge-on star-forming galaxies, NGC 4631 and NGC 4666. A simpler case – electrons subject to synchrotron-Compton losses diffusing into the



Figure 2. The starburst galaxy M82 (NGC 3034). An advective gas flow perpendicular to the disk is clearly seen.

Galactic halo with an energy-independent diffusion coefficient, $D = D_0$ – was analytically solved in a seminal paper by Syrovatki (1959). Exact analytical solutions describing the steady-state transport of relativistic electrons subject to diffusion, advection, and radiation losses perpendicular to a galactic plane are due to Lerche & Schlickeiser (1980).

In spite of the ubiquitousness of convection, the most effective way to transport particles orders of magnitudes farther out in distance from their sources is provided by jets. Jets are collimated flows of particles and electromagnetic energy that are formed when the black hole (BH) sitting in the galaxy center spins and the accretion disk is strongly magnetized; they are collimated close to the BH by magnetic stress associated with a disk wind. High-power jets can emerge from their galactic nuclei in relativistic, supersonic, particle-dominated states, and terminate in strong shocks that are revealed as “hot spots” in radio maps (see Section 1.3); lower-power jets are degraded to buoyant plumes and bubbles. Jets may accelerate protons to EeV energies which contribute to the CR spectrum and which may initiate pair cascades that can efficiently radiate synchrotron γ rays. Jets can affect their environments, stimulating and/or limiting the growth of galaxies.

1.2 Jets

Longitudinally, jets typically span three size scales.

(i) BH jets extend from the BH gravitational radius, $r_g = GM/c^2$, to the BH influence radius, $r_{\text{infl}} = 3GM/\sigma^2$ (where $\sigma \sim 300 \text{ km s}^{-1}$ is the central stellar velocity dispersion, e.g. Ferrarese & Merritt 2000; this implies $r_{\text{infl}} \sim 3 \cdot 10^6 r_g$) which measures the distance at which the potential changes abruptly and from which gas can accrete onto the BH. Jet collimation and acceleration (to apparently superluminal speeds) probably occurs over distances $\sim 10^{5-6} r_g$, i.e. relatively far away from the BH but still in this phase: in Virgo A (M87) the bright knot HST-1 probably marks r_{infl} . Still in M87, the jet section is parabolic in this phase, from at (at least) $6r_g$; in this region the jet shows limb brightening, and hence evidence of spine/sheath structure (see Section 2.3.1)

down to this scale (Kim et al. 2018). In 3C 84, however, the BH jet appears to have a uniform width from near the core region to $\sim 10^4 r_g$ (Giovannini et al. 2018).

(ii) Galaxy jets are the outward extension of the BH jets into the dynamical environment set by the stellar and dark matter potential within the host galaxy. In this phase jets have a fixed opening angle, i.e. their section is conical. In the M87 jet, an outer mildly relativistic velocity component (the “sheath”) and an inner faster component (the “spine”) are clearly seen (Mertens et al. 2016).

(iii) Lobe jets are the outermost extension of jets, from $\sim 0.1 r_{\text{lobe}}$ to r_{lobe} , where the latter measures the maximum radial extent of the jet or lobe.

These scales are nicely exemplified in the nearby source Virgo A (hosted in the elliptical galaxy M87) whose approaching jet points at 17° away from our line of sight so its longitudinal development can be observed, whereas its receding jet (pointing in the opposite direction) is dimmed, by relativistic beaming effects, to inobservability soon after its launch. A detailed VLBI study of the innermost M87 jet (Walker et al. 2018), based on 50 VLBA 43 GHz observations with spatial resolution $60 \times 120 r_g$ taken over 17 years, shows that: (i) an asymmetric jet and counter-jet exist in the inner 0.12 pc (for an assumed distance of 16 Mpc); (ii) jet and counter-jet are both edge brightened; (iii) both jets show an early fast widening followed by a narrowing and then a second widening, at which point the counter-jet fades to invisibility; (iv) the jet gets collimated; (v) proper motions and intensity ratios of the jet and counter-jet (as long as the latter is seen) indicate acceleration from apparent velocities $< 0.5c$ to $> 2c$; (vi) the measured polarization suggest a helical magnetic field close to the core. Fig. 3 shows a montage of the FR-I radio galaxy Virgo A (M87) on scales from near the central super-massive BH (SMBH; right) to the outer lobes (left).

Radially, a spine/sheath layer structure is suggested also by the statistics of jets that are γ -ray bright and radio bright, if the faster inner spine is predominantly γ -ray emitting and the slower outer sheath is predominantly radio emitting; there is in fact no correlation between the radio-measured speed of the jet and *Fermi*/LAT γ -ray detection (Karouzos et al. 2011).

In general, in the radio band higher-frequency emission is located closer to the BH than lower-frequency emission. However, as only VLBI offers milli-arcsec resolution, knowledge of the relative locations in different frequency bands relies on source variability. A number of studies have suggested that the γ -ray regions are either close to the radio-emitting regions (Jorstad et al. 2001; Marscher et al. 2011; Jorstad & Marscher 2016; Rani et al. 2018) or closer than the radio regions to the BH (Richards et al. 2011; Max-Moerbeck et al. 2011; Fuhrmann et al. 2014). In the latter case the spine/sheath model may not be viable, and a different source of target photons for Comptonization should be identified (Nalewajko et al. 2014).

1.2.1 Jet dynamics and energetics

It is mainstream opinion that SMBHs exist at the centers of virtually all massive galaxies with a significant bulge (Kormendy & Ho 2013; Heckman & Best 2014). For example,

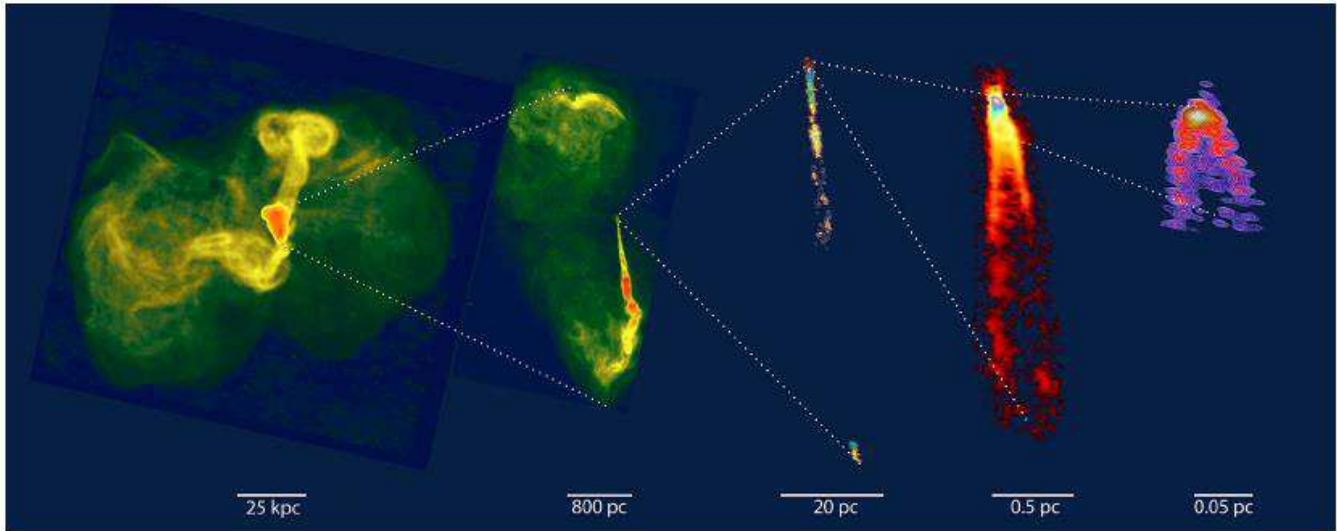


Figure 3. A montage of the FR-I radio galaxy Virgo A (reproduced from Fig. 1 of Blandford et al. 2019), on scales from near the SMBH to the outer lobes. From right: (1) the jet launching region near the SMBH, (2) the innermost jet, (3) the BH jet (including HST-1 at r_{infl} , at the bottom), (4) galaxy jet and inner lobes, (5) lobe jet and outer lobes (showing the current burst, and an older one perpendicular to it). The various size scales are indicated. For more information see Blandford et al. (2019).

M 87 famously harbors a $6.5 \cdot 10^9 M_{\odot}$ SMBH (Akiyama et al. 2019a) whose shadow was recently imaged (Akiyama et al. 2019b). Gas from the outer galaxy will somehow get close to the SMBH – gas coming from a merger with another gas-rich galaxy, from the galaxy’s own interstellar medium, from stars and SN, from the tidal disruption of stars that get inside the SMBH tidal radius. Irrespective of the gas initial angular momentum, if the SMBH spins fast enough the gas will tend to settle near the SMBH on the the latter’s equatorial plane, forming an accretion disk.

When the gas surrounding the SMBH can cool on the inflow timescale it will form a thin accretion disk in the hole’s equatorial plane with an inner radius $r > r_{\text{ISCO}}$, where r_{ISCO} is the innermost stable circular orbit. (The latter shrinks from $9r_g$ to r_g when $j \equiv J/(GM^2/c)$ increases from -1 to $+1$; Meier 2012). Gas spirals inwards under magnetic torques (related to the differential rotation of the gas in the disk), and finally falls towards the event horizon within r_{ISCO} . However, if the accretion rate is higher than the Eddington rate, $\dot{M}_{\text{Edd}} = 4\pi GM_{\text{BH}} m_p / (\sigma_T c)$, the gas can not cool and radiation is trapped by the inflowing gas and radiation pressure puffs the disk into a torus that can create a funnel which may be responsible for the initial collimation of the jet (Abramowicz & Fragile 2013).

A jet shooting from a spinning accreting SMBH can be formed in two ways: through the disk or the BH itself. The former involves the presence of a magnetohydrodynamical wind that can remove angular momentum and energy (Blandford 1976; Lovelace 1976). The latter involves extracting the spin-associated fraction (Penrose 1969) of the BH power (Blandford & Znajek 1977). If the disk is geometrically thin, optically thick, with hot ionized plasma supported by gas pressure, and opacity given by free-free absorption (Shakura & Sunyaev 1973), the disk jet luminosity and the hole jet luminosity are, respectively, $L_j^d \sim 0.5 L_{\text{Edd}} \dot{m}^2$ and $L_j^h \sim 0.5 L_{\text{Edd}} \dot{m}^2 j^2$ for \sim Eddington accretion rates (Meier

2012). Simulations confirm that faster spinning BH produce more jet power (e.g. McKinney 2006). For a fast spinning SMBH of mass of $\sim 10^8-10^{10} M_{\odot}$, accreting at $\dot{M} \sim 0.5 \dot{M}_{\text{Edd}}$, both mechanisms can generate jet powers of $L_{\text{jet}} = 10^{45-47} \text{ erg s}^{-1}$. Over timescales $\Delta t = 10^7 \text{ yr}$, such a jet can pump 10^{59-61} erg into the lobes. Once launched, jets are confined and collimated in different ways at different radii. They may be initially confined by the walls of the funnel formed by an ion-supported torus, i.e. the radiation-puffed-up accretion disk. However, such tori may be not ubiquitous, and in any case collimation is observed to take place at large distances as well. A gasdynamical disk wind may confine the the BH jet close to the hole (Globus & Levinson 2016), whereas if the wind is hydromagnetic then the jet may carry an axial current that supports a toroidal magnetic field outwards of some transition radius (Levinson & Globus 2017). Eventually, at large distances (the ”galaxy jet” region) there will be a return current and the outward magnetic stress will be balanced by gas pressure (Begelman et al. 1984). In FR-II lobes jets are probably confined by the back flow of the jet plasma that has passed through the hotspot shock.

1.2.2 Particle acceleration in jets

Once jets are broadly understood in terms of their mechanical properties, we must still understand where and how do particles get accelerated, and how and where are they transported to cool. The range of electron energy involved are $\sim 100 \text{ MeV}$ to explain self-absorbed and low-brightness radio cores up to $\sim 100 \text{ TeV}$ to explain synchrotron and X-ray luminosities (e.g. Ghisellini et al. 2010; Tavecchio et al. 2010). Distributed acceleration along the jets is required because radiative and adiabatic cooling would cause the jet surface brightness to fall with galactocentric radius much faster than observed.

Given the high photon density, protons in jets can un-

dergo photo-pion production through $p\gamma$ interactions. The resulting pairs may eventually take up all the proton energy. Protons, however, if they outnumber positrons (and hence are in substantial number equality with electrons), acquire roughly the same energy as electrons while they can be accelerated to much higher final energies because their radiative losses are lower. So jet protons would eventually be injected into the lobes.

Diffusive shock (Fermi-I) acceleration (involving repeat reflections by magnetic mirrors) to high Mach numbers has often been invoked as the primary particle acceleration mechanism in jets, hotspots, and lobes. This mechanism is known to be very efficient in SNR and at planetary bow shocks. In its simplest version, a planar shock with compression ratio r transmits a downstream power-law (PL) distribution function with index $3r/(r-1)$ (in momentum): a strong shock, $r = 4$, leads to an accelerated particle spectrum with index 2 (in energy), which can produce synchrotron or Compton PL spectra with index 0.5 (e.g., Gaisser 1990). Shocks can accelerate to high energies because a non-linear amplification of the local magnetic field is created at the shock front by the dynamical reaction of the accelerating particles on the shock (Amato & Blasi 2005, 2006).

Relativistic reconnection of magnetic field lines occur in axisymmetric relativistic jets confined by toroidal magnetic fields, which are prone to non-axisymmetric kink instabilities that can force oppositely directed field lines together so they reconnect by exchanging partners (e.g. Begelman 1998). This process will occur in many relatively small regions where ohmic dissipation balances flux freezing. Relativistic reconnection can be very efficient in converting magnetic energy (measured in the jet frame) into ultra-relativistic particles (Sironi & Spitkovski 2014).

Shock and magnetic-reconnection acceleration are associated with surfaces. As to the former, some dynamical features where both fields and particle densities are expected to be high should be observable: e.g., the "knots" in the M 87 jet and the hotspots in FR-II lobes (e.g. Pictor A, see Perley et al. 1997) are plausibly shocks. As to the latter, continuous emission along/across jets and lobes can be observed if electrons don't cool on the (shorter of) flow and propagation timescales. Shocks and reconnections should be distinguishable through X-ray polarimetry (Tavecchio et al. 2018).

Stochastic (Fermi-II) acceleration are due, most likely, to scattering by plasma waves and turbulence (PWT). Electric fields arising from magnetic reconnections may locally produce an unstable particle momentum distribution which will produces PWT that can then accelerate particles (e.g., Chen et al. 2015). Shear particle acceleration always entails stochastic Fermi-II acceleration (Liu et al. 2017). Initial acceleration by turbulence (coming from, e.g., dissipation of the jet's bulk energy; Wang 2002) of background particles followed by subsequent shock acceleration may have attractive features (Petrosian 2012) and may facilitate the whole process of particle energization (Liu et al. 2017).

1.2.3 Jet emission

Typical jet emission famously has a two-humped shape (see Fig. 4). The low-frequency hump is interpreted as electron synchrotron emission, whereas the high-frequency hump is most commonly – i.e., in the (prevailing) leptonic models

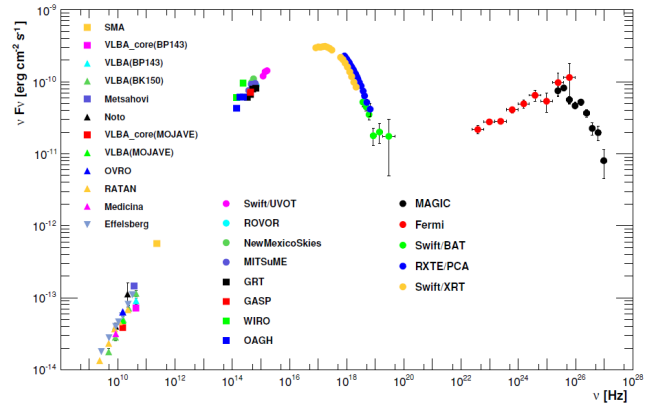


Figure 4. The broad-band SED of Mrk 421. For symbols, references, and further information see Abdo et al. (2011).

– interpreted as Compton scattering of synchrotron photons (in low-luminosity sources) or external-disk and BLR¹ photons (in higher-luminosity sources) off the radio-emitting electrons.

1. Leptonic models

The simplest, one zone, version of leptonic jet models assumes that both humps originate from a single emitting region (Maraschi et al. 1992), possibly associated with r_{inff} where a recollimation shock may form (Marscher 2014). In essence, this model involves one relativistically moving (bulk Lorentz factor Γ) spherical (radius R) emitting region of magnetized (field strength B) NT plasma, that contains electrons distributed in energy according to a single, or variously modified, truncated power law; these emit radiation by synchrotron and Compton mechanisms at, respectively, radio/optical and X/ γ -ray frequencies. Target photons for the latter include the synchrotron photons produced inside the blob by the very scattering electrons (synchrotron-self-Compton, SSC, model), and the photons produced outside the blob by various sources, e.g. the Broad Line Region and the CMB (external-Compton, EC, model). The SSC model is described by, e.g., Tavecchio et al. (1998), Kino et al. (2002), Tavecchio & Maraschi (2003). EC models may use different seed photons, from direct accretion disk emission (Dermer et al. 1992, 1997), IR dust emission (Blazewski et al. 2000; Arbeiter et al. 2002), the CMB (Harris & Krawczynski 2002), the BLR (Sikora et al. 1994; Blandford & Levinson 1995; Ghisellini & Madau 1996) – or from a superposition of various such photon fields (Ghisellini & Tavecchio 2009). More elaborate EC models invoke variations along or across the jet, e.g. the longitudinally decelerating model (Georganopoulos & Kazanas 2003) and the transversely structured spine/sheath model (Ghisellini et al. 2005).

2. Hadronic models

A more complex class of jet models involves protons that

¹ The Broad Line Region (BLR), where broad optical/UV emission lines are produced, is located close to the accretion disk, usually outside the line of sight to the nucleus, and its outer edge is delineated by the dusty/molecular torus (e.g., Czerny & Hryniewicz 2011).

contribute to the SED (lepto-hadronic models). As a general characteristic, hadronic jet models account for all leptonic processes related to the presence of electrons (and positrons) in the emission region: however, for high B strengths, all Compton processes are suppressed and proton-initiated radiation components dominate high-energy emission.

Various considerations suggest that jets may be energetically and dynamically dominated by protons (Ghisellini et al. 2014). This is deduced from limits on the electron (and positron) contents of jets deduced from the lack of soft-X-ray excesses (Sikora & Madejski 2000) and from the insight gained from leptonic models of knots and blazars (Celotti & Ghisellini 2008): the power in Poynting flux and in relativistic electrons is not sufficient to support the observed power of jets and radio lobes. Furthermore, radio lobes and X-ray cavities in galaxy clusters (interpreted as expanding bubbles from radio sources) require a significant pressure component, in addition to that of energetic electrons and magnetic fields, in order to overcome thermal intracluster gas pressure (e.g. Wilson et al. 2006; Wykes et al. 2013). Furthermore the highest energies detected in cosmic-ray protons, $E_p \sim 10^{20}$ erg, are consistent with the maximum attainable energy by protons that are confined in an acceleration region of radius r and magnetic field B , i.e. $E_p^{max} < 3 \cdot 10^{19} (B/10 \text{ G}) (R/10^{16})$ (Hillas 1984), with values of r and B scaled to their typical values in one-zone SSC models. Also, a striking similarity has been pointed out between the energy fluxes of diffuse γ rays above 100 MeV and cosmic-ray (CR) protons above $10^{15.5}$ eV (the "ankle" in the CR spectrum): this similarity is interpreted as favoring the presence of ultrarelativistic protons in blazar jets, that ultimately produce γ rays through hadron-initiated cascades (Mannheim 1995).

Protons may interact with target photons or matter to produce secondary particles, if their energy exceeds (in the plasma frame) the corresponding particle production threshold: 0.145 GeV for photo-meson production, and 1.22 GeV for inelastic pp interactions, that ultimately lead to the creation of γ -ray photons from π^0 's and e^\pm pairs from π^\pm 's. The latter, owing to the low σ_{pp} , requires high ambient densities to be a dominant emission mechanism – but short-time variability may be a problem (Atoyan & Dermer 2003; Beall & Bednarek 1999; Pohl & Schlickeiser 2000). In radiation-dominated jets, $p\gamma$ interaction rates dominate over pp interaction rates (above the respective thresholds). To accelerate protons to high energies, $B \sim \text{several} \times 10 \text{ G}$ are needed: in such intense fields protons, in addition to electrons, radiate by synchrotron mechanism (Aharonian 2000; Mücke & Protheroe 2000). Particle-photon interactions in hadronic models include photo-meson production and Bethe-Heitler pair production for protons, and Compton scattering of pairs off jet-internal synchrotron photons (Mannheim & Biermann 1992; Mücke & Protheroe 2001; Mücke et al. 2003), jet-external photons such as optical accretion-disk radiation – either direct (Bednarek & Protheroe 1999) or BLR reprocessed (Atoyan & Dermer 2003) – or IR dusty-torus radiation, and the CMB. For high B fields, the produced pions and muons will radiate synchrotron radiation up to energies higher than the proton synchrotron component (i.e. the typical synchrotron frequency, $\nu_s \propto ZE^2/m^3$ with usual meaning of symbols), although often at a fainter level. Pions decay into γ rays, e^\pm , and neutrinos. For high initial proton ener-

gies, the produced secondary particles are also energetic, so the emission region is optically thick to π^0 -decay γ rays and to secondary-produced synchrotron and Compton photons: so an e^\pm -pair cascade develops that redistributes energies from higher to lower energies.

One-zone hadronic models have more parameters than their leptonic counterparts: the energy distributions of protons and primary electrons (both with normalization, spectral index, and high/low-end truncation energies), and the integral properties of the emitting region (magnetic field, radius, bulk Doppler factor). The resulting SED consists of several contributions. For $B \sim \text{several} \times 10$ gauss, the high-frequency hump is mostly due to proton and muon synchrotron radiation (the higher B , the stronger the former contribution) with additional contributions from cascades initiated by secondary e^\pm pairs and π^0 -decay photons (Mannheim 1993), whereas the low-frequency hump is electron synchrotron radiation – that provides the main target photons for photo-meson production and the cascading for most model applications. For lower B , proton and meson synchrotron emission become less important and Compton- and synchrotron-supported pair cascades must be considered (Atoyan & Dermer 2003). If the jet-external BLR radiation provides most of the target photons, the pion production threshold can be reached by lower proton energies because the BLR photons are blue-shifted by a factor Γ (the emitting region's bulk Lorentz factor) in the jet frame (Atoyan & Dermer 2003). If the emitting region is close to the accretion disk, the latter's emission may provide the dominant target photon field (Protheroe 1997; Bednarek & Protheroe 1999) that will similarly be blue-shifted in the jet frame; on the contrary, if the emitting region is far from the disk, the latter's photons will reach the former from behind hence will be red-shifted by $\sim \Gamma^{-1}$ in the jet frame: this means a factor $\sim \Gamma^2$ higher proton energy requirement w.r.t. the case of a dominant BLR radiation target field (if the emitting region is within the BLR boundary) to reach the threshold energy for photo-pion production.

1.3 Lobes

Jets may create lobes. These are the most striking large-scale structures observed in radio galaxies. They are double, usually symmetrical, ellipsoidal or circular (in sky projection), located on both sides of the active nucleus. Based on the morphology of their large-scale emission, radio sources appear to be of two types, FR-I and FR-II (Fanaroff & Riley 1974), depending on whether the lobes are brightest in the center or at the edges. (The former/latter have lower/higher luminosity.) FR-I's have bright jets linking the radio core to the lobes (e.g. Fornax A, Centaurus A, Pictor A), whereas FR-II's have faint jets but bright hotspots at the far boundaries of the lobes (e.g., Cygnus A, NGC 6251). Piecing this information together, FR-I's radiate their energy efficiently as they cross the lobes, whereas FR-II's can transport their energy to the end of the lobes. FR-I jets decelerate close to the nucleus where their radio (synchrotron) emission is brightest, whereas FR-II jets remain relativistic across the lobes to their ends, where the observed hotspots arise from the shocks formed when the fast jet abruptly terminates at the end of the source. So the FR-I/FR-II transition likely reflect the jet's ability to propagate through the host galaxy

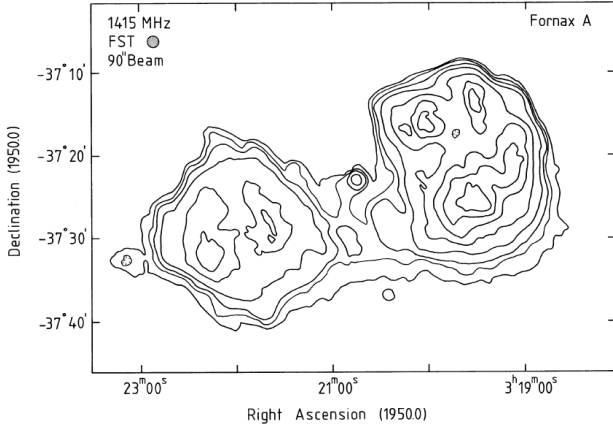


Figure 5. The FR-I radio galaxy Fornax A with its lobes: contours indicate the 1.4 GHz brightness distribution. (Reproduced from Fig. 1 of Ekers et al. 1983.)

without being slowed down to sub-relativistic speeds by interaction with the interstellar medium. Furthermore, FR-I jets at ~ 30 kpc transition from a super-linear to linear expansion and their magnetic fields transition from axial to toroidal, and show a velocity increase across the jet (sheath/spine structure).

Radio lobes are the interface through which AGN jets may influence their environments. Specifically, radio lobes located in galaxy clusters may be primary sources of relativistic particles into the intracluster medium. Knowledge of these distributions is generally quite limited and is based largely on just radio observations. Measurements of NT X-ray and more recently also γ -ray emission from the extended lobes of several nearby radio galaxies provide, for the first time, a tangible basis for detailed modeling of the spectral distributions of energetic electrons and protons in the lobes.

Sampling their emitted radiation SEDs over these spectral regions can by itself, even with only limited spatial information, yield important insight on the emitting electrons and possibly also on energetic protons whose interactions with the ambient plasma may dominate the observed ~ 100 MeV emission (from the decay of neutral pions). In addition to the intrinsic interest in physical conditions in radio lobes, modeling energetic particles and their emission processes can yield important insight also for the origin of these particles in galaxy clusters.

1.3.1 Radiative properties of lobes

The radio emission is electron synchrotron emission, as inferred from its very smooth broad-band nature (e.g., Ekers et al. 1983) and strong polarization (Saikia & Salter 1988), from relativistic electrons (with Lorentz factors up to $\gamma_{max} \sim 10^{5-6}$) moving in a tangled magnetic field. This plasma must also contain protons (and/or positrons) to balance the electrons and achieve charge neutrality. Assuming the electron energy distribution (EED) to be power-law (PL) in γ (the electron Lorentz factor), i.e. $N(\gamma) = N_{e0}\gamma^{-q_e}$ for $\gamma_{min} \leq \gamma \leq \gamma_{max}$ with $q_e = 2\alpha + 1$ where α is the radio spectral index, the synchrotron emissivity is $j_s \propto N_{e0}B^{(q_e+1)/2}$ (e.g. Tucker 1975), therefore radio emission alone can not

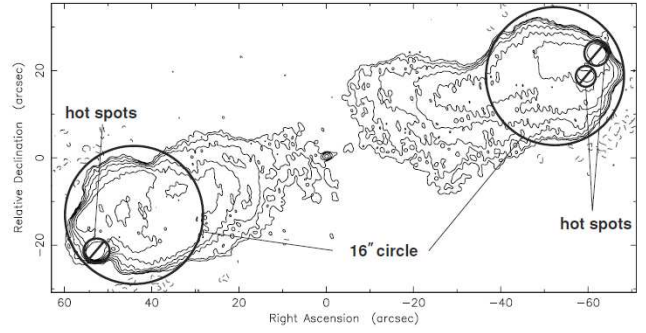


Figure 6. The FR-II radio galaxy Cygnus A: contours indicate the 1.3 GHz brightness distribution. Barred circles indicate hotspots at the lobes' far boundaries. (Reproduced from Fig. 4 of Yaji et al. 2010.)

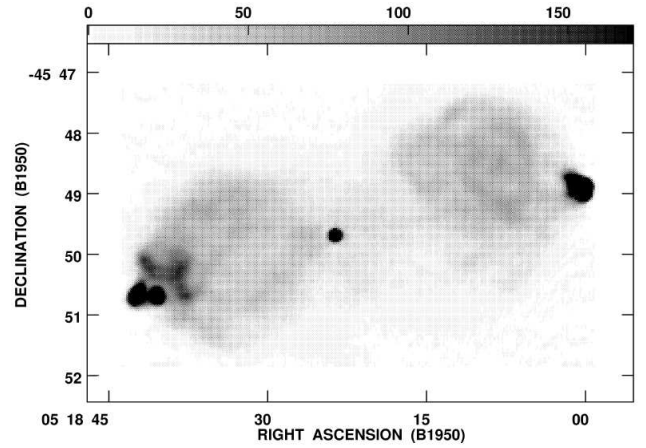


Figure 7. The FR-II radio galaxy Pictor A with its lobes: contours indicate the 20 cm brightness distribution at $7''.$ Hotspots at the lobes' far ends are clearly visible. (Reproduced from Fig. 3 of Perley et al. 1997.)

give both N_{e0} and B . Energetic electrons, in addition to emitting synchrotron radiation in the presence of a magnetic field, if immersed in a radiation field of characteristic frequency ν , Compton upscatter the associated photons to an energy $\nu_1 \sim \gamma^2\nu$. The ubiquitous CMB radiation field peaks at $\nu_{CMB} = 160.4$ GHz, so the corresponding peak Compton/CMB photon energy is $h\nu_{1C} \sim 0.1-10$ MeV for $\gamma \sim 10^{4-6}$. Photon energies ~ 1 keV, in the X-ray domain, are easily produced by Comptonization of CMB photons by an EED with the above-mentioned γ_{max} . Given the target photon field (the CMB Planckian) and the EED, the Compton emissivity is $j_c \propto N_{e0}$. Then combined X-ray and radio observations can in principle solve the electron-density vs. magnetic-field degeneracy and deliver N_{e0} and B separately.

Compton scattering is not restricted to CMB photons. An isotropic field of target photons is also provided by the Extragalactic Background Light (EBL). The EBL contains direct (UV/optical) and dust-reprocessed (IR) starlight, integrated over the star formation history of the universe: reflecting those two components, the EBL SED has a Bactrian shape and shows an optical hump and an IR hump. A recent updated model, based on accurate galaxy counts in several spectral bands, is presented by Franceschini & Rodighiero

(2017). Photons from the optical hump, with typical energy $\epsilon \sim 1$ eV, get Compton upscattered to $\epsilon \sim 0.1$ GeV by electrons with $\gamma = 10^4$. So, the radio emitting electrons in the lobes can upscatter CMB photons to X-ray energies and EBL photons to γ -ray energies. The CMB is known with far greater precision than the EBL, so N_{e0} is best derived from modelling X-ray data as Comptonized CMB emission than from modelling γ -ray data as Comptonized EBL emission. An anisotropic field of target photons is provided by the Galaxy Foreground Light (GFL) that arises from the elliptical host galaxy, whose SED usually shows two thermal humps, IR and optical.

The scheme of calculation used to construct the lobe SED models that will be presented in the next chapters, just hinted at in the preceding paragraphs, is more clearly outlined in the next section.

1.3.2 Scheme of lobe SED modeling

In a textbook-clear case, well exemplified in this thesis by Fornax A (Chapter 2), the steps to determine the particle energy distributions and the magnetic field can be outlined as follows.

(i) Each lobe is modeled as a sphere of radius r_{lobe} ; the (projected) distance from the lobe's nearest boundary to the host galaxy center is d (see Fig. 10 in Chapter 2). The lobe is located at a luminosity distance D_L . Once the emitting volume and its distance from the observer are known, spectral emissivities can be converted into spectral fluxes to be compared with data.

(ii) An EED is assumed in the form of a time-independent, isotropically distributed, truncated-PL distribution in the Lorentz factor γ , i.e.

$$N_e(\gamma) = N_{e,0} \gamma^{-q_e} \dots \gamma_{\min} < \gamma < \gamma_{\max} \text{ cm}^{-3}, \quad (1)$$

with $\gamma_{\min} \gg 1$ and finite γ_{\max} .

(iii) We interpret radio emission as NT electron synchrotron emission, with emissivity

$$\begin{aligned} j_s(\nu) = & N_{e,0} \frac{\sqrt{3}}{4} \frac{e^3 B}{m_e c^2} \left(\frac{\nu}{\nu_0}\right)^{-\frac{q_e-1}{2}} \times \\ & \times \int_0^\pi \sin \theta^{\frac{q_e+3}{2}} \int_{\frac{\nu}{\nu_0 \gamma_{\max}^2 \sin \theta}}^{\frac{\nu}{\nu_0 \gamma_{\min}^2 \sin \theta}} x^{\frac{q_e-1}{2}} \times \\ & \times \int_0^\infty e^{-x} \frac{\cosh(t)}{\cosh(t)} \frac{\cosh\left(\frac{5}{3}t\right)}{\cosh(t)} dt dx d\theta \quad \frac{\text{erg}}{\text{cm}^3 \text{s Hz}}. \quad (2) \end{aligned}$$

(see Chapter 2). The *shape* of the measured radio SED yields the EED spectral index, q_e , and the upper energy cutoff, γ_{\max} . The former is $q_e = 2\alpha + 1$, where α is the (observed) spectral index of the PL portion of the radio SED. The latter is determined by requiring the predicted synchrotron flux distribution to reproduce the observed radio SED turnover. (The radio data do not extend to frequencies low enough to constrain γ_{\min} .) The EED normalization, N_{e0} , and the magnetic field, B , appear as a product in Eq.2 so they can not be determined at this stage.

(iv) We now wish to determine the remaining EED parameters, γ_{\min} and N_{e0} . To this aim we compute the Compton scattering of the energetic electrons described by Eq. 1 off

the CMB photon field. The latter quantity is a Planckian function,

$$n(\epsilon)_{\text{CMB}} = \frac{8\pi}{h^3 c^3} \frac{\epsilon^2}{e^{\epsilon/k_B T} - 1} \text{ cm}^{-3} \text{ erg}^{-1}, \quad (3)$$

with $T = 2.73$ K. The differential number of scattered photons resulting from the Compton scattering of target photons distributed according to Eq. 3 off electrons distributed according to Eq. 1 is

$$\begin{aligned} \frac{d^2 N_{\gamma, \epsilon}}{dt d\epsilon_1} = & \int_{\epsilon_{\min}}^{\epsilon_{\max}} \int_{\max\{\frac{1}{2}\sqrt{\frac{\epsilon_1}{\epsilon}}, \gamma_{\min}\}}^{\gamma_{\max}} N_e(\gamma) \frac{\pi r_0^2 c}{2\gamma^4} \frac{n_{\text{CMB}}(\epsilon)}{\epsilon^2} \times \\ & \times \left(2\epsilon_1 \ln \frac{\epsilon_1}{4\gamma^2 \epsilon} + \epsilon_1 + 4\gamma^2 \epsilon - \frac{\epsilon_1^2}{2\gamma^2 \epsilon} \right) d\gamma d\epsilon \quad (4) \end{aligned}$$

(in $\text{cm}^{-3} \text{ s}^{-1} \text{ GeV}^{-1}$), where ϵ and ϵ_1 are the incident and scattered photon energies, and r_0 is the electron classical radius (see Chapter 2); formally, $\epsilon_{\min} = 0$ and $\epsilon_{\max} = \infty$. Eq. 4 is then multiplied by $\exp(-\tau_x(\epsilon_1))$, where

$$\tau_x(\epsilon_1) = 2 \cdot 10^{-22} \sigma_{\text{HI}} \left(\frac{\epsilon_1}{1 \text{ keV}} \right)^{-8/3}, \quad (5)$$

that accounts for photoelectric absorption suffered by the Compton-upscattered CMB photons by intervening Galactic HI (of column density σ_{HI}) in the direction to the source (e.g., Longair 1981). In Eq. 4 the only unknown quantities still to be determined are γ_{\min} and N_{e0} . The former controls the number density of electrons with (low) energies able to Compton upscatter CMB photons to 1 keV: starting from an arbitrary initial value of γ_{\min} , by decreasing it the predicted 1 keV Compton/CMB emission increases until it achieves stability when all such electrons are included into the process: at this point, γ_{\min} is determined. The photo-electrically absorbed Compton/CMB spectrum, with its shape fixed by now, is calibrated by the measured 1 keV data point: this returns N_{e0} . (An ideal case is when the whole X-ray SED is available: e.g., NGC 6251 in Chapter 3.) The EED is now fully determined.

(iv-bis) If no X-ray emission is available (e.g., Centaurus A in Chapter 3) γ_{\min} cannot be derived directly from data. It can only be estimated assuming it marks the transition from the Coulomb- to the synchrotron/Compton-loss regime, $\gamma_t \simeq 10^2 \left(\frac{n_{\text{gas}}}{10^{-4} \text{ cm}^{-3}} \right)^{1/2} \left(\frac{u_B}{0.025 \text{ eV cm}^{-3}} + \frac{u_r}{0.25 \text{ eV cm}^{-3}} \right)^{-1/2}$ (e.g. Rephaeli & Persic 2015) – where the magnetic and radiation energy densities, u_B and u_r , are scaled to $B = 1 \mu\text{G}$ and the CMB radiation field, respectively. Doing so yields $\gamma_{\min} \sim 100$ in most cases, in fair agreement with values deduced from Compton/CMB modeling the X-ray data. Then calibration of the EED is achieved by normalizing the predicted Compton/(EBL+GFL) spectrum to the lowest-energy *Fermi*/LAT flux density.

(v) The quantity in Eq. 2 that remains to be determined is B . This is obtained by normalizing the computed synchrotron curve to the radio data.

(vi) Calculating the Compton/(EBL+GFL) emission is strictly analogous to the CMB case outlined in (iv) because n_{EBL} and n_{GFL} , that describe the background and foreground radiation field of stellar origin, can be modeled as (diluted) Planckians. This calculation has no free param-

eters: the EED is determined, the EBL is known (see Chapter 3), and the GFL is (for a given galaxy) known (see e.g. Chapter 2). The Compton/(EBL+GFL) emission is purely a prediction (Chapters 2-4). It should be noted that the GFL, spectrally akin to the EBL, is usually subdominant w.r.t. the latter: however, in some cases it is the dominant source of IR/optical target photons in the lobes, and its accurate description is crucial (e.g., Fornax A in Chapter 2). In cases where the radio SED turnover is not clearly suggested by the data, the predicted Compton/(EBL+GFL) yield can be used to estimate γ_{\max} by imposing that it not overproduce the lowest-energy *Fermi*/LAT γ -ray flux.

(vii) A relevant contribution to the γ -ray emission of lobes may come from a hadronic channel. Interactions between energetic and (thermal) gas protons lead to the production of π^0 and π^\pm , whose decays yield γ rays and e^\pm , respectively. Details of this emission and how it is modelled are given in Chapter 2. Here let it suffice to say that, for an ambient thermal gas density n_H and a NT proton energy distribution (PED)

$$N_p(E_p) = N_{p0} (E_p/\text{GeV})^{-q_p} \dots 1 < E_p < E_p^{max} \text{ cm}^{-3}, \quad (6)$$

the pionic emission intensity is $\propto N_{p0} n_H$ (see Chapter 2). Its shape looks like a hump whose shape depends on q_p – flatter for $q_p = 2$ and spikier for $q_p = 2.8$ (see Chapter 3). The production of π^0 -decay γ rays is linked to the production of π^\pm -decay secondary e^\pm . (In the following by "electrons" we shall also mean "positrons".) Secondary electrons retain the parent proton spectral index at formation, so their steady-state EED has slope $q_p + 1$ at high energies, where synchrotron/Compton losses dominate, if no local particle reacceleration is at work. However, as discussed in Chapter 2, particle reacceleration most likely does occur in the lobes, as suggested by the deduced EED spectral indexes of lobes, $q_e \sim 2.2 - 2.5$, being significantly lower than the expected values for electron populations that had aged as result of efficient Compton-synchrotron energy losses.²

1.3.3 Magnetic field

If data necessary for the procedure outlined in Section 1.3.2 to be followed are not available, a frequently made assumption in estimating B is that the particle-field fluid achieves a minimum-energy (\sim equipartition) state (e.g., Longair 1981). For the single-PL EED described above the equipartition magnetic field, B_{eq} , can be written as (e.g., Persic & Rephaeli 2014)

$$B_{\text{eq}} = \left[3.3 \times 10^{-26} (1 + \kappa) 1250^{q_e/2} \psi_5 \times \gamma_{\min}^{2-q_e} \frac{1 - (\gamma_{\max}/\gamma_{\min})^{2-q_e}}{(q_e - 2) a(q_e)} \right]^{\frac{2}{5+q_e}} \text{ gauss} \quad (7)$$

² The synchrotron-Compton energy loss timescale is typically much shorter than the estimated lobe age (e.g., $t_{\text{lobe}} = 5 t_{\text{CS}}$ in the lobes of Fornax A, see Chapter 2). The flatter than expected EED is perhaps due to lack of information on the particle injection (by the jet) and propagation mode and related spectro-spatial aspects, or may be a consequence of efficient re-acceleration that can flatten pre-existing NT particle spectra (e.g., Bell 1978; Wandel et al. 1987) within the lobes.

where $\psi = (f_{5 \text{ GHz}}/\text{Jy}) (r_{\text{lobe}}/100 \text{ kpc})^{-3} (D_L/100 \text{ Mpc})^2$, and $\kappa(q_p, q_e) = u_p/u_e$ is the p/e energy density ratio. Making assumptions on κ , the notion of equipartition has been applied to radio lobes. For example, for a sample of 38 lobes with available 1 keV and 1.4 GHz flux densities and spectral radio indexes, in estimating B_{eq} Croston et al. (2005) assumed equipartition between the electrons and magnetic fields ($\kappa = 0$) and, setting $\gamma_{\min} = 10$, deduced $B \sim 0.7_{-0.4}^{+0.6} B_{\text{eq}}$.

However, two objections may be raised on using equipartition in the context of radio galaxy lobes. Firstly, lobes originate in the highly non-equilibrium phenomenon of AGN jets (see below), so their evolution is very different from that of older galactic systems that have attained a state of hydrostatic or virial equilibrium (e.g. clusters of galaxies): therefore it is doubtful whether the minimum-energy configuration is at all achieved in lobes. Secondly, even if equipartition holds, protons may not be overlooked because the lobes' radio emitting plasma is electrically neutral so protons must be present. The point where a jet flows into the lobe may be considered the lobe's particle injection point: assuming the injected plasma to be electrically neutral and both species (electrons and protons) to have PL spectra, κ can have quite substantial values, especially so if protons have a flatter spectrum than electrons owing to their low energy loss rate (the cross-section for inelastic pp interaction is low, ~ 30 mbarn, in the relevant lobe-frame E_p range) that allows them to essentially retain their injection spectrum. Although energetic protons in the lobes may be radiatively inconspicuous and may not leave any clear spectral signature in the lobe SED, they may dominate the NT energy density. In this case overlooking protons would bias the estimated B_{eq} low by a factor $(1 + \kappa)^{\frac{2}{5+q_e}}$ – which, for typical values $q_p = 2.2$ and $q_e = 2.2 - 2.5$, is ~ 3 .

1.4 Status of knowledge on NT emission in lobes before this thesis

Radio emission from galaxy lobes is described and discussed in Section 1.3. The PL radio SED and smooth, diffuse appearance of lobes in radio maps has been, since early on, the primary indication of a NT population of electrons and a homogeneous magnetic field filling the lobes. As mentioned, FR-II lobes also reveal the sign of (what is interpreted as) the termination shock of the lobe-feeding jet in the form of hotspots at the far ends of the lobes (e.g., Cygnus A).

NT X-ray emission from extended radio galaxy lobes was first detected for Fornax A using spatially unresolved *ROSAT* data (Feigelson et al. 1995). Those authors recognized that Compton upscattering of CMB photons into the X-ray band by relativistic electrons in the diffuse radio lobes is an obligatory process, and noticed that the absence of Faraday depolarization argued (assuming a homogeneous, ordered magnetic field) against the presence of substantial amounts of thermal gas in the lobes: so they concluded that the X-ray emission detected in Fornax A was most likely of Compton/CMB origin; combining radio and X-ray data they suggested a lobe magnetic field intensity of 2-3 μG (Feigelson et al. 1995). Subsequent observations (Kaneda et al. 1995 and Tashiro et al. 2001, *ASCA* data; Isobe et al. 2006, *XMM-Newton* data; Tashiro et al. 2009, *Suzaku* data) con-

firmed the X-ray emission's PL spectrum and spatial extension and coincidence with the radio image, and even resolved the individual E and W lobes. Subdominant thermal X-ray emission was also detected in the lobes of Fornax A, and found to be consistent with thermal bremsstrahlung from a gas with density $n_{\text{gas}} = 3 \cdot 10^{-4} \text{ cm}^{-3}$ and $k_B T \sim 0.5 \text{ keV}$ (Seta et al. 2013). Other X-ray detections of radio lobes (see Chapters 3 and 4), conform to the main feature mentioned above: smooth, spatially extended NT (or thermal + NT) emission that matches the radio morphology.

In γ rays, Centaurus A was the first source detected with Fermi/LAT (Abdo et al. 2010; and later with higher photon statistics by Yang et al. 2012 and Sun et al. 2016). In succession, NGC 6251 (Takeuchi et al. 2012), Centaurus B (Katsuta et al. 2013), and Fornax A (McKinley et al. 2015; Ackermann et al. 2016) followed. Early lobe SED modeling by those groups suggested the γ -ray emission to be Compton-upscattered radiation from the CMB, with additional contribution at higher energies from the EBL in the cases of Cen A and Cen B. As to Fornax A, both McKinley et al. (2015) and Ackermann et al. (2016) concluded that the Compton scattering of energetic electrons off the optical radiation field in the lobes (EBL and GFL) would fall short of matching the observed γ -ray emission, and proposed that a substantial fraction of the latter originates from decays of neutral pions produced in interactions of energetic protons with protons in the lobe plasma. That scenario, however, implied an uncomfortably high proton energy density, $\sim 10^2$ higher than the gas thermal energy density, $u_{th} \sim 0.5 \text{ eV cm}^{-3}$. To ease the problem, McKinley et al. (2015) suggested that pp interactions occur mostly in filaments with very high gas over-density and enhanced magnetic field. However, that suggestion was probably unrealistic because the implied enhancement also in thermal X-ray emission as well as in radio emission (by secondary e^\pm produced in π^\pm decays) are not observed in radio maps and X-ray images of the lobes (e.g., Tashiro et al. 2001, 2009; Isobe et al. 2006). So the issue about a possible pionic signature in the SED of Fornax A was left unsettled.

The properties of NT lobe emission, as they were understood at the time my work started, can be summarized as follows: (i) radio emission is electron synchrotron radiation, and (ii) X/ γ -ray emission results from Compton upscattering of the photon fields present in the lobes (CMB, EBL, GFL – and occasionally synchrotron, e.g. Cygnus A) by the radio-emitting electrons. Such results had been reached through a variety of assumed EED: however, those differing approaches on one hand did check the stability of qualitative results but on the other hand made detailed comparisons between lobes difficult – for example, B -values in the 0.5-20 μG range, corresponding to widely different EED, were reported for Cen A (Sun et al. 2016). One major lingering issue was the claimed presence of protons at a clearly problematic level.

As a consequence, my thesis aims to: (i) build a unified rigorous SED modeling for all lobes, to allow unbiased comparison of lobe properties; (ii) provide an updated account of the superposed photon fields in the lobes, to accurately predict Compton yields; (iii) re-examine the case of the radiative signature of protons in γ rays, once the leptonic contribution in that energy band has been freshly re-assessed.

1.5 Plan of the thesis

This thesis is composed of five chapters. Chapter 2 studies the prototypical lobe system of Fornax A. Chapter 3 studies the lobes of local ($D_L < 125 \text{ Mpc}$) radio galaxies: Centaurus A (six spatially resolved lobe regions), Centaurus B, and NGC 6251. Chapter 4 studies the lobes of distant ($D_L > 125 \text{ Mpc}$) radio galaxies, for which only radio/X-ray SED are available: 3C 98, Pictor A, DA 240, Cygnus A, 3C 326, and 3C 236. Finally, Chapter 5 contains a summary of results and conclusions.

Reference texts consulted during this thesis for basic and useful expressions for emissivities, radiative yields, and secondary particles from pp and $p\gamma$ interactions, include books by Pacholczyk (1970), Tucker (1975), Rybicki & Lightman (1979), Longair (1981), Gaisser (1990), Dermer & Menon (2009) and articles by Blumenthal & Gould (1970), Rephaeli (1979), Mannheim & Schlickeiser (1994), and Kelner, Aharonian & Bugayov (2006). I used the NASA/IPAC Extragalactic Database (NED) which is operated by JPL/Caltech, under contract with NASA.

ACKNOWLEDGEMENTS

I gratefully acknowledge my supervisors Gabriele Giovannini and Yoel Rephaeli for inspiration and guidance. In particular, I thank Yoel for longtime collaboration and friendship. I dedicate this work to my wife Federica and our sons Nicola, Ludovico, Edoardo for supporting me in this effort with their encouragement and patience. I owe special thanks to Federica also for lovingly taking most of my share of family duties upon herself during the preparation of this thesis.

REFERENCES

- Abdo A.A., et al. (*Fermi*/LAT Collab.), 2010, *Science*, 328, 725
 Abdo A.A., et al. (*Fermi*/LAT Collab.; MAGIC Collab.), 2011, *ApJ*, 736:131
 Abramowicz M.A., Fragile P.C., 2013, *Living Rev. in Relativity*, 16, 1
 Ackermann M., Ajello M., Baldini L., et al., 2016, *ApJ*, 826:1
 Aharonian F.A., 2000, *New Astron*, 5, 377
 Akiyama K., et al. (EHT Collab.), 2019a, *ApJ*, 875:L6
 Akiyama K., et al. (EHT Collab.), 2019b, *ApJ*, 875:L1
 Amato E., Blasi P., 2005, *MNRAS*, 364, L76
 Amato E., Blasi P., 2006, *MNRAS*, 371, 1251
 Arbeiter C., Pohl M., Schlickeiser R., 2002, *A&A*, 386, 415
 Atoyan A.M., Dermer C.D., 2003, *ApJ*, 586, 79
 Beall J.H., Bednarek W., 1999, *ApJ*, 510, 188
 Bednarek W., Protheroe R.J., 1999, *MNRAS*, 302, 373
 Begelman M.C., 1998, *ApJ*, 493, 291
 Begelman M.C., Blandford R.D., Rees M.J., 1984, *Rev Mod Phys*, 56, 255
 Bell A.R., 1978, *MNRAS*, 182, 443
 Blandford R.D., 1976, *MNRAS*, 176, 465
 Blandford R., Levinson A., 1995, *ApJ*, 441, 79
 Blandford R., Znajek R.L., 1977, *MNRAS*, 179, 433
 Blandford R., Meier D., Readhead A., 2019, *ARAA*, 57, 467
 Blaziejewski M., Sikora M., Moderski R., Madejski G.M., 2000, *ApJ*, 545, 107
 Blumenthal G.R., Gould R.J., 1970, *RvMP*, 42, 237
 Celotti A., Ghisellini G., 2008, *MNRAS*, 385, 283
 Chen X., Pohl M., Böttcher M., 2015, *MNRAS*, 447, 530

- Croston J.H., Hardcastle M.J., Harris D.E., et al., 2005, *ApJ*, 828, 733
- Czerny B., Hryniewicz, K., 2011, *A&A*, 525, L8
- Dermer C.D., Menon G., 2009, *High Energy Radiation from Black Holes* (Princeton, NJ: Princeton University Press)
- Dermer C.D., Schlickeiser R., Mastichiadis A., 1992, *A&A*, 256, L27
- Dermer C.D., Sturmer S.J., Schlickeiser R., 1997, *ApJS*, 109, 103
- Ekers R.D., Goss W.M., Wellington K.J., et al., 1983, *A&A*, 127, 361
- Fanaroff B.L., Riley J.M., 1974, *MNRAS*, 167, 31P
- Feigelson E.D., Laurent-Muehleisen S.A., Kollgaard R.I., Fomalont E.B., 1995, *ApJ*, 449, L149
- Ferrarese L., Merritt D., 2000, *ApJ*, 539, L9
- Franceschini A., Rodighiero G. 2017, *A&A*, 603, A34 (and Erratum: 2018, *A&A*, 614, C1)
- Fuhrmann L., Larsson S., Chang J., et al., 2014, *MNRAS*, 441, 1899
- Gaisser T.K., 1990, *Cosmic Rays and Particle Physics* (Cambridge University Press, Cambridge)
- Georganopoulos M., Kazanas D., 2003, *ApJ*, 594 L27
- Ghisellini G., Madau P., 1996, *MNRAS*, 280, 67
- Ghisellini G., Tavecchio F., 2009, *MNRAS*, 397, 985
- Ghisellini G., Tavecchio F., Chiaberge M., 2005, *A&A*, 432, 401
- Ghisellini G., Tavecchio F., Foschini L., Ghirlanda G., Maraschi L., 2010, *MNRAS*, 402, 497
- Ghisellini G., Tavecchio F., Maraschi L., Celotti A., Sbarrato T., 2014, *Nature*, 515, 376
- Ginzburg V.L., Syrovatskii S.I., 1964, *The Origin of Cosmic Rays* (New York: Mcmillan)
- Giovannini G., Savolainen T., Orienti M., et al., 2018, *Nature Astronomy*, 2, 472
- Globus N., Levinson A., 2016, *MNRAS*, 461, 2605
- Harris D.E., Krawczynski H., 2002, *ApJ*, 565, 244
- Heckman T.M., Best P.N., 2014, *ARAA*, 52, 589
- Hillas A.M., 1984, *ARAA*, 22, 425
- Isobe N., Makishima K., Tashiro M., et al., 2006, *ApJ*, 645, 256
- Jorstad S.G., Marscher A.P., Mattox J.P., et al., 2001, *ApJ*, 556, 733
- Jorstad S., Marscher A., 2016, *Galaxies*, 4, 47
- Kaneda H., Tashiro M., Ikebe Y., et al., 1995, *ApJ*, 453, L13
- Karouzos M., Britzen S., Witzel A., et al., 2011, *A&A*, 529, A16
- Katsuta J., Tanaka Y.T., Stawarz L., et al., 2013, *A&A*, 550, A66
- Kelner S.R., Aharonian F.A., Bugayov V.V., 2006, *Phys Rev D*, 74(3), 034018
- Kim J.-Y., Krichbaum T.P., Lu R.-S., et al., 2018, *A&A*, 616:A188
- Kino M., Takahara F., Kusunose M., 2002, *ApJ*, 564, 97
- Kormendy J., Ho L.C., 2013, *ARAA*, 51, 511
- Krawczynski H., Böttcher M., Reimer A., 2012, in *Relativistic Jets from Active Galactic Nuclei* (eds. M. Böttcher, D.E. Harris, H. Krawczynski; Berlin: Wiley), p.215
- Lerche I., Schlickeiser R., 1980, *ApJ*, 239, 1089
- Levinson A., Globus N., 2017, *MNRAS*, 465, 1608
- Liu R.-Y., Riegler F.M., Aharonian F.A., 2017, *ApJ*, 842:39
- Longair M.S., 1981, *High Energy Astrophysics* (Cambridge University Press, Cambridge)
- Lovelace R.V.E., 1976, *Nature*, 262, 649
- Mannheim K., 1993, *A&A*, 269, 67
- Mannheim K., 1995, *Astrop Phys*, 3, 295
- Mannheim K., Biermann P.L., 1992, *A&A*, 253, 21
- Mannheim K., Schlickeiser R., 1994, *A&A*, 286, 983
- Maraschi L., Ghisellini G., Celotti A., 1992, *ApJ*, 397, L5
- Maraschi L., Tavecchio F., 2003, *ApJ*, 593, 667
- Marscher A.P., 2014, *ApJ*, 780:87
- Marscher A., Jorstad S.G., Larionov V.M., Aller M.F., Lähteenmäki A., 2011, *JApA*, 32, 233
- Max-Moerbeck W., Hovatta T., Richards J.L., et al., 2014, *MNRAS*, 445, 428
- McKinley B., Yang R., López-Caniego M., et al., 2015, *MNRAS*, 446, 3478
- McKinley J.C., 2006, *MNRAS*, 368, 1561
- Meier D.L., 2012, *Black Hole Astrophysics* (San Francisco: W.H. Freeman & Co.)
- Mertens F., Lobanov A.P., Walker R.C., Hardee P.E., 2016, *A&A*, 595:A54
- Mücke A., Protheroe R.J., 2000, *AIP Conf Proc*, 515, 149
- Mücke A., Protheroe R.J., 2001, *Astrop Phys*, 15, 121
- Mücke A., Protheroe R.J., Engel R., Rachen J.P., Stanev T., 2003, *Astrop Phys* 18, 593
- Nalewajko K., Begelman M.C., Sikora M., 2014, *ApJ*, 789, 161
- Pacholczyk A.G., 1970, *Radio Astrophysics* (San Francisco: W.H. Freeman & Co.)
- Perley R.A., Röser H.-J., Meisenheimer K., 1997, *A&A*, 328, 12
- Penrose R., 1969, *Nuovo Cimento*, 1, 252
- Persic M., Rephaeli Y., 2014, *A&A*, 567, A 101
- Petrosian V., 2012, *SSRv*, 173, 535
- Pohl M., Schlickeiser R., 2000, *A&A*, 354, 395 (and Erratum: 2000, *A&A*, 355, 829)
- Protheroe R.J., 1997, in *Accretion Phenomena and Related Outflows*, IAU Colloquium 163, ASP Conf Ser 121 (eds. D.T. Wickramasinghe, G.V. Bicknell, L. Ferrario), ASP, p.585
- Rani B., Jorstad S.G., Marscher A.P., et al. 2018, *ApJ*, 858:80
- Rephaeli Y., 1979, *ApJ*, 227, 364
- Rephaeli Y., Persic M., 2015, *ApJ*, 805:111
- Rephaeli Y., Sadeh S., 2019, *MNRAS*, 486, 2496
- Richards J.L., Max-Moerbeck W., Pavlidou V., et al., 2011, *ApJS*, 194, 29
- Rybicki S.I., Lightman, 1979, *Radiative Processes in Astrophysics* (New York: Wiley)
- Saikia D.J., Salter C.J., 1988, *ARAA*, 26, 93
- Seta H., Tashiro M.S., Inoue S., 2013, *PASJ*, 65, 106
- Shakura N.I., Sunyaev R.A., 1973, *A&A*, 24, 337
- Sikora M., Begelman M.C., Rees M.J., 1994, *ApJ*, 421, 153
- Sikora M., Madejski G., 2000, *ApJ*, 534, 109
- Sironi L., Spitkovsky A., 2014, *ApJ*, 783:L21
- Sun X.-N., Yang R.-Z., McKinley B., Aharonian F., 2016, *A&A*, 595, A 29
- Syrovatskii S.I., 1959, *SvA*, 3, 22
- Takeuchi Y., Kataoka J., Stawarz L., et al., 2012, *ApJ*, 749:66
- Tashiro M., Makishima K., Iyomoto N., Isobe N., Kaneda H., 2001, *ApJ*, 546, L19
- Tashiro M.S., Isobe N., Seta H., Matsuta K., Yaji Y., 2009, *PASJ*, 61, S327
- Tavecchio F., Ghisellini G., Ghirlanda G., Foschini L., Maraschi L., 2010, *MNRAS*, 401, 1570
- Tavecchio F., Landoni M., Sironi L., Coppi P., 2018, *MNRAS*, 480, 2872
- Tavecchio F., Maraschi L., Ghisellini G., 1998, *ApJ*, 509, 608
- Tucker W.H., 1975, *Radiative Processes in Astrophysics* (Cambridge, MA: MIT Press)
- Yaji Y., Tashiro M.S., Isobe N., et al., 2010, *ApJ*, 714, 37
- Yang R.-Z., Sahakyan N., de Ona Wilhelmi E., Aharonian F., Rieger F., 2012, *A&A*, 542, A 19
- Walker R.C., Hardee P.E., Davis F.B., Ly C., Junior, 2018, *ApJ*, 855:128
- Wandel A., et al., 1987, *ApJ*, 316, 676
- Wang J.-C., 2002, *Ch J Astron Ap*, 2, 1
- Wiegert T., Irwin J., Miskolczy A., et al., 2015, *AJ*, 150:81
- Wilson A.S., Smith D.A., Young A.J., 2006, *ApJ*, 644, L9
- Wykes S., Croston J.H., Hardcastle M.J., et al., 2013, *A&A*, 558, A19

2 CHAPTER 2. NT EMISSION IN THE LOBES OF FORNAX A

Abstract. Current measurements of the emitted SED at radio, X-ray, and γ -ray frequencies provide a sufficiently wide basis for determining basic properties of energetic electrons and protons in the extended lobes of the radio galaxy Fornax A. Of particular interest is establishing observationally, for the first time, the level of contribution of energetic protons to the extended emission observed by the *Fermi* satellite. Two recent studies concluded that the observed γ -ray emission is unlikely to result from Compton scattering of energetic electrons off the optical radiation field in the lobes, and therefore that the emission originates from decays of neutral pions produced in interactions of energetic protons with protons in the lobe plasma, implying an uncomfortably high proton energy density. However, an exact calculation of the emission by energetic electrons in the magnetized lobe plasma leads to the conclusion that all the observed emission can, in fact, be accounted for by energetic electrons scattering off the ambient optical radiation field, whose energy density (which, based on recent observations, is dominated by emission from the central galaxy NGC 1316) is calculated to be higher than previously estimated.

2.1 Introduction

The SED of energetic particles outside their galactic sources are important for determining basic properties of the populations and for assessing the impact of the particle interactions in the magnetized plasma of galactic halos and galaxy clusters. Knowledge of these distributions is generally quite limited and is based largely on just radio observations. Measurements of NT X-ray and more recently also γ -ray emission from the extended lobes of several nearby radio galaxies provide, for the first time, a tangible basis for detailed modeling of the spectral distributions of energetic electrons and protons in the lobes. Sampling the SED over these regions by itself, with only limited spatial information, yields important insight on the emitting electrons and possibly also on energetic protons whose interactions with the ambient plasma may dominate any observed ~ 100 MeV emission (from the decay neutral pions).

The very luminous nearby radio galaxy Fornax A best exemplifies the level of spectral modeling currently feasible with supplementary X/ γ -ray measurements. This system, located at a luminosity distance $D_L = 18.6$ Mpc (Madore et al. 1999) in the outer region of the Fornax cluster, consists of the elliptical galaxy NGC 1316 and two roughly circular (radius $R \simeq 11' \sim 60$ kpc) radio lobes centered (at a distance $s \simeq 17.5'$) nearly symmetrically on its E and W sides, with a galaxy to nearest-lobe-boundary distance of $d \simeq 6.5' \sim 35$ kpc (e.g., Ekers et al. 1983; Isobe et al. 2006; McKinley et al. 2015): the radio image of the lobe system and a cartoon of its geometry are shown, respectively, in Figs. 8 and 10. The galaxy sits at the center of a (sub-cluster) group of galaxies, thought to be falling towards the cluster center (Drinkwater et al. 2001), which includes the star-forming galaxies NGC 1310, NGC 1316C, and NGC 1317 (see Fig. 1 of Iodice et al. 2017).

Detailed modeling of emission from the lobes of Fornax A was carried out by McKinley et al. (2015) and Ackermann et al. (2016); these included fitting radio, *WMAP*, *Planck*, NT emission at 1 keV, and *Fermi* measurements. Whereas the radio and X-ray data points can be fit with a truncated electron spectrum, the indication from both analyses was that Compton scattering of the (radio-emitting) electrons off the EBL and some assumed level of the local optical radiation fields, are too weak to account for the emission observed by *Fermi*. This led to the conclusion that the γ emission could only be interpreted as π^0 -decay from pp interactions; if so, this would imply a very high proton energy density in the lobes.

Specifically, the deduced proton energy density was estimated to be $\sim 10^2$ higher than the gas thermal energy density, $u_{th} \sim 0.5$ eV cm $^{-3}$ (assuming $n_H = 3 \cdot 10^{-4}$ cm $^{-3}$, for $k_B T = 1$ keV; Seta et al. 2013). To ameliorate this clearly problematic result, McKinley et al. (2015) suggested that pp interactions occur mostly in filaments with very high gas over-density and enhanced magnetic field. This could very well be unrealistic given the implied enhancement also in thermal X-ray emission and the enhanced level of radio emission by secondary electrons and positrons produced in charged pion decays. Such enhancements would have likely been detected in both radio maps and X-ray images of the lobes (e.g., Tashiro et al. 2001, 2009; Isobe et al. 2006).

In an attempt to clarify and possibly remove some of the modeling uncertainty we re-assess key aspects of conditions in the Fornax A lobes, and repeat detailed calculations of the emission by energetic electrons and protons. We base our analysis on all the available radio, X-ray, and γ -ray measurements, and on newly-published detailed surface-brightness distribution of stellar emission from the central galaxy NGC 1316. The latter emission is sufficiently intense to constitute the most dominant optical radiation field in the lobes; consequently, the predicted level of γ -ray emission is significantly higher than in previous estimates. In Section 2.2 we briefly review the observations of NT emission in the various bands and the optical radiation field in the lobe region. In Section 2.3 we describe our calculations of the lobe SED model, which is fit to observations in Section 2.4. We conclude with a short discussion in Section 2.5.

2.2 Observations of NT emission from Fornax A

Fornax A lobes have been extensively observed over a wide range of radio and microwave frequencies, in the (soft) X-ray band, and at high energies (≥ 100 MeV) with the *Fermi*/LAT. We use the updated measurements of the lobes in all these spectral regions; the dataset used in our analysis is specified in Table 1 where the listed flux densities are the combined emission from both the E and W lobes. On sufficiently large scales the radio and X-ray emission appears smooth across the lobes, but with E lobe brightness $\sim 1/2$ that of the W lobe.

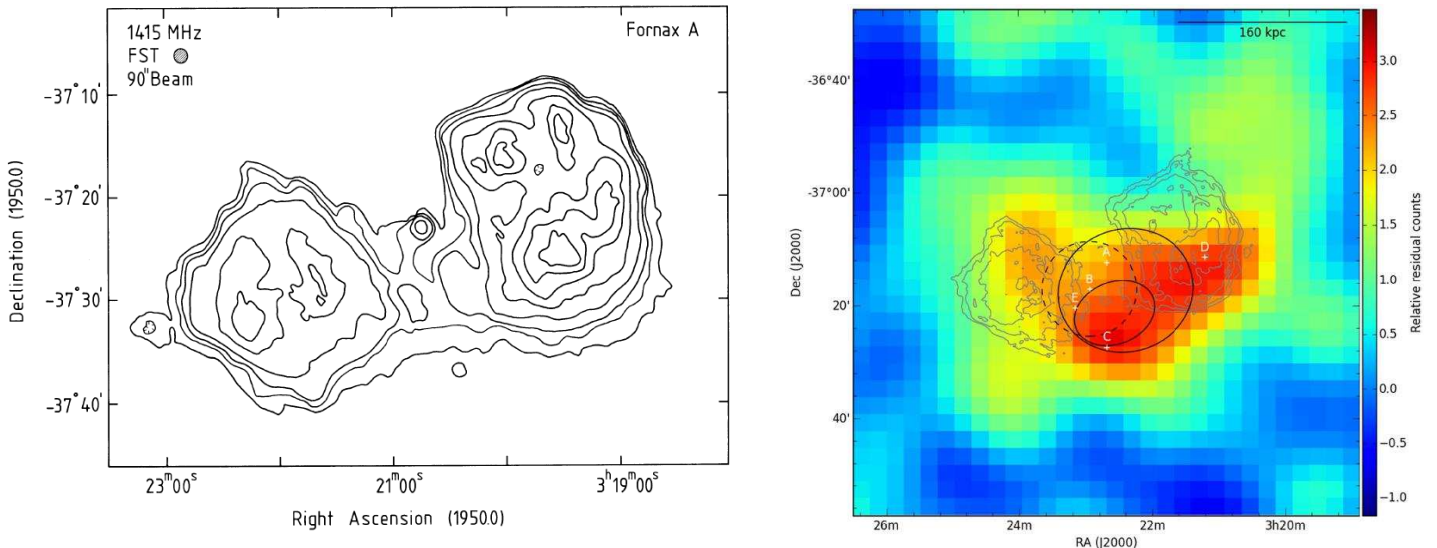


Figure 8. *Left.* The FR-I radio galaxy Fornax A with its lobes: contours indicate the 1.4 GHz brightness distribution. (Reproduced from Fig. 1 of Ekers et al. 1983.) *Right.* Map of the smoothed ($0^\circ.24$ Gaussian FWHM) relative excess of *Fermi*/LAT γ -ray counts w.r.t. a baseline model that contains the Galactic diffuse background and point sources in the $1^\circ.5$ square region around the core of Fornax A in the 1-300 GeV (i.e., (counts – model)/model; reproduced from Fig. 1 of Ackermann et al. 2016). Overlaid are the VLA radio contours (Fomalont et al. 1989) with the core (indicated by A) subtracted. The γ -ray residuals are elongated in a similar way to the radio lobes. If modelled as a point-like source, Fornax A would be localized at position B (the dashed circle shows the 95% confidence error circle). Also shown are the 95% confidence error ellipses for the Fornax A counterparts in the second and third *Fermi*/LAT catalogs. The other points (C,D,E) are the locations of other sources (see details in Ackermann et al. 2016).

We briefly review the most relevant observations used in our analysis, avoiding many of the details that have already been presented in the two recent similar analyses by McKinley et al. (2015) and Ackermann et al. (2016). A reasonably accurate description of the optical and IR fields in the region of the lobes is important for a correct calculation of the predicted high energy X-and- γ emission from Compton scattering of energetic electrons (and positrons), a new aspect of our analysis that leads to a different conclusion on the possible origin of the emission observed by *Fermi*.

McKinley et al. (2015) compiled a comprehensive list of previously published radio measurements, supplemented by *WMAP* and *Planck* data in the 22-143 GHz band, and at 154 MHz (observed with the Murchison Widefield Array). When available, single-lobe flux densities were added up to obtain total lobe emission, implying a relatively low contribution from the central galaxy. The flux drops sharply at $\nu \gtrsim 30$ GHz.

X-ray observations and spectral analyses were reported by several groups. Early on Feigelson et al. (1995), using spatially-unresolved *ROSAT* data, argued in favor of a diffuse NT origin of the X-ray emission. Kaneda et al. (1995), based on a spectral decomposition of *ASCA* 1.7-7 keV data, suggested that $\sim 1/3$ and $\sim 1/2$ of the W and E lobe 1 keV flux is NT, with a spectral index consistent with the radio index. This suggestion was confirmed by Tashiro et al. (2001) who, based on follow-up *ASCA* data, concluded that $\sim 1/2$ of the W lobe flux is NT; Tashiro et al. (2009), analyzing W lobe *Suzaku* data with a multi-component spectral model, claimed the 0.5-20 keV spectrum to be fit by a power-law (PL) with an energy index consistent with the radio index. Similarly, Isobe et al. (2006) found that E lobe *XMM-Newton* 0.3 – 6 keV data are well fit by a PL with an index consistent with the radio index (see Fig. 9). Following McKinley et al. (2015), we assume that the 1 keV flux densities (Tashiro et al. 2009, Isobe et al. 2006) are indeed NT.

Based on 6.1 yr of Pass 8 *Fermi*/LAT data, Ackermann et al. (2016) reported extended >100 MeV lobe emission consistent with the radio lobes' morphology, and point-like emission from the radio core (see Fig. 8-right). A similar level of emission, based on a smaller dataset and a point-source spatial model, had been previously reported by McKinley et al. (2015).

2.2.1 Optical radiation fields in the lobes

The superposed radiation field in the lobe region has cosmic and local components.

a) Cosmic Fields.

(i) The CMB is described as an undiluted Planckian with $T_{CMB} = 2.735$ K and integrated intensity $\nu I_\nu = 960$ nW m $^{-2}$ sr $^{-1}$ and energy density $u_{CMB} = 0.25$ eV cm $^{-3}$ (Cooray 2016);

(ii) The cosmic IR background (CIB), originating from dust-reprocessed starlight integrated over the star formation history of galaxies, is described as a diluted Planckian with $T_{CIB} = 29^\circ$ K (from its 100 μ m peak) and integrated intensity $\nu I_\nu = 30$ nW m $^{-2}$ sr $^{-1}$ and energy density $u_{CIB} = 7.85 \cdot 10^{-3}$ eV cm $^{-3}$ (Cooray 2016);

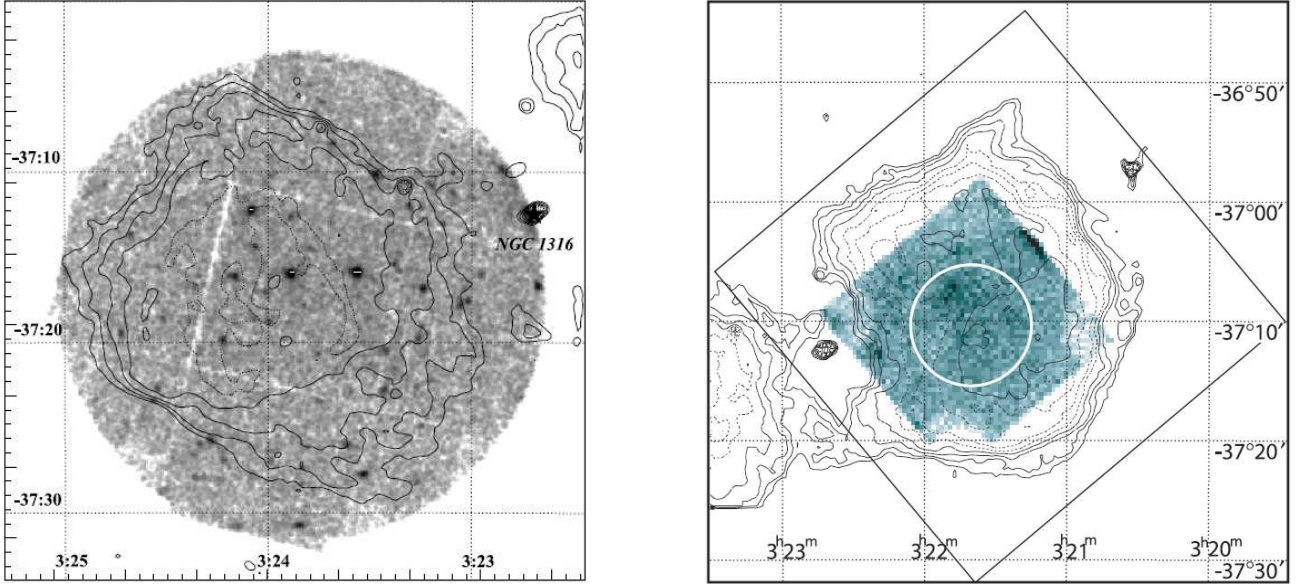


Figure 9. *Left.* Background-inclusive, exposure-uncorrected 0.3-10 keV *XMM-Newton*/MOS image of the E lobe of Fornax A, smoothed with a 2-D Gaussian with $\sigma = 5''$, with the 1.5 GHz VLA contour (Fomalont et al. 1989) overlaid and the position of the host galaxy NGC 1316 indicated (reproduced from Fig. 1 of Isobe et al. 2006). The lobe is fully contained in the MOS field of view. See Isobe et al. (2006) for details. *Right.* The raw image of the W lobe of Fornax A obtained with *Suzaku*/XIS 0, 1, and 3, with the radio image (Fomalont et al. 1989) overlaid (reproduced from Fig. 1 of Tashiro et al. 2009). The FWHM of the HXD/PIN field of view is represented as a solid square. The white circle represents the XIS spectral integration region. See Tashiro et al. (2009) for details.

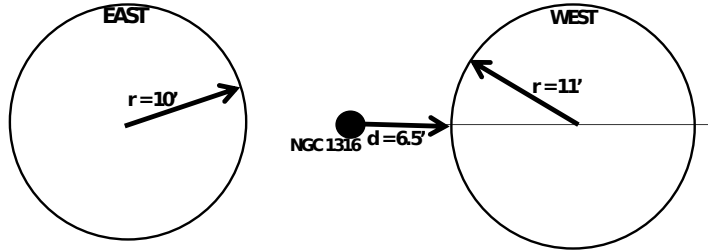


Figure 10. Projected geometry of Fornax A (not to scale).

(iii) The cosmic optical background (COB), originating from direct starlight integrated over all stars ever formed, is described as a diluted Planckian with $T_{\text{COB}} = 2900^\circ\text{K}$ (from its $1\mu\text{m}$ peak) and integrated intensity $\nu I_\nu = 24\text{ nW m}^{-2}\text{ sr}^{-1}$, and $u_{\text{COB}} = 6.28 \cdot 10^{-3}\text{ eV cm}^{-3}$ (Cooray 2016).

The dilution factor, C_{dil} , is the ratio of the actual energy density, u , to the energy density of an undiluted blackbody at the same temperature T , namely $u = C_{\text{dil}}aT^4$, where a is the Stefan-Boltzmann constant. The dilution factors of the cosmic fields are, $C_{\text{CMB}} = 1$, $C_{\text{CIB}} = 10^{-6.724}$, and $C_{\text{COB}} = 10^{-13.726}$.

b) Local Fields.

The local radiation fields are dominated by emission from the central galaxy, NGC 1316, whose SED shows two thermal humps, IR and optical. The IR hump peaks at $100\mu\text{m}$ and has a bolometric luminosity $^3 L_{\text{IR}} \simeq 1.5 \cdot 10^{43}\text{ erg s}^{-1}$; its effective temperature is $T_{\text{gal, IR}} = 29\text{ K}$. The optical hump peaks at $1\mu\text{m}$, corresponding to an effective temperature $T_{\text{gal, OPT}} = 2900\text{ K}$, and has a bolometric luminosity $L_{\text{opt}} \sim 1.4 \cdot 10^{45}\text{ erg s}^{-1}$ from the total r -band magnitude (Iodice et al. 2017), converted to bolometric magnitude, as detailed below.

³ The total-IR flux is computed from the *IRAS* flux densities at 12, 25, 60 and $100\mu\text{m}$ (Golombek et al. 1988) using $f_{\text{IR}} = 1.8 \cdot 10^{-11}(13.48 f_{12} + 5.16 f_{25} + 2.58 f_{60} + f_{100})\text{ erg cm}^{-2}\text{ s}^{-1}$ (Sanders & Mirabel 1996).

Table 1. Emission from the lobes.

Frequency log(ν /Hz)	Energy Flux 10^{-12} erg cm $^{-2}$ s $^{-1}$	Reference	Frequency log(ν /Hz)	Energy Flux 10^{-12} erg cm $^{-2}$ s $^{-1}$	Reference
7.476	0.634 ± 0.063	Finlay & Jones 1973	10.515	3.08 ± 0.185	McKinley et al. 2015
7.933	0.814 ± 0.163	Mills et al. 1960	10.607	2.67 ± 0.240	McKinley et al. 2015
8.188	1.16 ± 0.220	McKinley et al. 2015	10.644	2.70 ± 0.540	McKinley et al. 2015
8.611	1.06 ± 0.106	Robertson 1973; Cameron 1971	10.781	2.84 ± 0.426	McKinley et al. 2015
8.778	1.86 ± 0.465	Piddington & Trent 1956	10.848	2.11 ± 0.359	McKinley et al. 2015
8.926	1.42 ± 0.128	Jones & McAdam 1972	11.000	1.20 ± 0.300	McKinley et al. 2015
9.151	1.77 ± 0.142	Ekers et al. 1983	11.155	0.415 ± 0.212	McKinley et al. 2015
9.179	1.77 ± 0.199	Fomalont et al. 1989	17.38	0.498 ± 0.100	Tashiro et al. 2009; Isobe et al. 2006
9.431	2.65 ± 0.265	Shimmins 1971	22.60	0.7 ± 0.2	Ackermann et al. 2016
9.699	2.74 ± 0.411	Gardner & Whiteoak 1971	23.15	1.0 ± 0.2	Ackermann et al. 2016
10.353	3.18 ± 0.159	McKinley et al. 2015	23.75	1.1 ± 0.2	Ackermann et al. 2016
10.453	3.10 ± 0.217	McKinley et al. 2015	24.31	0.8 ± 0.2	Ackermann et al. 2016

The optical stellar surface-brightness distribution of NGC 1316, with a half-light radius of $135''$, can be decomposed into a (nearly) de Vaucouleurs spheroid plus an exponential envelope (Iodice et al. 2017). Its deprojection, i.e., the emissivity distribution, will be used to model the distribution of the photon energy density.

The de Vaucouleurs profile is given by $\sigma(R) = \sigma_0 \exp[-\delta(R/R_e)^\alpha]$, where σ_0 is the central surface brightness, $\delta = 7.67$, $\alpha = 1/4$, and R_e is the radius encompassing half the (integrated) luminosity. The corresponding deprojected profile can be well approximated by the analytical expression $\rho(x) = \rho_0 x^{-\beta} \exp(-x^\alpha)$ where $x = r \delta^4 / R_e$, $\rho_0 = \sigma_0 \delta^4 / (2R_e) \Gamma(8) / \Gamma((3 - \beta)/\alpha)$, and $\beta = 0.855$ (Mellier & Mathez 1987). From r -band surface photometry measurements (Iodice et al. 2017) $R_e = 87''$ (~ 7.8 kpc) and $\mu_{e,r} = 20.76$ mag arcsec $^{-2}$. The latter can be transformed into b -band magnitudes using $b = r + 1.33(g - r) + 0.20$ (Jester et al. 2005), with $g - r = 0.74$ inside the half-light radius (Iodice et al. 2017): $\mu_{e,g} = 21.94$ mag arcsec $^{-2}$. The b -band bolometric correction, needed to estimate the full-band magnitude, is $BC_b = -0.85 - (b - v)$ mag (Buzzoni et al. 2006); with $b - v = 0.84$ (within $2R_e$; Cantiello et al. 2013), $BC_b = -1.69$. Thus $\mu_{e,bol} = 20.25$ mag arcsec $^{-2}$, which corresponds to 4 $\sigma_{e,bol} = 264.9 L_{bol\odot} \text{ pc}^{-2}$; from $\sigma_0 = e^{7.67} \sigma_e$ we finally derive $\sigma_{0,bol} = 228.3$ erg cm $^{-2}$ s $^{-1}$. The resulting volume brightness distribution of the NGC 1316 stellar spheroid is

$$\rho_{\text{sph}}(r) = 4.7 \cdot 10^{-21} \left(\frac{r}{R_e}\right)^{-0.855} \exp\left[-7.67 \left(\frac{r}{R_e}\right)^{1/4}\right] \text{ erg cm}^{-3} \text{ s}^{-1}. \quad (8)$$

The deprojection of the exponential profile, $I(R) = I_0 \exp[-(R/h)]$, where I_0 is the central surface brightness and h is a characteristic scale, is expressed in terms of a modified Bessel function of the second kind, $\rho(r) = I_0 / (\pi h) K_0(r/h)$ (Baes & Gentile 2011). From Iodice et al. 2017 we get $\mu_{0,r} = 22.79$ mag arcsec $^{-2}$ and $h_r = 317''$ (~ 28.6 kpc); however, the stellar envelope is measured to be considerably bluer at larger radii (see their Figs. 4, 6-left), implying $h_g \sim 360''$ (~ 32.5 kpc). Following the same procedure adopted for the spheroid, $I_{0,bol} = 0.016$ erg cm $^{-2}$ s $^{-1}$. The resulting emissivity distribution of the NGC 1316 stellar envelope is

$$\rho_{\text{env}}(r) = 5.2 \cdot 10^{-26} K_0(r/h) \text{ erg cm}^{-3} \text{ s}^{-1}. \quad (9)$$

We can now calculate the galaxy optical photon energy density, $u_{\text{gal OPT}}$, in the lobes. Given that the current X-ray and γ -ray data are not spatially resolved, we take a volume average as a nominal value. The exact calculation accounting for the full light distribution and averaging over the volume of the lobes requires a 6D integration, but given the approximate nature of our treatment, we compute $u_{\text{gal OPT}}$ as a line average along the nearest-to-farthest-boundary lobe diameter of the stellar spheroid and envelope components

$$u_j = \frac{\rho_0 \lambda_j}{8\pi c \rho_s} \int_0^{2r_s/\lambda_j} \int_0^\infty \int_0^{2\pi} \int_0^\pi f_j \left(\sqrt{[\rho \sin(\theta) \sin(\phi) + d + \xi]^2 + [\rho \cos(\theta)]^2 + [\rho \sin(\theta) \cos(\phi)]^2} \right) \sin(\theta) d\theta d\phi d\rho d\xi \frac{\text{erg}}{\text{cm}^3} \quad (10)$$

where j denotes either component, $\lambda_j = R_e, h$, and $f_j(R/\lambda)$ is given by Eqs. (8) and (9). The resulting u_j values are $7.500 \cdot 10^{-14}$ erg cm $^{-3}$ (disk) and $4.556 \cdot 10^{-14}$ erg cm $^{-3}$ (envelope).

Finally, $C_{\text{gal OPT}} = 10^{-12.65}$. A similar calculation yields $C_{\text{gal IR}} = 10^{-7.00}$. Thus, $n(\epsilon)$ includes the CMB, cosmic and local (NGC 1316) IR/optical radiation fields.

Further contributions to the local optical radiation field should also be assessed. The star-forming galaxies NGC 1310, NGC 1316C, and NGC 1317, members of the subcluster that contains Fornax A, lie close to NGC 1316. As their estimated

⁴ $\mu(\text{mag arcsec}^{-2}) = M_{\text{bol}\odot} + 21.572 - 2.5 \log \sigma(L_{\text{bol}\odot} \text{ pc}^{-2})$, with $M_{\text{bol}\odot} = 4.74$ mag and $L_{\text{bol}\odot} = 3.83 \cdot 10^{33}$ erg s $^{-1}$.

projected separations from NGC 1316 ($\sim 20'$, $30'$, $6'$) are comparable to the Fornax A size, they are likely located within the lobe region. Their cumulative luminosity is relatively modest, $\lesssim 15\%$ of the NGC 1316 luminosity (Iodice et al. 2017).

2.3 NT emission in the lobes

Radio emission in the lobes is by electron synchrotron in a disordered magnetic field whose mean value B is taken to be spatially uniform, and X- γ emission is by Compton scattering of the electrons by the CMB and optical radiations fields. A significant energetic proton component could yield additional radio emission by secondary electrons and positrons produced by π^\pm decays, and γ -ray emission from π^0 decay. The calculations of the emissivities from all these processes are well known and standard, and need not be specified here. We will limit our brief treatment here to features in the calculations that result from the observational need to explicitly assume (at the outset) that the particle spectral distributions are truncated.

Given the lack of any information about temporal evolution of the lobe emission, it is appropriate to represent the spectral electron and proton numbers by time-independent, truncated PL distributions in the Lorentz factor γ and energy E . The spectral (in γ) number of electrons in a lobe is then

$$N_e(\gamma) = N_{e,0} \gamma^{-q_e} \dots \gamma_{min} < \gamma < \gamma_{max}, \quad (11)$$

with $\gamma_{min} \gg 1$ and finite γ_{max} . Similarly, the spectral (in E_p) proton number in a lobe is

$$N_p(E_p) = N_{p,0} E_p^{-q_p} \dots E_p^{min} < E < E_p^{max}, \quad (12)$$

in the interval $[E_p^{min}, E_p^{max}]$.

2.3.1 Radiative yields of electrons and positrons

Synchrotron emissivity by the above (isotropically distributed) population of electrons is (Blumenthal & Gould 1970)

$$j_s(\nu) = \frac{\sqrt{3}e^3 B N_{e,0}}{4\pi m_e c^2} \int_{\Omega} \sin \theta d\Omega \theta \int_{\gamma_{min}}^{\gamma_{max}} \gamma^{-q_e} d\gamma \frac{\nu}{\nu_c} \int_{\nu/\nu_c}^{\infty} K_{5/3}(\xi) d\xi \quad \text{erg cm}^{-3} \text{ s}^{-1} \text{ Hz}^{-1}, \quad (13)$$

where $\nu_c = \nu_0 \gamma^2 \sin \theta$ ($\nu_0 = \frac{3eB}{4\pi m_e c}$ is the cyclotron frequency). The modified Bessel function of the second kind, $K_{5/3}(\xi)$, has the integral representation

$$K_{5/3}(\xi) = \int_0^{\infty} e^{-\xi \cosh(t)} \cosh\left(\frac{5}{3}t\right) dt. \quad (14)$$

With $x = \nu/\nu_c = \nu/[\nu_0 \gamma^2 \sin \theta]$ Eq. (13) transforms into

$$j_s(\nu) = N_{e,0} \frac{\sqrt{3}}{4} \frac{e^3 B}{m_e c^2} \left(\frac{\nu}{\nu_0}\right)^{-\frac{q_e-1}{2}} \int_0^{\pi} \sin \theta^{\frac{q_e+3}{2}} \int_{\frac{\nu}{\nu_0 \gamma_{max}^2 \sin \theta}}^{\frac{\nu}{\nu_0 \gamma_{min}^2 \sin \theta}} x^{\frac{q_e-1}{2}} \int_x^{\infty} \int_0^{\infty} e^{-\xi \cosh(t)} \cosh\left(\frac{5}{3}t\right) dt d\xi dx d\theta \frac{\text{erg}}{\text{cm}^3 \text{ s Hz}}. \quad (15)$$

This 4D integral can be readily reduced to a 3D integral

$$j_s(\nu) = N_{e,0} \frac{\sqrt{3}}{4} \frac{e^3 B}{m_e c^2} \left(\frac{\nu}{\nu_0}\right)^{-\frac{q_e-1}{2}} \int_0^{\pi} \sin \theta^{\frac{q_e+3}{2}} \int_{\frac{\nu}{\nu_0 \gamma_{max}^2 \sin \theta}}^{\frac{\nu}{\nu_0 \gamma_{min}^2 \sin \theta}} x^{\frac{q_e-1}{2}} \int_0^{\infty} e^{-x \cosh(t)} \frac{\cosh\left(\frac{5}{3}t\right)}{\cosh(t)} dt dx d\theta \frac{\text{erg}}{\text{cm}^3 \text{ s Hz}}. \quad (16)$$

The (differential) number of scattered photons in Compton scattering of electrons from the above distribution by a diluted (dilution factor C_{dil}) Planckian (temperature T) radiation field,

$$n(\epsilon) = C_{dil} \frac{8\pi}{h^3 c^3} \frac{\epsilon^2}{e^{\epsilon/k_B T} - 1} \text{ cm}^{-3} \text{ erg}^{-1}, \quad (17)$$

is (Blumenthal & Gould 1970)

$$\frac{d^2 N_{\gamma,\epsilon}}{dt d\epsilon_1} = \int_{\epsilon_{min}}^{\epsilon_{max}} \int_{\max\{\frac{1}{2}\sqrt{\frac{\epsilon_1}{\epsilon}}, \gamma_{min}\}}^{\gamma_{max}} N_e(\gamma) \frac{\pi r_0^2 c}{2\gamma^4} \frac{n(\epsilon)}{\epsilon^2} \left(2\epsilon_1 \ln \frac{\epsilon_1}{4\gamma^2 \epsilon} + \epsilon_1 + 4\gamma^2 \epsilon - \frac{\epsilon_1^2}{2\gamma^2 \epsilon} \right) d\gamma d\epsilon \quad \text{cm}^{-3} \text{ s}^{-1} \text{ GeV}^{-1}, \quad (18)$$

where ϵ and ϵ_1 are the incident and scattered photon energies, and $r_0 = (e^2/m_e c^2)^2$ is the electron classical radius. In Eq. (18) we set $\epsilon_{min} = 0$ and $\epsilon_{max}/h = 10^{12}$, 10^{13} , and 10^{15} Hz for the CMB, IR, and optical components, respectively.

2.3.2 Pion decay yields

Collisions of relativistic and ambient protons may lead, with similar probabilities, to the production of π^0 's (mass $m_{\pi^0} = 0.135$ GeV) and π^\pm 's (mass $m_{\pi^\pm} = 0.140$ GeV): γ -rays are produced in the decay $\pi^0 \rightarrow 2\gamma$, whereas secondary e^\pm originate from π^\pm decays according to the scheme $\pi^\pm \rightarrow \mu^\pm + \nu$ and $\mu^\pm \rightarrow e^\pm + 2\nu$ (e.g., Mannheim & Schlickeiser 1994).

The π^0 -decay γ -ray emissivity is (e.g., Stecker 1971)

$$Q_\gamma(E_\gamma)|_{\pi^0} = 2 \int_{E_{\pi^0}^{\min}}^{E_{\pi^0}^{\max}} \frac{Q_{\pi^0}(E_{\pi^0})}{\sqrt{E_{\pi^0}^2 - m_{\pi^0}^2}} dE_{\pi^0} \text{ cm}^{-3} \text{ s}^{-1} \text{ GeV}^{-1} \quad (19)$$

where the factor 2 accounts for the two photons emitted by the π^0 decay, and

$$E_{\pi^0}^{\min}(E_\gamma) = E_\gamma + \frac{m_{\pi^0}^2}{4E_\gamma} \text{ GeV} \quad (20)$$

is the minimum π^0 energy required to produce a photon of energy E_γ ,

$$E_{\pi^0}^{\max}(E_p^{max}) = m_{\pi^0} \left[\frac{2m_p E_p^{max} - 2m_p^2 + m_{\pi^0}^2}{4m_p m_{\pi^0}} + \sqrt{\left(\frac{E_p^{max} + m_p}{2m_p} - 1 \right) \left(\frac{(2m_p E_p^{max} - 2m_p^2 + m_{\pi^0}^2)^2}{8m_p m_{\pi^0}^2 (E_p^{max} + m_p)} - 1 \right)} \right] \text{ GeV} \quad (21)$$

is the maximum energy of a π^0 produced by a proton of energy E_p^{max} , deduced from the kinematics of the interaction (e.g., Eq. B.29 in Domingo-Santamaría 2006; in most cases of interest $E_{\pi^0}^{\max} \lesssim E_p^{max}$), and

$$Q_{\pi^0}(E_{\pi^0}) = \frac{4}{3} \pi n_H \int_{E_p^{thr}(E_{\pi^0})}^{E_p^{max}} J_p(E_p) \frac{d\sigma(E_{\pi^0}, E_p)}{dE_{\pi^0}} dE_p \text{ cm}^{-3} \text{ s}^{-1} \text{ GeV}^{-1} \quad (22)$$

is the spectral distribution of the neutral pions. Here, n_H is the (thermal) gas proton density, $J_p = \frac{c}{4\pi} N_p$ is the (isotropic) energetic proton flux, $d\sigma(E_{\pi^0}, E_p)/dE_{\pi^0}$ is the differential cross-section for production of neutral pions with energy E_{π^0} from a collision of a proton with energy E_p with a proton (essentially) at rest, and $E_p^{thr} \simeq 1.22$ GeV is the threshold energy for production of a neutral pion with energy E_{π^0} . We use a δ -function approximation (Aharonian & Atoyan 2000) to the differential cross-section by assuming that a fixed average fraction, κ_{π^0} , of the proton kinetic energy, $E_p^{kin} = E_p - m_p$, is transferred to the neutral pion, i.e., $d\sigma(E_{\pi^0}, E_p)/dE_{\pi^0} \sim \delta(E_{\pi^0} - \kappa_{\pi^0} E_p^{kin}) \sigma_{pp}(E_p)$ where σ_{pp} is assumed to be the inclusive total cross-section for inelastic pp collisions, i.e. containing the multiplicity of the pions produced in each hadronic interaction (e.g., Dermer 1986; Achilli et al. 2011; Aaij et al. 2014). Then

$$Q_{\pi^0}(E_{\pi^0}) = \frac{c n_H}{3 \kappa_{\pi^0}} N_p \left\{ m_p + \frac{E_{\pi^0}}{\kappa_{\pi^0}} \right\} \sigma_{pp} \left\{ m_p + \frac{E_{\pi^0}}{\kappa_{\pi^0}} \right\} \quad (23)$$

(in $\text{cm}^{-3} \text{s}^{-1} \text{GeV}^{-1}$) where $\kappa_{\pi^0} \simeq 0.17$ in the GeV-TeV region, and $\sigma_{pp}(E_p)$ can be analytically approximated (see Eq. (79) of Kelner et al. 2006). Noting that in the range $5 \lesssim E_p/\text{GeV} \lesssim 50$ (relevant to our analysis), σ_{pp} is roughly constant, $\sigma_{pp,0} \approx 30$ mbarn, we set $\sigma_{pp} = \sigma_{pp,0}$. The resulting γ -ray photon emissivity (in $\text{cm}^{-3} \text{s}^{-1} \text{GeV}^{-1}$; energies are in GeV) is

$$Q_\gamma(E_\gamma)|_{\pi^0} = \frac{2}{3} \frac{c}{\kappa_{\pi^0}} n_H N_{p,0} \sigma_{pp,0} \int_{E_{\pi^0}^{\min}}^{E_{\pi^0}^{\max}} \frac{(m_p + E_{\pi^0}/\kappa_{\pi^0})^{-q_p}}{\sqrt{E_{\pi^0}^2 - m_{\pi^0}^2}} dE_{\pi^0} \text{ cm}^{-3} \text{ s}^{-1} \text{ GeV}^{-1}. \quad (24)$$

The production rate of electrons and positrons is calculated from the π^\pm decay rate density (e.g., Stecker 1971),

$$Q_{\pi^\pm}(E_{\pi^\pm}) = \frac{2}{3} c n_H \int_{E_{\text{thr}}} N_p(E_p) f_{\pi^\pm, p}(E_p, E_{\pi^\pm}) dE_p \text{ cm}^{-3} \text{ s}^{-1} \text{ GeV}^{-1}, \quad (25)$$

where $f_{\pi^\pm, p}(E_p, E_{\pi^\pm})$ is the π^\pm energy distribution for an incident proton energy E_p . The π^\pm energy distribution can be well approximated by assuming that a constant fraction, k_{π^\pm} , of the proton kinetic energy is transferred to charged pions, so that

$$f_{\pi^\pm, p}(E_p, E_{\pi^\pm}) = \sigma_{pp}(E_p) \delta(E_{\pi^\pm} - k_{\pi^\pm} E_p^{\text{kin}}), \quad (26)$$

where $\sigma_{pp}(E_p)$ is the total inclusive cross-section of inelastic pp collisions (see above). For the range of q_p values of interest here, $k_{\pi^\pm} = 0.25$ (Kelner et al. 2006). Substituting Eq. (26) in Eq. (25) we obtain

$$Q_{\pi^\pm}(E_{\pi^\pm}) = \frac{2}{3} \frac{c}{k_{\pi^\pm}} n_H N_{p,0} \left(m_p + \frac{E_{\pi^\pm}}{k_{\pi^\pm}} \right)^{-q_p} \sigma_{pp} \left\{ m_p + \frac{E_{\pi^\pm}}{k_{\pi^\pm}} \right\} \text{ cm}^{-3} \text{ s}^{-1} \text{ GeV}^{-1}. \quad (27)$$

We finally calculate the source spectrum of secondary electron, $Q_{se}(\gamma_e)$ (see Gould & Burbidge 1965; Ramaty & Lingenfelter 1966). In the the muon (\sim pion) frame, the secondary-electron distribution is

$$P(\tilde{\gamma}_e) = \frac{2\tilde{\gamma}_e^2}{A^3} \left(3 - \frac{2\tilde{\gamma}_e}{A} \right), \quad (28)$$

where $\tilde{\gamma}_e$, that reaches a maximum of $A = 105$ (corresponding to 52 MeV), is the (secondary) electron Lorentz factor in the muon frame. $P(\tilde{\gamma}_e)$ can be approximated by a delta function around $\tilde{\gamma}_e^* = \frac{7}{10} A \sim 70 \approx \frac{1}{4} \frac{m_\pi}{m_e}$, i.e., $\delta\left(\tilde{\gamma}_e - \frac{m_\pi}{4m_e}\right)$. Therefore, being $\gamma_e \simeq \tilde{\gamma}_e^* \gamma_{\pi^\pm}$, at high energies it is $E_e = m_e \gamma_e \simeq m_e \tilde{\gamma}_e^* \gamma_{\pi^\pm} = \frac{1}{4} E_{\pi^\pm}$. At low energies we assume that, in fact, $E_e = \frac{1}{4} (E_{\pi^\pm} - m_{\pi^\pm})$. So the e^\pm source spectrum becomes

$$Q_{se}(\gamma_e) \approx \int Q_{\pi^\pm}(\gamma_{\pi^\pm}) \delta\left(\gamma_e - \frac{m_{\pi^\pm}}{4m_e} \gamma_{\pi^\pm}\right) d\gamma_{\pi^\pm} = \frac{4m_e}{m_{\pi^\pm}} Q_{\pi^\pm} \left\{ \frac{4m_e}{m_{\pi^\pm}} \gamma_e \right\}. \quad (29)$$

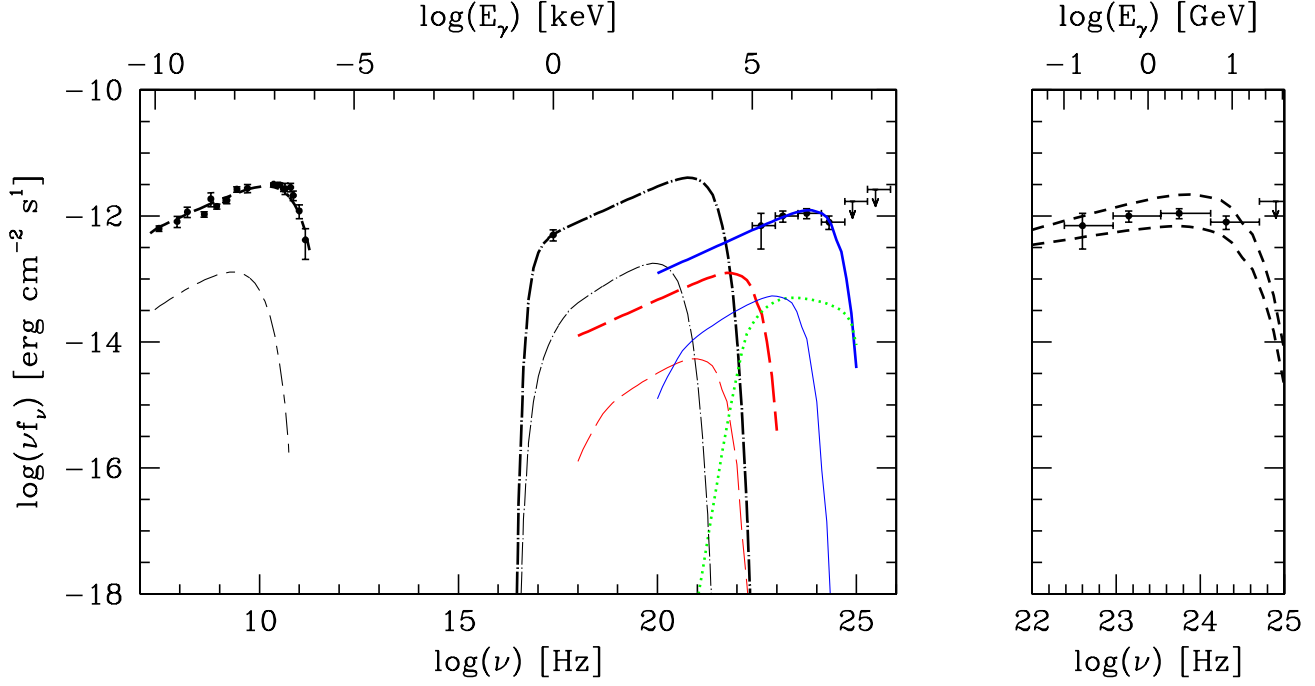


Figure 11. *Left:* broad-band SED of the Fornax A lobes. Data points (Table 1) are shown by dots. Emission components are: synchrotron, black short/long-dashed curves; Compton/CMB, black dotted-long-dashed curves; Compton/IR, red long-dashed curves; Compton/OPT, blue solid curves; pionic, green dotted curve. Thinner curves depict secondary-electron emissions. *Right:* dashed curves bracket the 95% confidence level of the predicted Compton/OPT emission.

Combining Eqs.(29,27), in the laboratory (= galaxy) frame we get

$$Q_{se}(E_e) \approx \frac{8}{3} \frac{c}{k_{\pi\pm}} n_H N_{p0} \sigma_{pp,0} \left(\frac{4E_e + m_{\pi\pm}}{\kappa_{\pi\pm}} + m_p \right)^{-q_p} \text{ cm}^{-3} \text{ s}^{-1} \text{ GeV}^{-1}. \quad (30)$$

At steady state, assuming transport losses to be negligible, the loss equation is

$$\frac{d[b(\gamma)N_{se}(\gamma)]}{d\gamma} = Q_{se}(\gamma), \quad (31)$$

where $N_{se}(\gamma)$ is the steady-state distribution of secondary electrons, and $b(\gamma)$ is the energy loss term. Assuming transport losses to be negligible (e.g., Rephaeli 1979; Persic & Rephaeli 2014), the latter is written as $b(\gamma) = b_0 + b_1(\gamma) + b_2(\gamma)$ (in s^{-1}), where $b_0(\gamma) = 1.2 \cdot 10^{-12} n_e [1 + \ln(\gamma/n_e)/84]$ is the loss rate by electronic excitations in ionized gas, $b_1(\gamma) = 10^{-15} \gamma n_e$ is the loss rate by electron bremsstrahlung in ionized gas, and $b_2(\gamma) = 1.3 \cdot 10^{-9} \gamma^2 (B^2 + 8\pi\rho_r)$ is the loss rate by synchrotron and Compton radiation. In these loss expressions $n_e = n_H$ is the thermal electron density and ρ_r is the radiation energy density. The secondary electron density is then

$$N_{se}(\gamma) = \frac{\int Q_{se}(\gamma') d\gamma'}{b(\gamma)} \text{ cm}^{-3}. \quad (32)$$

where

$$\int Q_{se}(\gamma) d\gamma \approx \frac{2}{3} \frac{c}{q_p - 1} n_H N_{p0} \sigma_{pp,0} m_e^{1-q_p} \left(\frac{4}{\kappa_{\pi\pm}} \gamma + \frac{m_{\pi\pm} + \kappa_{\pi\pm} m_p}{\kappa_{\pi\pm} m_e} \right)^{-q_p+1} \text{ cm}^{-3} \text{ s}^{-1}. \quad (33)$$

The resulting $N_{se}(\gamma)$ can be approximated by

$$N_{se}^{\text{fit}}(\gamma) = N_{se,0} \left[1 + \left(\frac{\gamma}{\gamma_f} \right)^\tau \right]^{-(q_p+1)}. \quad (34)$$

where τ is a (fit) parameter specified below (see section 2.5).

2.4 Modeling the lobe SED

As has already been deduced in previous analyses (McKinley et al. 2015; Ackermann et al. 2016), the energy range of electrons emitting the observed radio and-X-ray radiation is relatively narrow, as is clear from the steep drop of the flux at high radio frequencies, and from the level and spectral shape of the emission around ~ 1 keV. The exact emission level near this energy

is pivotal to our analysis. X-ray observations were reported by several groups, starting with spatially-unresolved *ROSAT* measurements by Feigelson et al. (1995). From spectral analysis of *ASCA* 1.7 – 7 keV data Kaneda et al. (1995) deduced that the emission had a NT component (with a PL index similar to the radio index); specifically, they estimated that $\sim 1/3$ and $\sim 1/2$ of 1 keV flux from the W and E lobes, respectively, was NT; this was later confirmed by Tashiro et al. (2001). Similarly, Isobe et al. (2006) found that E lobe *XMM-Newton* 0.3 – 6 keV data are well fit by a PL with an index consistent with the radio index. Additionally, from analysis of *Suzaku* data Tashiro et al. (2009) estimated that $\sim 1/2$ of the W lobe flux to be NT. Assuming all the measured flux at 1 keV originates in Compton scattering off the CMB yields the overall normalization factor, $N_{e,0} \simeq 8 \cdot 10^{64}$ (corresponding to a density of $N_{e0} = 2 \cdot 10^{-6} \text{ cm}^{-3}$), and the lower energy limit, $\gamma_{min} \simeq 200$.

Fitting the predicted synchrotron flux to measurements in the 0.03-143 GHz yields the spectral index of the electron distribution, $q_e = 2.43$, and the upper energy cutoff, $\gamma_{max} = 7 \cdot 10^4$. The mean magnetic field strength in the lobes is computed using (e.g., Eq. 4.53 in Tucker 1975)

$$B = \left[2.47 \cdot 10^{-19} (5.25 \cdot 10^3)^{(q_e-1)/2} T_{\text{CMB}}^{(q_e+5)/2} \frac{b(q_e)}{a(q_e)} \left[\frac{F_c}{F_s} \left(\frac{\nu_c}{\nu_s} \right)^{(q_e-1)/2} \right]^{-1} \right]^{2/(q_e+1)} \text{ gauss.} \quad (35)$$

Eq. (35) applies when the synchrotron and Compton fluxes are emitted from the same region by electrons with untruncated PL spectrum. Substituting the measured 5 GHz and 1 keV flux densities for F_s and F_c , respectively, Eq. (35) returns $B = 2.64 \mu\text{G}$. The value we find is only slightly different, $B = 2.9 \mu\text{G}$; the $\sim 10\%$ discrepancy mostly stems from the scatter of radio data points about the synchrotron curve.

With the electron distribution fully determined, the Compton yields from scattering off the above specified IR and OPT radiation fields can now be calculated; the results for the full SED are shown in Fig. (11) together with the radio, X-ray, and γ -ray measurements. The main current interest in the predicted Compton yields is the emission in the range 0.1-100 GeV probed by *Fermi*/LAT; the fact that our predicted emission in this range matches well the measurements is an important outcome of our analysis that is essentially a direct consequence of our full accounting for the optical radiation field in the lobes which yielded a higher energy density than estimated by Ackermann et al. (2016). As specified in Section 2.1, in our detailed estimate of the optical radiation field in the lobes we determined that this field is dominated by the stellar emission of the central galaxy, NGC 1316. This conclusion is based on recent mapping of the extended surface brightness distribution of this galaxy by Iodice et al. (2017).

The energetic proton density in the lobes is likely to be quite significant and the energy density higher than that of the electrons; however, this does not necessarily imply that the associated π^0 -decay yield can exceed the above estimated level from Compton scattering of primary electrons off the local optical radiation field. Assuming a proton energy distribution, with $q_p = 2.2$ and a theoretically-motivated nominal proton-to-electron energy-density ratio $\kappa = \rho_p/\rho_e = 50$ (see below), we can calculate the secondary electron and π^0 -decay yields in all the above spectral bands. These emissions are all well below the corresponding levels by primary electrons. Thus, we can only place a $\sim 30\%$ nominal upper limit on the pionic contribution to the flux in the *Fermi*/LAT band, a limit that roughly reflects the modeling uncertainties in our analysis and the level of precision of the current *Fermi*/LAT data.

2.5 Discussion

Detailed modeling of emission in radio lobes is clearly needed in order to determine key properties of energetic particles, magnetic and radiation fields, and for assessing the impact of AGN jets on their intergalactic or intracluster environment. In particular, fitting model predictions to measurements of the lobe SED is critical for a robust determination of the relative significance of energetic protons when gauged by their radiative yields from interactions with ambient gas. By virtue of proximity, brightness of its lobes, and adequate multi-spectral observations, Fornax A is one of the most suitable for such a study.

In our analysis of the broad-band SED of the Fornax A lobes we use the simplest truncated-PL spectral distribution, the most constraining SED dataset currently available, and a recently published, sufficiently precise NGC 1316 light distribution. Assuming the X-ray flux originates from electron Compton scattering off the CMB, our main result is that the related flux from Compton scattering off the optical radiation field, which is dominated by the central galaxy, is consistent with the *Fermi*/LAT measurements. Thus, there is no apparent need for an additional pionic component (at a level comparable to current observations). This conclusion would only be strengthened if account is taken of the estimated $\lesssim 15\%$ contribution to the observed emission by NGC 1316 (Ackermann et al. 2016), and an additional $\lesssim 15\%$ enhancement of the intra-lobe optical light by emission from nearby star-forming galaxies. In light of this, only an upper limit can be set on a (likely) pionic component, in contrast with the conclusion reached by McKinley et al. (2015) and Ackermann et al. (2016).

Limits on the ambient proton spectral parameters can be set by selecting the proton distribution's spectral index and maximum energy to be close to the values that would be implied from fitting a pionic component to the *Fermi*/LAT data; this yields $q_p = 2.2$ and $E_p^{max} = 50 \text{ GeV}$, respectively. The value of the index is in the range of what is theoretically predicted. Assuming a nominal p/e energy density ratio of 50, as appropriate for an electrically neutral NT plasma for the deduced value of q_e and assumed q_p (Persic & Rephaeli 2014), then $N_{p0} = 1.7 \cdot 10^{62}$. This would imply a total NT proton energy of $7.2 \cdot 10^{58} \text{ erg}$, roughly two orders of magnitude lower than what would be required if the measured γ -ray emission were of pionic origin (McKinley et al. 2015; Ackermann et al. 2016).

This low-level normalization implies also a correspondingly low secondary electron (and positron) contribution to the

observed emission; thus, the exact values of the proton and secondary- e^\pm spectral indices are of little practical interest. More relevant is the fact that the deduced spectral index, $q_e \sim 2.4$, is significantly lower than the expected value for a population that had aged as result of efficient Compton-synchrotron energy losses – whose characteristic time, $t_{CS} = \gamma/b_2(\gamma) \sim 0.08$ Gyr (estimated using the relevant photon and magnetic field energy densities and $\gamma = 1.35 \cdot 10^4$, i.e., the likely Lorentz factor of an electron emitting at $\nu_c = 1.4$ GHz in the deduced lobe magnetic field, derived from the expression for ν_c with $\langle \sin \theta \rangle = 2/\pi$), is shorter than the estimated age of the lobes, $t_{lobe} \sim 0.4$ Gyr (Lanz et al. 2010). This is perhaps due to lack of information on the particle injection (by the jet) and propagation mode and related spectro-spatial aspects, or perhaps a consequence of efficient re-acceleration that can flatten pre-existing NT particle spectra (e.g., Bell 1978; Wandel et al. 1987) within the lobes. Given these uncertainties, taking $\tau = 3/4$ in Eq. (34) effectively implies a steady-state secondary e^\pm index of (asymptotically) 2.4, same as that of the primary electron spectrum. The secondary electron maximum energy, $\sim \frac{1}{4} E_p^{max}$ (a pp collision originates 3 neutrinos and 1 electron), corresponds to $\gamma_{max} \sim 2.5 \cdot 10^4$.

To assess the accuracy of our quantitative results we focus on the impact of the main observational and modeling uncertainties. Key parameters are the electron number normalization and endpoints of the energy range which were determined from the radio and X-ray data. Specifically, the values of $N_{e,0}$ and γ_{min} were deduced from the measured 1 keV flux, interpreted to be a consequence of Compton scattering off the CMB. While there is appreciable uncertainty in the level of the NT emission at this energy, which was determined by Tashiro et al. (2009) and Isobe et al. (2006), it largely impacts the modeled level of the radio spectrum, whose fit to the radio data yields the value of the mean magnetic field. Therefore, the resulting uncertainty is essentially reflected in the latter quantity whose exact value (in the range $B \sim 1\text{--}3 \mu\text{G}$ in all previous analyses) is clearly not that important (also because it constitutes a nominal volume-averaged value across the lobes). The substantial uncertainty in the spectral shape of the X-ray data results in some level of parameter degeneracy; e.g., the combination $N_{e,0} = 1.1 \cdot 10^{65}$, $\gamma_{min} = 700$ is consistent with the 1 keV flux density, but this higher γ_{min} causes a steeper rise of the predicted flux than suggested by the data. Also, the value of γ_{max} , constrained by the high-frequency turnover of the radio spectrum, is affected by the observational error in the value of q_e , whose relative level (at 1σ confidence level) is estimated to be $\sim 4\%$.

A source of (mostly) modeling uncertainty results from monochromatic to bolometric flux conversion required in order to compute the dilution factor of the optical radiation field sourced by NGC 1316. This involves converting r to b and (then) to bolometric magnitudes based on the adopted stellar population synthesis model. The CIB and COB intensities are known with a $\sim 30\%$ uncertainty (see Cooray 2016).

Important are also the relatively large error intervals of the *Fermi*/LAT data (below ~ 20 GeV). With the best-fit value of the spectral index determined from the radio data, $\alpha \simeq 0.71 \pm 0.04$ (1σ uncertainty), the propagated uncertainty in the predicted Compton flux in the *Fermi*/LAT range is $\sim 15\%$.

A similar joint analysis of the multi-spectral emission from the giant radio lobes of the nearby radiogalaxy Centaurus A, the first extended extragalactic regions detected by *Fermi*/LAT (Abdo et al. 2010; Yang et al. 2012), is clearly of much interest. The lack of unambiguous evidence for NT X-ray emission from the lobes, perhaps due to their large angular size and complex X-ray morphology (e.g., Schreier et al. 1979; Hardcastle et al. 2009 and references therein), does not allow a definite conclusion on the origin of the measured γ -ray emission. Assuming that the observed low energy ($\gtrsim 60$ MeV) emission originates mostly from Compton scattering off the CMB and EBL, allows calibration of the electron spectrum in a purely leptonic model (Abdo et al. 2010⁵). However, the improved spatial resolution attained in more recent radio measurements (Sun et al. 2016) indicates a possible magnetic enhancement at the edge of the south lobe, and thus leads to a lower electron number normalization that lowers the likelihood of the leptonic origin of the γ -ray emission. As previously suggested for Fornax A, a combined lepto-hadronic model seems to require an unrealistically high proton energy density (Sun et al. 2016).

Unequivocal observational evidence for energetic protons in the lobes of radio galaxies is of great interest also for an improved understanding of the origin of extended radio halos in clusters. In a first detailed assessment of galactic energetic proton and electrons sources in clusters (Rephaeli & Sadeh 2016), it was assumed that electrons diffuse out of radio and star-forming galaxies, and because of the lack of clear evidence for an appreciable proton component in the lobes of radio galaxies, their (secondary electron) contribution to the radio halo emission was conservatively ignored. The extended distribution of star-forming galaxies, whose relative fraction increases with distance from the cluster center, is important in order to account for the large size of radio halos. This approach was applied to conditions in the Coma cluster, where the number of star-forming galaxies was estimated from the total blue luminosity of the cluster, and only the two central powerful radio galaxies were included as electron sources. It was found that for reasonable models of the gas density and magnetic field spatial profiles, the predicted profile of the combined radio emission from primary and secondary electrons is roughly consistent with that deduced from current measurements of the Coma halo. However, the level of radio emission was predicted to be appreciably lower than the measured emission, suggesting that there could be additional particle sources, such as AGN and (typically many) lower luminosity radio galaxies. Clearly, therefore, quantitative evidence for energetic protons in radio lobes would have important implications also on our understanding of the origin of cluster radio halos.

Note. An abridged version of this Chapter is published in Persic & Rephaeli (2019).

⁵ The optical emission from the host galaxy, NGC 5128, was estimated to negligibly contribute to the Compton yield.

REFERENCES

- Aaij R., Adeva B., Adinolfi M., et al., 2015, JHEP, 1502, 129 [arXiv:1412.2500]
- Achilli A., Srivastava Y., Godbole R., et al., 2011, Phys Rev D84, 094009 [arXiv:1102.1949]
- Ackermann M., et al. (*Fermi*/LAT Collab.), 2016, ApJ, 826:1
- Aharonian, F.A., Atoyan A.M., 2000, A&A, 362, 937
- Baes M., Gentile G., 2011, A&A, 525, A 136
- Bell A.R., 1978, MNRAS, 182, 443
- Blumenthal G.R., Gould R.J., 1970, RvMP, 42, 237
- Buzzoni A., Arnaboldi M., Corradi R.L.M., 2006, MNRAS, 368, 877
- Cameron M.J., 1971, MNRAS, 152, 439
- Cantiello M., Grado A., Blakeslee J.P., et al., 2013, A&A, 522, A 106
- Cooray A., 2016, Royal Society Open Science, 3, 150555
- Dermer C.D., 1986, A&A, 157, 223
- Domingo-Santamaría E., 2006, PhD Thesis (Universitat Autònoma de Barcelona)
- Drinkwater M.J., Gregg M.D., Holman B.A., et al., 2001, ApJ, 548, L139
- Ekers R.D., Goss W.M., Wellington K.J., et al., 1983, A&A, 127, 361
- Feigelson E.D., Laurent-Muehleisen S.A., Kollgaard R.I., Fomalont E.B., 1995, ApJL, 449, L149
- Finlay E.A., Jones B.B., 1973, Aust. J. Phys., 26, 389
- Fomalont E.B., Ebnetter K.A., van Breugel W.J.M., Ekers R.D., 1989, ApJ, 346, L17
- Gardner F.F., Whiteoak J.B., 1971, Aust. J. Phys., 24, 899
- Golombek D., Miley G.K., Neugebauer G., 1988, AJ, 95, 26
- Gould R.J., Burbidge G.R. 1965, Annales d'Astrophysique, 28, 171
- Hardcastle M.J., Cheung C.C., Feain I.J., Stawarz L., 2009, MNRAS, 393, 1041
- Iodice E., Spavone M., Capaccioli M., et al., 2017, ApJ, 839:21
- Isobe N., Makishima K., Tashiro M., et al., 2006, ApJ, 645, 256
- Jester S., Schneider D., Richards G.T., et al., 2005, AJ, 130, 873
- Jones P.A., McAdam W.B., 1992, ApJS, 80, 137
- Kaneda H., Tashiro M., Ykebe Y., et al., 1995, ApJL, 453, L13
- Kelner S.R., Aharonian F.A., Bugayov V.V., 2006, Phys. Rev. D, 74(3), 034018
- Lanz L., Jones C., Forman W.R., et al., 2010, ApJ, 721, 1702
- Madore B.F., Freedman W.L., Silbermann N., et al., 1999, ApJ, 515, 29
- Mannheim K., Schlickeiser R., 1994, A&A, 286, 983
- McKinley B., Yang R., López-Carniego M., et al., 2015, MNRAS, 446, 3478
- Mellier Y., Mathez G., 1987, A&A, 175, 1
- Mills B.Y., Slee O.B., Hill E.R., 1960, Aust. J. Phys., 13, 676
- Persic M., Rephaeli Y., 2014, A&A, 567, A 101
- Persic M., Rephaeli Y., 2019, MNRAS, 485, 2001 (and Erratum: 2019, MNRAS, 486, 950)
- Piddington J.H., Trent G.H., 1956, Aust. J. Phys., 9, 74
- Ramaty R., Lingenfelter R., 1966, J. Geophys. Res., 71, 3687
- Rephaeli Y., 1979, ApJ, 227, 364
- Rephaeli Y., Sadeh S., 2016, Phys. Rev. D, 93, 101301
- Robertson J.G., 1973, Aust. J. Phys., 26, 403
- Sanders D.B., Mirabel I.F., 1996, ARAA, 34, 749
- Schreier E.J., Feigelson E., Delvaile J., et al. 1979, ApJ 234, L39
- Seo E.S., Ptuskin V.S., 1994, ApJ, 431, 705
- Seta H., Tashiro M.S., Inoue S., 2013, PASJ, 65, 106
- Shimmins A.J., 1971, Aust. J. Phys. Suppl., 21, 1
- Sun X.-N., Yang R.-Z., McKinley B., Aharonian F., 2016, A&A, 595, A 29
- Stecker F.W., 1971, Cosmic Gamma Rays (Baltimore: Mono Book Corp.)
- Tashiro M.S., Isobe N., Seta H., Matsuta K., Yaji Y., 2009, PASJ, 61, S327
- Tashiro M.S., Makishima K., Iyomoto N., et al., 2001, ApJL, 546, L19
- Tucker W., 1975, Radiative Processes in Astrophysics (Cambridge, MA: MIT Press)
- Yang R.-Z., Sahakyan N., de Ona Wilhelmi E., Aharonian F., Rieger F., 2012, A&A, 542, A 19
- Wandel A., Eichler D., Letaw J.R., et al., 1987, ApJ, 316, 676

3 CHAPTER 3. NT EMISSION IN THE LOBES OF CENTAURUS A, CENTAURUS B, AND NGC 6251

Abstract. Radio and γ -ray measurements of large lobes of several radio galaxies provide adequate basis for determining whether emission in these widely separated spectral regions is largely by energetic electrons. This is very much of interest as there is of yet no unequivocal evidence for a significant energetic proton component to account for γ -ray emission by neutral pion decay. A quantitative assessment of the proton spectral distribution necessitates full accounting of the local and background radiation fields in the lobes; indeed, doing so in our recent analysis of the spectral energy distribution of the Fornax A lobes considerably weakened previous conclusions on the hadronic origin of the emission measured by the *Fermi* satellite. Results are presented here of similar analyses of the measured radio, X-ray and γ -ray emission from the lobes of Centaurus A, Centaurus B, and NGC 6251. Our results indicate that the measured γ -ray emission from these lobes can be accounted for by Compton scattering of the radio-emitting electrons off the superposed radiation fields in the lobes; consequently, we set upper bounds on the energetic proton contents of the lobes.

3.1 Introduction

Measurements of NT emission from the extended lobes of several nearby radio galaxies provide a basis for detailed modeling of the spectral distributions of energetic particles in these environments. Sampling the emission SED, even with only limited spatial information, yields valuable insight on the emitting electrons and possibly also on energetic protons whose pp interactions in the ambient lobe plasma and ensuing π^0 -decay could yield detectable $\gtrsim 0.1$ GeV emission. In addition to the intrinsic interest in physical conditions in radio lobes, modeling energetic particles and their emission processes can yield important insight also for the origin of these particles in galaxy clusters.

Currently available spectral radio, X-ray, and γ -ray measurements of the lobes of the nearby galaxy Fornax A provide an adequate basis for determining the emission processes, the spectral energy distribution of the emitting particles, and the mean value the magnetic field, as has been done by McKinley et al. (2015), Ackermann et al. (2016), and more recently by us (Persic & Rephaeli 2019a; see Chapter 2). Here we carry out similar data analyses of three other radio galaxies whose multi-spectral lobe emission was detected (also) by *Fermi*/LAT: Centaurus A (Cen A), Centaurus B (Cen B), and NGC 6251. Our improved spectral modeling of the measured SEDs of these sources is based on an updated EBL model (Franceschini & Rodighiero 2017, 2018), and on a more complete accounting for the local (ambient) galactic radiation fields than done in previous works.

In light of the fact that the results presented here are based on essentially identical treatment to that described in Chapter 2 (other than the spatially sectionalized modeling of Cen A), our discussion here will be brief and limited only to the most relevant observational data and to the results of our new spectral modeling. In Section 3.2 we summarize the observational data and estimates of the radiation field densities in the lobes of the three galaxies. Results of the

fitted SED models are detailed in Section 3.3. Our main conclusions are in Section 3.4.

3.2 Lobe SED measurements

Measurements of the broad-band emission from the lobes of the three radio galaxies studied in this chapter are reported in Tables 2-4. Here we briefly summarize their main emission properties.

3.2.1 Cen A

At a luminosity distance $D_L = 3.8$ Mpc (Harris et al. 2010), Cen A has two giant elongated radio lobes, each with projected linear size 280 kpc by 140 kpc, centered nearly symmetrically to the north and south of the elliptical galaxy NGC 5128 (Israel 1998). These were the first lobes detected by *Fermi*/LAT (Abdo et al. 2010). The improved spectral (0.06-30 GeV) and spatial resolution attained in more recent radio, *Planck*, and *Fermi*/LAT measurements (Sun et al. 2016, hereafter SYMA16) allow a spatially resolved spectral analysis. On sufficiently large scale the radio and γ -ray emissions appear reasonably uniform across the lobes, but with a somewhat different N and S lobe morphology. X-ray observations and spectral analyses of Cen A were carried out by several groups (Abdalla et al. 2018 and references therein); however, due to the complex morphology of the source (e.g., Schreier et al. 1979; Hardcastle et al. 2009 and references therein), there is no unambiguous detection of NT emission at ~ 1 keV (e.g., Kraft et al. 2003). Detailed lobe SED modeling (Abdo et al. 2010; Yang et al. 2012; SYMA16) suggested that the γ -ray emission from the lobes is Compton-upscattered radiation from the CMB with additional contribution at higher energies from the EBL.

We use the most updated data in the radio and γ -ray bands, as reported by SYMA16: they are specified in Table 2 where the listed flux densities are the emissions from the sub-regions in the north (N) and south (S) lobes identified by SYMA16 (see Fig. 12) as N1, S1 (outer), N2, S2 (middle), and N3, S3 (inner). Radio data comprise 118 MHz Murchison Widefield Array (McKinley et al. 2013), 408 MHz Haslem (Haslam et al. 1982), and 1.4 GHz Parkes fluxes (O'Sullivan et al. 2013), whereas microwave data comprise 40, 44, 70, 100, 143 GHz *Planck* fluxes. These flux densities were measured using aperture photometry over the same sub-regions as specified in the analysis of the extended γ -ray image (SYMA16). As noted by SYMA16, for N2, S2, N3, and S3 the *Planck* data above 70 GHz may be affected by poor understanding of the high frequency background in this band hence may not be reliable. Based on 7 yr of *Fermi*/LAT data and updated *Fermi*/LAT collaboration software tools, SYMA16 extended the detected γ -ray emission down to 60 MeV and up to 30 GeV; using an extended-lobe model for the lobe emission consistent with the radio lobes' morphology and point-like emission from the radio core, they confirmed Yang et al.'s (2012) previous finding that the North lobe's γ -ray emission extends beyond the radio image.

Table 2. Cen A: emission from the lobe regions.

Frequency	N1	N2	N3	S1	S2	S3
Log(ν /Hz)	Radio Flux Density [Jy] [†]					
8.072	362.65 ± 48.26	517.63 ± 61.86	620.58 ± 70.84	479.99 ± 60.31	849.74 ± 95.37	764.29 ± 86.30
8.611	165.07 ± 18.78	265.98 ± 28.95	291.83 ± 31.21	368.12 ± 39.64	495.86 ± 52.01	382.24 ± 40.48
9.146	72.25 ± 1.55	97.56 ± 2.04	107.22 ± 2.22	81.13 ± 1.73	163.92 ± 3.37	162.55 ± 3.34
10.477	9.63 ± 0.01	11.19 ± 0.01	12.41 ± 0.01	9.29 ± 0.01	19.26 ± 0.01	24.36 ± 0.01
10.643	5.43 ± 0.03	8.03 ± 0.03	8.67 ± 0.02	–	10.82 ± 0.03	16.63 ± 0.02
10.845	2.37 ± 0.07	11.70 ± 0.06	7.92 ± 0.05	–	15.67 ± 0.06	12.58 ± 0.05
11.000	–	4.45 ± 0.05	–	–	9.11 ± 0.04	–
11.155	–	–	–	–	3.92 ± 0.04	–
	γ -ray Flux Density [pJy] [‡]					
22.50 ± 0.125	–	4.70 ± 0.50	–	–	–	–
22.75 ± 0.125	3.22 ± 0.46	2.17 ± 0.44	6.34 ± 0.72	–	12.02 ± 1.33	6.31 ± 0.76
23.00 ± 0.125	1.10 ± 0.37	1.33 ± 0.35	2.40 ± 0.44	1.20 ± 0.44	5.25 ± 0.67	2.09 ± 0.45
23.25 ± 0.125	0.60 ± 0.21	0.69 ± 0.22	0.95 ± 0.21	0.52 ± 0.31	2.00 ± 0.30	0.79 ± 0.22
23.50 ± 0.125	0.48 ± 0.12	0.21 ± 0.09	0.34 ± 0.11	0.39 ± 0.12	1.00 ± 0.14	0.29 ± 0.10
23.75 ± 0.125	0.25 ± 0.07	0.14 ± 0.05	0.13 ± 0.06	0.25 ± 0.07	0.39 ± 0.07	0.15 ± 0.06
24.00 ± 0.125	0.07 ± 0.04	0.12 ± 0.04	0.12 ± 0.04	0.13 ± 0.04	0.15 ± 0.04	0.07 ± 0.04
24.25 ± 0.125	0.04 ± 0.01	–	0.06 ± 0.02	0.08 ± 0.01	0.06 ± 0.02	–
24.50 ± 0.125	0.03 ± 0.02	–	0.03 ± 0.02	–	0.04 ± 0.02	–

[†]From Table 3 of SYMA16. [‡]From Fig. 4 of SYMA16.

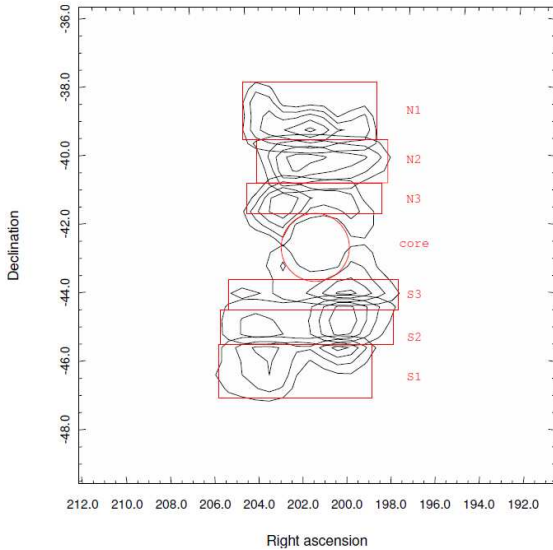


Figure 12. The lobes of Cen A (reproduced from Fig. 3 of SYMA16). The contours correspond to the *Fermi*/LAT γ -ray (> 1 GeV) image. The red rectangles indicate the regions of the radio and Planck aperture photometry, and the contours inside the corresponding regions show the template SYMA16 used for the extraction of the corresponding LAT spectrum. N1, N2, N3 are the outer, middle, inner regions of the northern lobe; and S1, S2, S3 are the outer, middle, inner regions of the southern lobe. The circle denotes the core region.

3.2.2 Cen B

At $D_L = 56$ Mpc, Cen B is the fifth-brightest radio galaxy in the sky. Its projected position close to the Galactic plane results in strong foreground absorption in the optical and

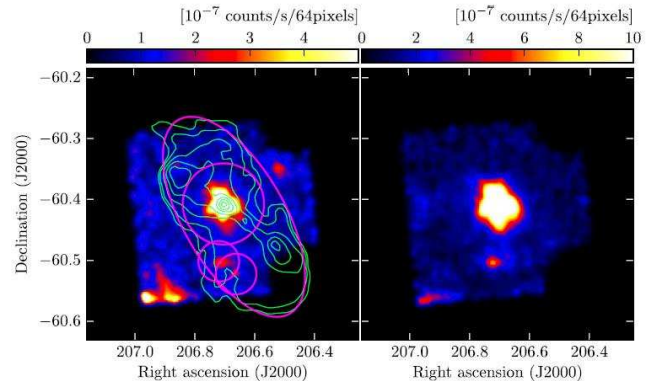


Figure 13. *Suzaku* image (left: 0.5-2 keV; right: 2-10 keV) of Cen B (reproduced from Fig. 8 of K13). The central bright source is the nucleus of the system. The green contours denote the 843 MHz (McAdam 1991). The magenta ellipse denote the source extraction region for the lobes. The three magenta circular regions containing X-ray point-like sources were excluded from the K13 analysis.

X-ray bands (Schröder et al. 2007; Tashiro et al. 1998). *Fermi*/LAT detecting emission from the lobes during ~ 3.5 yr observations (Katsuta et al. 2013, hereafter K13; see Fig. 13). The level of diffuse X-ray emission from the lobes, originally claimed based on *ASCA* data (Tashiro et al. 1998), is marginally consistent with *Suzaku* upper limits (K13). If the flux is close to the *Suzaku* limit (which would be consistent with the *ASCA* estimate), then γ -ray emission could be interpreted as Compton scattering of the radio-emitting off the CMB; otherwise, a jet origin of the measured γ -ray emission would be favored (K13).

The dataset used in our analysis is specified in Table 3,

where the listed fluxes refer to the combined lobes. We take 0.03-5 GHz radio fluxes from Jones et al. (2001; and references therein), 30 GHz *Planck* and 0.2-20 GeV *Fermi*/LAT data from K13, and the 1 keV *ASCA* flux from Tashiro et al. (1998). Concerning X-ray emission, we assume the 2-10 keV *Suzaku* upper limit to be consistent with the *ASCA* flux (see K13), so use the latter 1 keV flux.

3.2.3 NGC 6251

Located at $D_L = 106$ Mpc, NGC 6251 has the largest angular extent among northern radio sources, 1.2° . The NW radio lobe was detected by *Suzaku* to be very extended, likely associated with *Fermi*/LAT source 2FGL J1629.4+8326 (Takeuchi et al. 2012, hereafter T12; see Fig. 14). The observed γ -ray emission was interpreted as Compton scattering of the radio-emitting electrons off the CMB (T12). (Previously, the *Fermi*/LAT counterpart of NGC 6251 was closer to the core and was interpreted as jet emission; Migliori et al. 2011.)

The dataset used in our analysis (Table 4) comes from T12: the 0.327-1.56 GHz Westerbork Synthesis Radio Telescope (WSRT) and Very Large Array fluxes are measured using the same source extraction regions as in the 0.5-8 keV *Suzaku* analysis.

3.3 Radiation fields in the lobes

A reasonably precise determination of the ambient photon fields in the lobes is needed for predicting the level of γ -ray emission from Compton scattering of the radio-emitting electrons (and positrons). Due to the proximity of the central active galaxy, radiation fields in the lobes include local, in addition to cosmic (background) components.

Relevant cosmic radiation fields include the CMB and the EBL. The CMB is a pure Planckian with $T_{\text{CMB}} = 2.735$ K and energy density $u_{\text{CMB}} = 0.25(1+z)^4 \text{ eV cm}^{-3}$ (e.g. Dermer & Menon 2009). The EBL originates from direct and dust-reprocessed starlight integrated over the star formation history of the universe. A recent updated model, based on accurate galaxy counts in several spectral bands, is presented by Franceschini & Rodighiero (2017); its main components are the cosmic IR background (CIB) and the cosmic optical background (COB), described as diluted Planckians (Chapter 2). We represent the EBL as a combination of diluted Planckians,

$$n_{\text{EBL}}(\epsilon) = \sum_{j=1}^7 A_j \frac{8\pi}{h^3 c^3} \frac{\epsilon^2}{e^{\epsilon/k_B T_j} - 1} \text{ cm}^{-3} \text{ erg}^{-1} \quad (36)$$

with $A_1 = 10^{-5.629}$, $T_1 = 29$ K, $A_2 = 10^{-8.496}$, $T_2 = 96.7$ K, $A_3 = 10^{-10.249}$, $T_3 = 223$ K, $A_4 = 10^{-12.027}$, $T_4 = 580$ K, $A_5 = 10^{-13.726}$, $T_5 = 2900$ K, $A_6 = 10^{-15.027}$, $T_6 = 4350$ K, $A_7 = 10^{-16.364}$, $T_7 = 8700$ K, that incorporates galaxy-counts based results (Franceschini et al. 2008; Franceschini & Rodighiero 2017) and γ -ray derived results (that suggest a slight enhancement of the optical hump; Acciari et al. 2019).

Local radiation fields, that constitute the GFL, arise from the central elliptical galaxies located between the lobes. Galaxy SEDs usually show two thermal humps, IR and optical.

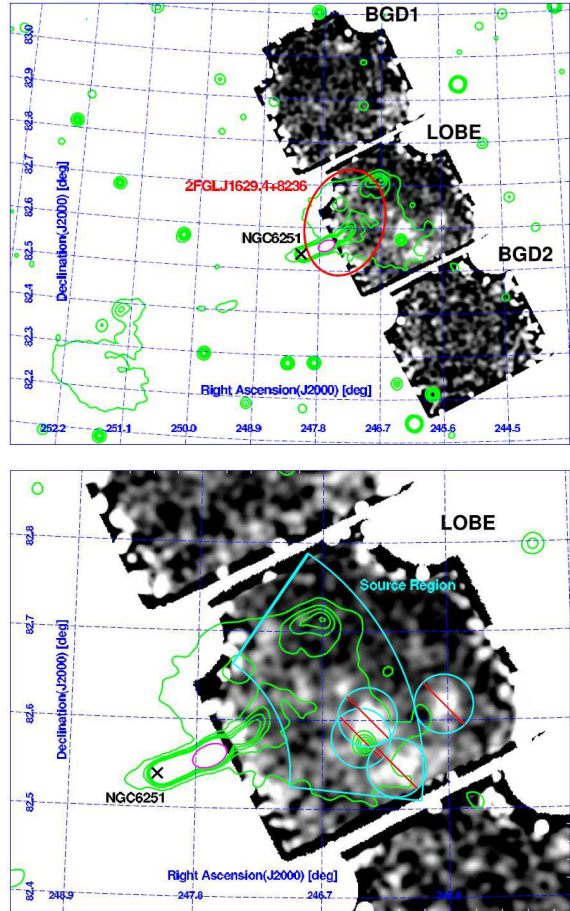


Figure 14. Image of the NW lobe region of NGC 6251 (reproduced with permission from Figures 1 and 2 of T12). The image shows the relative excess of the smoothed *Suzaku* X-ray (0.4-10 keV) photon counts (see T12 for details). *Left.* The radio contours (green in the online version) denote the large-scale structure observed by the Westerbork Synthesis Radio Telescope at $55''$ resolution (Mack et al. 1997) and indicate levels of 8, 31, 54, 77, and 100 mJy/beam. The ellipse (red in the online version) denotes the 95% position error of 2FGL J1629.4+8326. The position of the radio core of NGC 6251 is marked by the cross at the center, and the adjacent outer jet region is marked by the ellipse (magenta in the online version). *Bottom.* Same as top panel, but zooming into the NW lobe region. The *Suzaku* source extraction region is denoted by the section of circular corona (cyan in the online version). The point X-ray sources removed from the T12 analysis are marked by the circles with stripes (cyan and red, respectively, in the online version).

Cen A: The central galaxy, NGC 5128, has a bolometric IR luminosity of $L_{\text{IR}} \simeq 4.8 \cdot 10^{43} \text{ erg s}^{-1}$, as implied by *IRAS* flux densities at 12, 25, 60 and $100 \mu\text{m}$ (Gil de Paz et al. 2007)⁶. The optical bolometric luminosity, $L_{\text{opt}} \sim 1.6 \cdot 10^{44} \text{ erg s}^{-1}$, is derived from the total *B*-band magnitude (Gil de Paz et al. 2007), converted to bolometric magnitude using $B - V \sim 0.9$ (Dufour et al. 1979) following the procedure outlined in Chapter 2. The surface brightness distribution extends out

⁶ The total IR (8–1000 mm) flux is $f_{\text{IR}} = 1.8 \cdot 10^{-11} (13.48 f_{12} + 5.16 f_{25} + 2.58 f_{60} + f_{100}) \text{ erg cm}^{-2} \text{ s}^{-1}$ (Sanders & Mirabel 1996).

Table 3. Cen B: lobe emission.

Frequency log(ν /Hz)	Flux density*	Reference	Frequency log(ν /Hz)	Flux density*	Reference
7.477	1684 \pm 118 Jy	Finlay & Jones (1973)	9.423	60 \pm 6 Jy	Milne & Hill (1969)
7.932	795 Jy	Mills, Slee & Hill (1961)	9.431	61 Jy	Day, Thomas & Goss (1969)
8.004	750 Jy	Mills (1952)	9.699	39 Jy	Goss & Shaver (1970)
8.611	242 Jy	Komessaroff (1966)	10.477	12 \pm 1 Jy	Katsuta et al. 2013
8.611	210 Jy	Kesteven (1968)	17.383	0.22 \pm 0.09 μ Jy	Tashiro et al. 1998
8.611	136 Jy	Shaver & Goss (1970)	22.94 \pm 0.25	6.5 \pm 2.5 pJy	Katsuta et al. 2013
8.926	150 Jy	McAdam (1991)	23.43 \pm 0.25	1.1 \pm 0.5 pJy	Katsuta et al. 2013
9.149	102 \pm 10 Jy	Milne & Hill (1969)	23.94 \pm 0.25	0.24 \pm 0.10 pJy	Katsuta et al. 2013
9.158	130 Jy	Mathewson, Healey & Rome (1962)	24.43 \pm 0.25	< 0.11 pJy	Katsuta et al. 2013

*Where not explicitly indicated, flux density uncertainties are assumed to be 10%.

Table 4. NGC 6251: NW lobe emission.

Frequency* log(ν /Hz)	Flux density	Reference	Frequency* log(ν /Hz)	Flux density	Reference
8.515	3.10 \pm 0.29 Jy	Takeuchi et al. (2012)	17.860	25 \pm 4 nJy	Takeuchi et al. (2012)
8.785	1.75 \pm 0.17 Jy	Takeuchi et al. (2012)	18.161	12 \pm 5 nJy	Takeuchi et al. (2012)
9.193	0.91 \pm 0.09 Jy	Takeuchi et al. (2012)	22.542 \pm 0.25	7.2 \pm 2.6 pJy	Takeuchi et al. (2012)
10.023	0.21 \pm 0.03 Jy	Mack, Klein, O'Dea & Willis (1997)	23.034 \pm 0.25	3.2 \pm 1.9 pJy	Takeuchi et al. (2012)
17.258	44 \pm 12 nJy	Takeuchi et al. (2012)	23.542 \pm 0.25	0.63 \pm 0.19 pJy	Takeuchi et al. (2012)
17.559	46 \pm 10 nJy	Takeuchi et al. (2012)	24.034 \pm 0.25	0.083 \pm 0.024 pJy	Takeuchi et al. (2012)

*The X-ray flux densities refer to the photon energy intervals 0.5-1 keV, 1-2 keV, 2-4 keV, 4-8 keV.

to $\sim 625''$ following a $(R/R_e)^{1/4}$ profile with $R_e = 305''$ ($=11.5$ kpc; Dufour et al. 1979). This effective radius is modest as compared with the distance (70 kpc) to the nearest boundaries of the innermost lobe regions N3 and S3.

Cen B: The host galaxy PKS 1343-601, which is projected close to the Galactic plane, is extremely absorbed ($A_B \sim 12.3$ mag, Schröder et al. 2007). We estimate $L_{\text{opt}} \sim 10^{45}$ erg s $^{-1}$ from $B \sim 11.8$ mag (total, extinction corrected; Schröder et al. 2007) converted to bolometric magnitude assuming $B - V = 0.95$ (a typical value for ellipticals) and following the procedure outlined in Chapter 2. Also, $L_{\text{IR}} \sim 4 \cdot 10^{44}$ erg s $^{-1}$ from the B-luminosity through a FIR-B scaling relation (Bregman et al. 1998) and setting $L_{\text{IR}} \sim 2 L_{\text{FIR}}$ (e.g. Persic & Rephaeli 2007). The surface brightness distribution is unknown; however, if it has a typical $R^{1/4}$ profile, its effective radius can be estimated from the B-luminosity (Romanishin 1986): $R_e \sim 17$ kpc. Lobe radii and nearest lobe boundaries are ~ 100 kpc (Jones et al. 2001, K13).

NGC 6251: We estimate $L_{\text{opt}} \sim 10^{45}$ erg s $^{-1}$ from $B_T^0 = 13.22$ (RC3 catalogue), and following the steps outlined in the previous case, $L_{\text{IR}} \sim 4 \cdot 10^{43}$ erg s $^{-1}$ from *IRAS* flux densities (Golombek et al. 1988). The relevant surface brightness distribution is a modified Hubble profile ($\propto [1 + (r/a)^2]^{-1}$) with $a = 1.1''$ (0.565 kpc; Crane et al. 1993). The lobe radius and nearest boundary distance are 185 kpc and 265 kpc (see T12).

The above IR and optical parameters allow modeling

the GFL. In our calculations we take $T_{\text{gal, OPT}} = 2900$ K and $T_{\text{gal, IR}} = 29$ K (see Chapter 2). The γ -ray data for the lobe regions of Cen A, and the lobes of Cen B and NGC 6251 are spatial averages. Similarly, we compute the corresponding volume-averaged Compton/GFL yield. As the characteristic radii of NGC 5128, PKS 1343-601, NGC 6251 are small compared with the typical scales of the corresponding lobes (radius, distance from central galaxy), we treat central galaxies as point sources ⁷ (in contrast with our procedure for Fornax A in Chapter 2).

⁷ Assuming the lobe is a sphere with radius r_s , centered at $C(d + r_s, 0)$, with d the x -coordinate of the nearest lobe boundary. A vertical line $x = d + u$ (being u the x -axis running variable inside the lobe, $0 \leq u \leq 2r_s$) intersects the lobe at $y_t = \pm \sqrt{-(d+u)^2 + 2(d+r_s)(d+u) - d(d+2r_s)}$. The photon energy density at the lobe boundary is $u_{\text{gal}}(d) = L_{\text{opt}}/(4\pi d^2 c)$. Since the lobe is symmetric w.r.t. the x -axis, the volume-averaged energy density is $\bar{u}_{\text{gal}} = \psi u_{\text{opt}}(d)$, where $\psi = V_{\text{lobe}}^{-1} \int_0^{2r_s} \int_0^{y_t} \frac{d^2}{(d+u)^2 + y^2} 2\pi y dy du$ with $V_{\text{lobe}} = (4/3)\pi r_s^3$. This formula applies also to a cylindrical lobe (radius r_s , height r_h , and base located at a distance d from the central galaxy on the x -axis), but with $y_t = r_s$ and $V_{\text{lobe}} = \pi r_s^2 r_h$.

Table 5. Energy densities (eV cm^{-3}) in the lobes.

Energy density	Cen A-N1	Cen A-N2	Cen A-N3	Cen A-S3	Cen A-S2	Cen A-S1	Cen B	NGC6251	Fornax A
u_e	0.043	0.041	0.028	0.026	0.058	0.061	4.623	0.121	0.404
u_B	0.022	0.036	0.060	0.099	0.039	0.022	0.021	0.004	0.209
u_e/u_B	2.02	1.15	0.48	0.26	1.49	2.79	224.5	30.5	1.93

3.4 Modeling NT emission in the lobes

3.4.1 Synchrotron and Compton yields

Radio emission in the lobes is by electron synchrotron in a disordered magnetic field whose mean value B is taken to be spatially uniform. X- γ emission is modeled to originate in Compton scattering of the electrons off the CMB and optical radiation fields. The standard emissivity calculations are briefly described in Chapter 2.

Assuming no appreciable temporal flux variation, the electron energy distribution (EED) is taken to be time-independent, spatially isotropic and truncated-PL distribution in the electron Lorentz factor, $N_e(\gamma) = N_{e,0} \gamma^{-q_e}$ in the interval $[\gamma_{min}, \gamma_{max}]$, with a finite γ_{max} . The electrons traverse magnetized lobe plasma, with field strength B , and scatter off the ambient radiation fields emitting radio synchrotron and Compton X/ γ -ray radiation (see Eqs. 16 and 18 of Chapter 2). The results of our lobe SED modeling are summarized below and shown in Figs. 15 and 16.

Cen A. Measured NT emission at 1 keV, pivotal to the analysis of Fornax A in Chapter 2, is unavailable; diffuse emission from a lobe region of Cen A measured by *XMM-Newton* was determined to be of thermal origin (Kraft et al. 2003). Thus, to calibrate the EED in each lobe region we either maximized the Compton/CMB contribution to the lowest-frequency *Fermi*/LAT point, or normalized it to the *Fermi*/LAT data, if the spectral shape of the data matched that of the predicted Compton/EBL spectrum. Fitting the predicted synchrotron flux to radio data yielded the EED spectral index, q_e . The upper energy cutoff, γ_{max} , was determined by requiring the predicted synchrotron flux to fit the radio SED turnover (e.g., region N1) or, if the latter is not clearly suggested by the data, by requiring the predicted Compton/EBL flux not to overproduce the lowest-energy *Fermi*/LAT data point. The minimum electron energy, γ_{min} , cannot be derived directly from the present data set owing to the lack of low-energy (1 keV) Compton/CMB data. We can only estimate γ_{min} by assuming it marks the transition from the Coulomb-loss regime to the synchrotron/Compton-loss regime, $\gamma_t \simeq 10^2 \left(\frac{n_{gas}}{10^{-4} \text{ cm}^{-3}} \right)^{1/2} \left(\frac{u_B}{0.025 \text{ eV cm}^{-3}} + \frac{u_r}{0.25 \text{ eV cm}^{-3}} \right)^{-1/2}$ (e.g. Rephaeli & Persic 2015) – where the magnetic and radiation energy densities, u_B and u_r , are scaled to $B = 1 \mu\text{G}$ and the CMB radiation field, respectively. Doing so yielded $\gamma_{min} \sim 100$. The mean magnetic field strength, B , was deduced by adjusting the predicted synchrotron yield to the radio measurements.

The results are shown in Fig. (15) together with the radio and γ -ray measurements. In all lobe regions the predicted Compton emission is consistent with the ~ 0.1 -10 GeV *Fermi*/LAT data. The dominant radiation field is the EBL,

as has been previously suggested, using different EEDs and EBL models (Abdo et al. 2010, SYMA16). The maximum electron energy, γ_{max} , is lower by a factor ~ 2 in the outer as compared to the inner regions (see Fig. (15)). The less energetic EEDs necessarily sample more energetic photons from the target radiation fields to produce Compton emission in the *Fermi*/LAT band. Indeed, a virtually pure EBL shape is revealed by the *Fermi*/LAT data in the outer regions, whereas a significant contribution from the CMB profile is recognizable in the inner regions.

Cen B. We use the photoelectrically absorbed ($N_H = 1.06 \cdot 10^{22} \text{ cm}^2$; K13) 1 keV flux density to determine $N_{e,0}$ assuming the emission is Compton/CMB. Spectral fitting the predicted spectrum to the radio data yields q_e , whereas γ_{max} is deduced by requiring the predicted Compton/CMB flux not to exceed the lowest-energy *Fermi*/LAT data point; we set $\gamma_{min} = 100$. With the electron spectrum fully specified, normalization of the predicted synchrotron spectral flux to the radio measurements yields B . The SED is shown in Fig. (16)-left. *Fermi*/LAT data are modeled as Compton scattering off the CMB at lower energies and as Compton scattering off the EBL (and subdominant GFL) at higher energies. The γ -ray spectrum clearly reflects the shape of the Compton/EBL(+GFL).

NGC6251. The spectral index q_e is deduced as described above. Modeling the γ -ray spectrum and the photoelectrically absorbed ($N_H = 5.54 \cdot 10^{20} \text{ cm}^2$, Dickey & Lockman 1990) X-ray flux as Compton/CMB yields γ_{max} , and $N_{e,0}$ and $\gamma_{min} = 600$. Adjusting the predicted synchrotron yield to the radio data determines B . The SED is shown in Fig. (16)-middle; the X-ray and γ -ray data are interpreted as Compton/CMB emission, with the predicted Compton/EBL flux amounting to just few percent of the *Fermi*/LAT flux (and negligible contribution from Compton/GFL).

As is apparent from Figs. (15),(16), the radiative yields of energetic electrons in the lobes of Cen A, Cen B, and NGC6251 can adequately account for all currently available radio, X-ray, and γ -ray measurements. This basic result of our spectral analyses constitutes further substantiation of what has been suggested in previous works (SYMA16, Yang et al. 2012; K13; T12). Note also that GFL contributes insignificantly to the measured levels of γ -ray emission⁸, in clear contrast with our finding in the case of Fornax A, in whose lobes the main component of γ -ray emission is by Compton scattering off GFL photons (Chapter 2). The double-humped profile in the predicted γ -ray spectra of Cen A and Cen B (Figs. 15 and 16) mimics the spec-

⁸ We use projected galaxy-to-lobe distances (inclinations are unknown), so inferred GFL densities are strict upper limits.

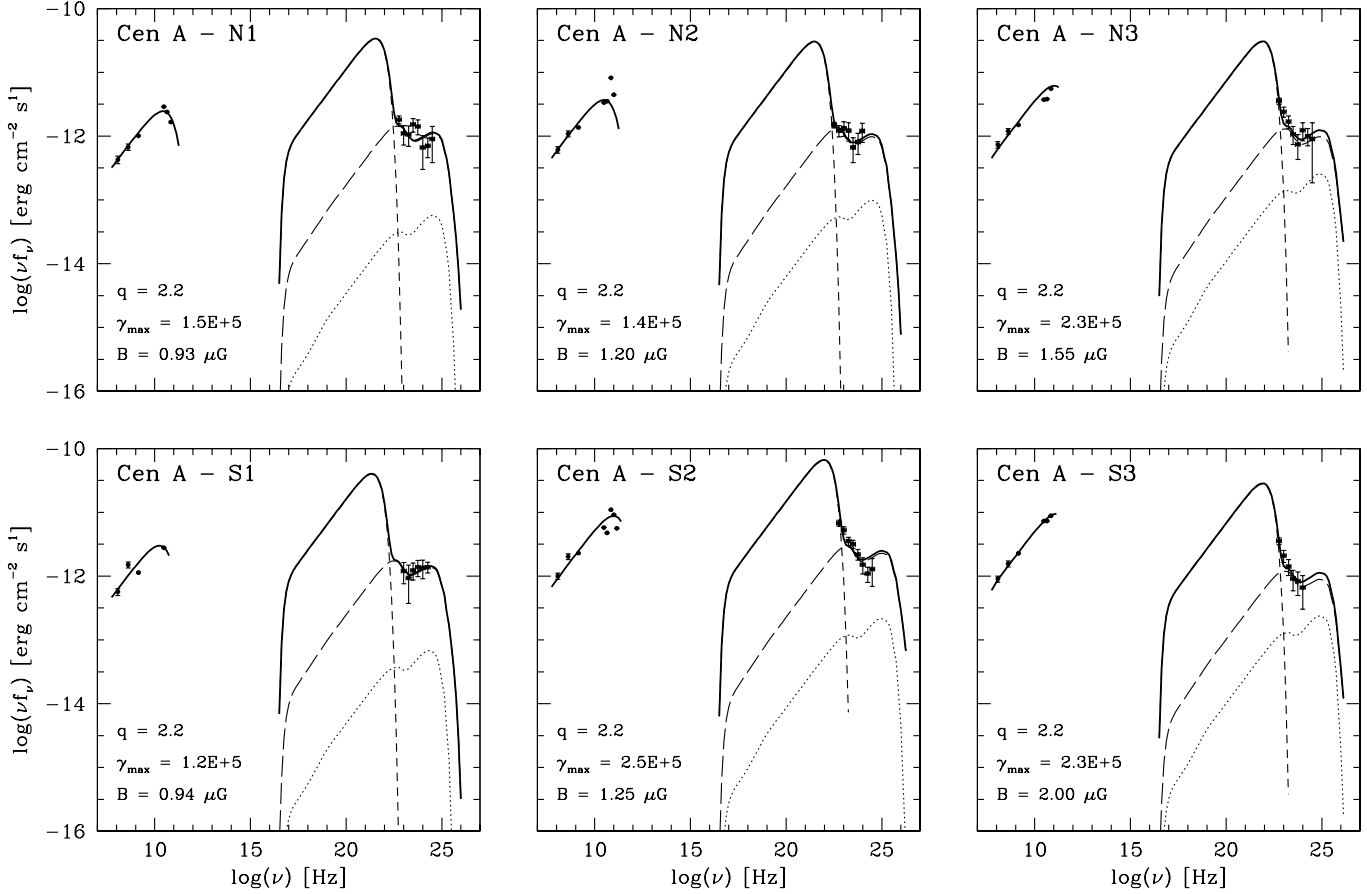


Figure 15. Predicted and measured SEDs for the six lobe regions of Cen A specified in SYMA16. Regions N1, S1 are farthest from the host galaxy NGC 5128; regions N2, S2 are intermediate; regions N3, S3 are closest. Data are denoted by dots (with error bars). Emission component curves are: synchrotron, solid; Compton/CMB, short-dashed; Compton/EBL, long-dashed; Compton/GFL, dotted; total Compton: thick solid. Indicated in each panel are the values of the EED parameters.

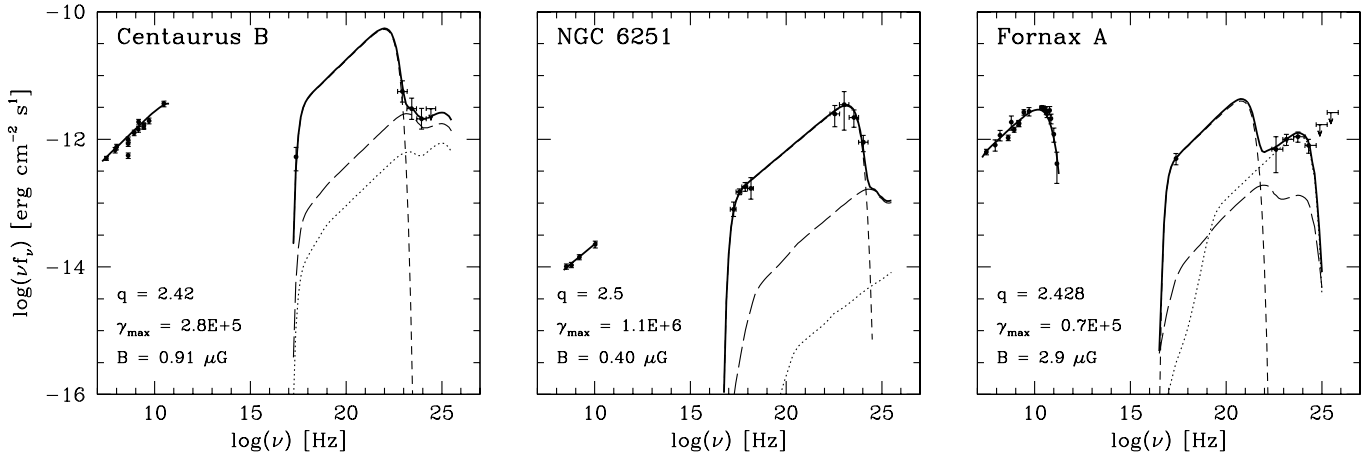


Figure 16. Broad-band SEDs of Cen B and NGC 6251. For comparison, the SED of Fornax A is also shown: the model is as in Chapter 2 except for implementing the current EBL model and neglecting secondary yields. Emissions and model parameters are as in Fig. (15).

tral distribution of the EBL (and GFL); this underlines its origin. Also, the sharp γ -ray cutoff in the spectrum of NGC 6251 reflects the truncation of the electron energy distribution. Thus, these features by themselves indicate that the γ -ray spectral profiles of these sources are unlikely to be of hadronic origin that has the characteristic hump-shaped pion-decay profile. It seems that this *a priori* rules out any significant pionic component to these SEDs. (In contrast, the γ -ray profile of Fornax A is amenable to a pionic interpretation, see McKinley et al. 2015 and Ackermann et al. 2016.)

3.4.2 Upper limits on proton contents in lobes: the case of Cen A

Energetic particles in the lobes are thought to be injected by jets emanating from the central galaxy. There is mounting evidence (e.g. Krawczynski et al. 2012) that AGN jets are energetically and dynamically dominated by protons, albeit with an uncertain proton-to-electron number density ratio. This is deduced from limits on the electron (and positron) contents of jets deduced from the lack of soft-X-ray excesses, and based on insight gained from leptonic models of knots and blazars. Furthermore, X-ray cavities in galaxy clusters (interpreted as expanding bubbles from radio sources) require a significant pressure component, in addition to that of energetic electrons and magnetic fields, in order to overcome thermal intracluster gas pressure (e.g. Wilson et al. 2006). Jet protons can undergo photopion production through $p\gamma$ interactions, and most of the proton energy is eventually channeled into pair production. Due to their less efficient radiative losses, protons can be accelerated to much higher final energies than electrons. Acceleration is likely distributed along the jet because adiabatic and radiative cooling would cause the jet surface brightness to decrease much faster with galactocentric radius than observed (Blandford et al. 2019). If so, the electrically neutral NT plasma injected by the jet into the lobes would have a similar spectral index for protons and electrons, so their energy densities may be related, $u_p/u_e \sim (m_p/m_e)^{(3-q)/2}$ (e.g. Persic & Rephaeli 2014).

The pionic yield in the lobes can be estimated following the formalism introduced in Chapter 2. Assuming the PED to be $N_p(E) = N_{p0}E^{-q_p}$ (with E in GeV) in the interval 1-500 GeV and the thermal plasma to have a nominal density $n_{\text{gas}} = 10^{-4} \text{ cm}^{-3}$ (Stawarz et al. 2013 for Cen A), an upper limit (UL) to the proton content can be deduced from spectral considerations.

The SEDs of the S1 and S3 regions of Cen A are sufficiently detailed so that the dominance of the Compton components provides a meaningful basis for spectral analysis to set bounds on the proton contents. We consider the two extreme cases, $q_p = 2.0$ (flat hump) and $q_p = 2.8$ (spiky hump) for each region (as shown in Fig. (17)). The *Fermi*/LAT data for S1 are interpreted as largely due to Compton scattering off the EBL, as is clearly reflected in the double-humped EBL profile. In a lepto-hadronic framework a substantial pionic hump tends to smooth out the Compton/EBL double hump feature if $q_p = 2.0$, and to enhance it unacceptably at low *Fermi*/LAT energies if $q_p = 2.8$: in both cases, $u_p \lesssim 20 \text{ eV cm}^{-3}$. In a lepto-hadronic model for S3 a pion component contributes at the highest-energy ($q_p = 2.0$) and lowest-energy ($q_p = 2.8$) *Fermi*/LAT data points: we infer,

respectively, $u_p \lesssim 10 \text{ eV cm}^{-3}$ and $u_p \lesssim 20 \text{ eV cm}^{-3}$. In all cases lepto-hadronic models are inconsistent with the measurements for relatively high PED normalizations.

By comparison, the *Fermi*/LAT spectrum of Fornax A has a humpy shape similar to pionic emission from a PED with $q_p = 2.1$ and $E_{\text{max}} = 50 \text{ GeV}$. The spectrum peaks at the third point, which has the smallest error bars; the above specified pionic emission peaks at similar energies. This coincidence leads to $u_p \lesssim 12 \text{ eV cm}^{-3}$, or possibly $u_p \lesssim 40 \text{ eV cm}^{-3}$ (see Section 3.5). Steeper PED slopes make the pionic hump spikier and shift the pionic peak to lower energies; the larger uncertainty on the first *Fermi*/LAT point implies a weaker limit, $u_p \lesssim 41 \text{ eV cm}^{-3}$ for $q_p = 2.8$ (see Fig. 18).

For a given SED, limits are lower if n_{gas} is higher than the assumed nominal value. The number density of the thermal X-ray emitting gas in southern lobe of Cen A is $n_{\text{gas}} = (0.9 - 2.5) \cdot 10^{-4} \text{ cm}^{-3}$ (Stawarz et al. 2013); for $n_{\text{gas}} = 2.5 \cdot 10^{-4} \text{ cm}^{-3}$ the u_p values would be a factor 2.5 lower than deduced above, e.g. $u_p < 4 \text{ eV cm}^{-3}$ in S3 ($q_p = 2$).

3.4.3 On a jet origin of NT electrons in lobes: the case of Cen A.

Observations show that in all sources energy is dissipated along the jet, from the BH site to the lobes (see review by Blandford et al. 2019). Many FR-I jets dissipate a large fraction of their initial energy at a probable recollimation shock near R_{inf} that causes them to slow down to moderately-relativistic speeds: surprisingly, however, they still carry energy to sites that are order of magnitude further in distance, mostly in the form of magnetic and radiation fields and energetic particles as evidenced by the high luminosities and particle (electron) contents of the lobes. FR-II jets seem to behave in the opposite way: by the time they reach the lobes, they seem to have lost much of their electromagnetic energy while retaining their kinetic energy, i.e. their bulk motion is still highly relativistic. Thus, both FR-I and FR-II jets dissipate much of their energy in the lobes – although this is mostly stored in particle and fields in the former and in bulk motion in the latter.

As a working (albeit speculative) example, let's see how the relativistic electrons that give rise to the diffuse synchrotron and Comptonized emissions in the Cen A lobes are likely injected into the lobes by a jet that shoots from the nucleus of the central elliptical galaxy NGC 5128.

The broad-band SED from the Cen A core, probably associated with such a jet, can be described with a synchrotron-self-compton (SSC) jet model (Abdalla et al. 2018). This involves two double-PL EEDs, at lower and higher energies respectively (see their Table 2). The jet itself is inclined by $\theta = 30^\circ$ to the line of sight so the relativistic boosting affecting the observed flux, described by the Doppler factor $\delta_D \equiv 1/[\Gamma(1 - \beta \cos \theta)]$ where Γ is the bulk Lorentz factor of the jet flow (moving with velocity β), is quite modest: in Abdalla et al.'s model both SSC components have $\delta_D = 1$ which, for $\beta \sim 1$, implies $\Gamma \sim 7.5$.

We may venture into a semiquantitative scenario linking the EEDs of the jet and the lobes. The jet model of Abdalla et al. (2018; see their Table 2) implies two co-axial electron fluids, the outer with density $n_1 = 2650 \text{ cm}^{-3}$ and the inner with density of $n_2 = 680 \text{ cm}^{-3}$. Both fluids move along the

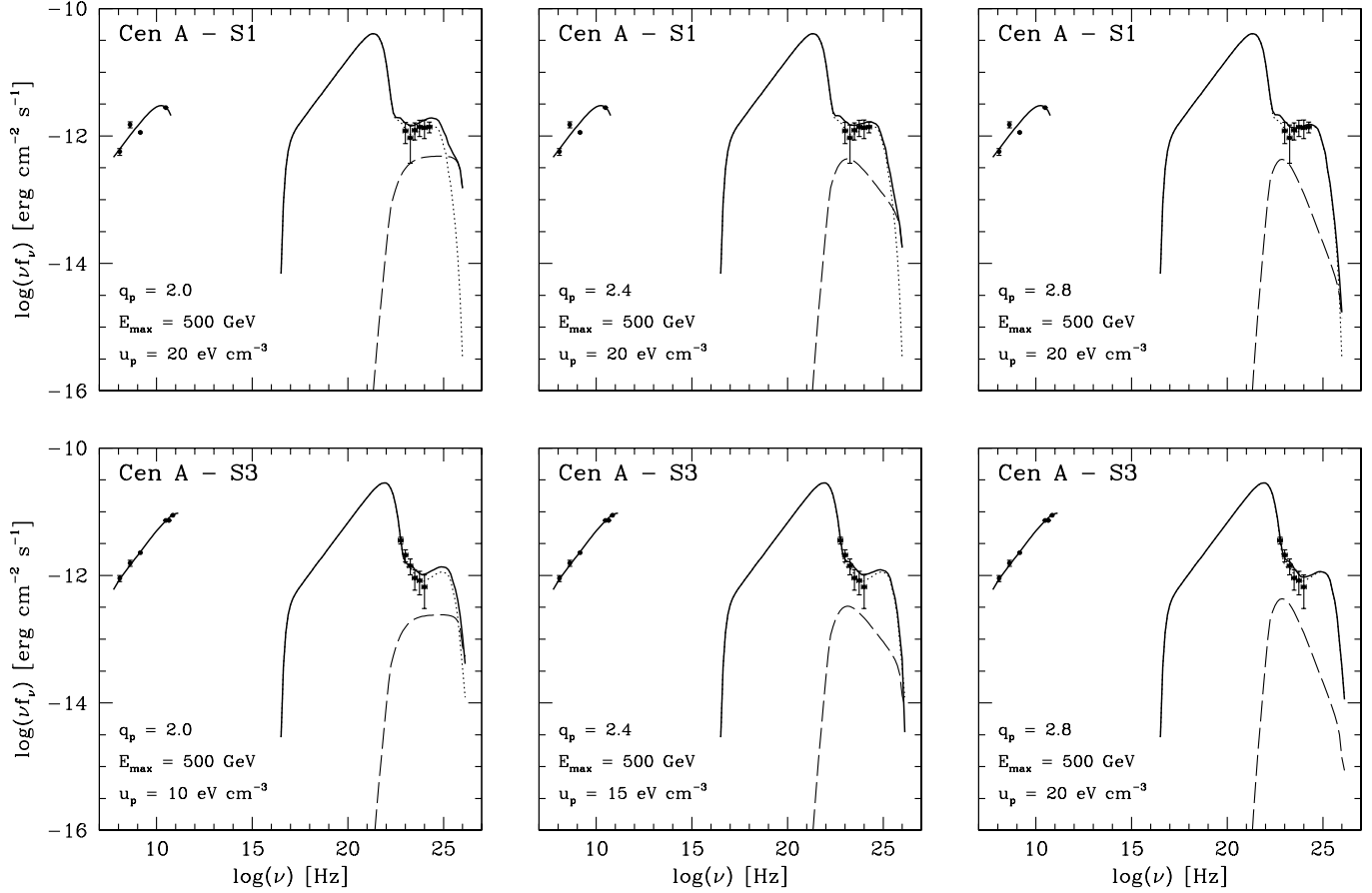


Figure 17. SEDs of two Cen A lobe regions S1, S3 with a lepto-hadronic model overlaid on data. Emission components in the X-ray/ γ -ray energy range are: superposed Compton, dotted line; pionic, dashed line; total: thick solid line. The leptonic components are as in Fig. (15). PED parameters are reported in each panel.

jet with a bulk velocity $v \sim c$ corresponding to $\Gamma = 7.5$. The jet cross section is $\sigma_j = \pi R_1^2$ where $R_1 = 3.3 \cdot 10^{15}$ correspond to component 1. If the jet has been injecting electrons into the lobe (volume $V_{\text{vol}} = \pi 210 \cdot 70^2 \text{ kpc}^{-3}$)⁹ for a time $\Delta t \sim 10^8 \text{ yr}$ and the electrons are trapped within the lobe, the final NT electron density is $N_e = (n_1 + n_2) \pi R_1^2 v \Delta t V_{\text{lobe}}^{-1} \sim 10^{-11} \text{ cm}^{-3}$, a value similar to that deduced for our model EEDs in the lobe regions. This match supports a scenario where the NT electrons in the lobes may result from jet injection.

Upon entering the lobes, an electron with energy γ' in the flow frame has energy $\sim \Gamma \gamma'$ in the lobe frame. (a) The electrons described by the lower-energy component 1 of the jet model (see Abdalla et al.'s (2018) Table 2), provide the majority of the jet-injected electrons but do not contribute to the radiative yield sampled by our SED dataset. Their (effective) limiting energy in the lobe frame, $\gamma_{\text{max}} \sim \Gamma \gamma'_{\text{br}} = 6 \cdot 10^3$, would Compton-upscattered op-

tical photons (of frequency $\nu_{\text{opt}} = (1 \text{ eV}/h)$ to frequencies $\sim \gamma_{\text{max}}^2 \nu_{\text{opt}} \sim 10^{22} \text{ Hz}$, an order of magnitude lower than the lowest-frequency Fermi/LAT flux densities in our dataset. Similarly the radio band, the typical synchrotron frequency corresponding to γ_{max} is $\nu_s = 1.3 \gamma_{\text{max}}^2 B \sim 95 \text{ MHz}$, lower than the lowest frequency for which we have radio flux densities. So the injected electrons from Component 1 are effectively unveiled by our SED dataset. (b) The electrons able to Comptonize EBL and GFL photons into the Fermi/LAT frequency band are those from component 2: in the relevant energy range, this is a PL with index $p = 1.5$ out to $\gamma'_{\text{br}} = 3.2 \cdot 10^4$. In the lobe frame, near injection the stationary EED, if assumed to be a truncated single PL, may be expected to be $\propto \gamma^{-q}$ with $q = p + \eta \sim 2.1$ ($\eta \sim 0.6$ represents the spectral steepening due to diffusion losses – as deduced from cosmic rays in the Milky Way) out to $\gamma_{\text{max}} \sim \Gamma \gamma'_{\text{br}} = 2.4 \cdot 10^5$. Although maybe just coincidental, we note that in the innermost regions (N3, S3) we do find that a single-PL EED with $q = 2.2$ and $\gamma_{\text{max}} = 2.4 \cdot 10^5$ matches the data.

⁹ Similarly to Abdo et al. (2010) we assume a cylindrical size of the Cen A lobe(s) of $L = 210 \text{ kpc}$ (length) and $r = 70 \text{ kpc}$ (radius). The core region identified by SYMA16 has a radius of $\sim 70 \text{ kpc}$; the lobes lay outside of it. The six sub-regions specified by SYMA16 and used here are idealized as cylinders of radius $r = 70 \text{ kpc}$ and height $h = 70 \text{ kpc}$.

In the outermost regions N1 and S1, located at about twice the distance of N3, S3 from the central galaxy, the EED spectral index q is unchanged but the high cutoff energy γ_{max} drops to half its value in the inner regions: this

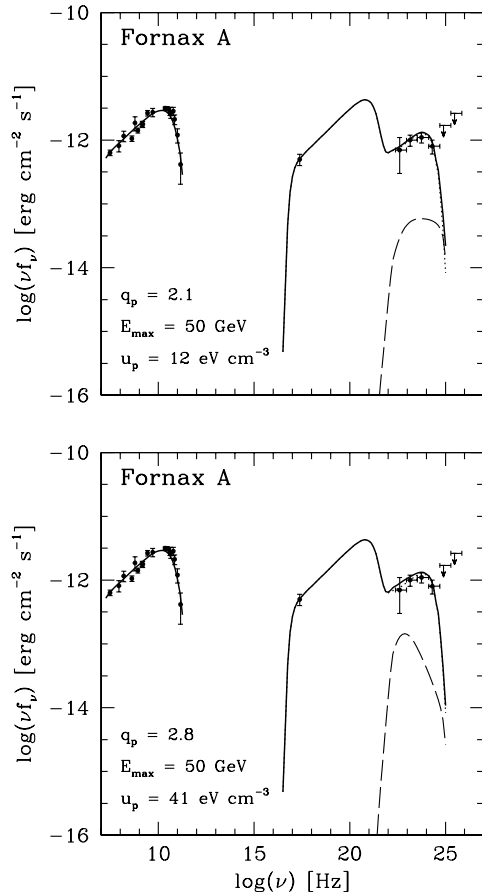


Figure 18. SEDs of Fornax A with a lepto-hadronic model overlaid on data. The leptonic component is as in Fig. 2. PED parameters are indicated. Symbols are as in Fig. (17). For the $q_p = 2.1$ case see also Section 3.4.2.

picture may hint at (longitudinal over distance L) expansion losses ($\propto v/L$) suffered by the NT plasma while it flows along the lobes.

Comparison of the jet and halo magnetic fields may provide a further insight on the jet/halo relationship. The jet model has similar magnetic and electron energy densities, $u_B \sim u_e$. If this similarity is (roughly) conserved from injection to lobe-diffuse configuration, then $B \propto \sqrt{n_e \gamma_{br}}$: that is, assuming (for simplicity) $B' \sim 10$ G and $N_e' \sim 10^3$ cm $^{-3}$ in the jet, the lobe (where $N_e \sim 10^{-11}$ cm $^{-3}$) will have $B \sim 1$ μ G. The latter value is consistent with our fitting results.

3.5 Discussion

The electron energy density arises from $\gamma > \gamma_{min}$ SED-emitting electrons (index: q_e) and from $\gamma < \gamma_{min}$ electrons affected by non-radiative Coulomb losses (index: $q_e - 1$; e.g. Rephaeli & Persic 2015). Table 1 reports the electron and magnetic energy density values for the current lobes and for Fornax A (Chapter 2). The electron and magnetic contributions are comparable in Fornax A and Cen A; in the latter system u_e/u_B increases with increasing galactocentric radius. On the other hand, the magnetic contributions are rel-

atively small in Cen B and NGC 6251, as a consequence of the Compton humps in their SEDs being much more powerful than the synchrotron humps.

Although radiatively inconspicuous, energetic protons in the lobes may dominate the NT energy density. In Section 3.4.2 we deduced upper limits on the proton content based on current *Fermi*/LAT data, $u_p \lesssim 10$ -40 eV cm $^{-3}$ depending on the lobe (region) and PED spectral index. These limits were obtained without accounting for uncertainties in the EBL and GFL photon densities. Uncertainties in the EBL density arise also from the fact that it is based on large datasets with inhomogeneous error estimates (in addition to other systematic uncertainties, such as redshift-dependent galaxy luminosity functions; Franceschini & Rodighiero 2017). The main EBL components, the CIB and the COB, have $\sim 30\%$ uncertainties (Cooray 2016). A higher/lower COB power implies a lower/higher $N_{e,0}$ if the latter is determined via Compton/EBL modelling of *Fermi*/LAT data (e.g., the S1 region of Cen A); this in turn implies a higher/lower B in the synchrotron fit to the radio spectrum¹⁰. The GFL suffers from observational uncertainties in the galaxy light distribution (Cen A: Dufour et al. 1979; Fornax A: Iodice et al. 2017), and from modeling uncertainties in the monochromatic to bolometric flux correction (e.g., Buzzoni et al. 2006) required to compute the dilution factor of the GFL blackbody model. A case in point is Fornax A, for which our estimate of the GFL photon field density (Chapter 2) was based on nominal magnitude, color, and band-to-band magnitude conversion values adopted from the literature. The resulting nominal Compton/(EBL+GFL) flux slightly exceeds (by $\sim 10\%$, yet within error bars) the nominal *Fermi*/LAT fluxes. As a result, the deduced UL is biased low; correcting for this leads to a weaker bound, $u_p \lesssim 40$ eV cm $^{-3}$ for $q_p = 2.1$.

A lower limit to the proton content may be estimated assuming the lobe internal pressure to exceed the external (ambient) pressure. (Lobes are inflating bubbles in intergalactic space.) Since magnetic fields and relativistic electrons fall short of providing the required internal pressure, protons (NT and thermal) may provide the required pressure. For Cen A (see Table 1 for u_e and u_B) this hypothesis leads to $u_p \gtrsim 5$ eV cm $^{-3}$ (Wykes et al. 2013). The thermal pressure inside the lobes is much smaller: in the S lobe $n_{gas} = (0.9-2.5) \cdot 10^{-4}$ cm $^{-3}$ and $k_B T_{gas} = 0.5$ keV (Stawarz et al. 2013) imply a thermal energy density, $u_{th} = \frac{3}{2} n_{gas} k_B T$, in the range 0.068-0.188 eV cm $^{-3}$. So the above lower limit mainly applies to NT protons and is compatible with our ULs (see Fig. 17).¹¹

In spite of these uncertainties we may compare the estimated limits on u_p with nominal values deduced from the proton to electron energy density ratio, κ , in an electrically

¹⁰ For example if T_5 is taken 9% lower (to mimic a slightly lower COB), then in the Cen A S1 region $N_{e,0}$ and B become, respectively, 25% higher and 10% lower.

¹¹ No information on thermal gas is available for the lobes of Cen B and NGC 6251. As to the latter, the lack of internal depolarization in the NW lobe implies, for a field strength of $B = 0.4$ μ G and no field reversals in the lobe, $n_{gas} < 0.75 \cdot 10^{-4}$ cm $^{-3}$ (see Willis et al. 1978). For Fornax A, $n_{gas} = 3 \cdot 10^{-4}$ cm $^{-3}$ and $k_B T_{gas} = 1$ keV (W lobe; Seta et al. 2013) hence $u_{th} = 0.45$ eV cm $^{-3}$.

neutral NT plasma where both particle species have energy distributions as specified in Sections 3.4.1 (electrons) and 3.4.2 (protons). For $q_p = 2.0$, $q_e = 2.2$ in Cen A's S1, S3 regions, $\kappa \simeq 120$, whereas for $q_p = 2.1$, $q_e = 2.43$ in Fornax A, $\kappa \simeq 110$ (Persic & Rephaeli 2014). The corresponding values of u_e (Table 5) imply nominal values of u_p that are compatible with our estimated ULs.

The result $u_B + u_e + u_p > u_{th}$ is likely to be a more general feature in the energetics of radio lobes. After all, lobes originate in the highly non-equilibrium phenomenon of AGN jets, and their evolution is very different from that of older galactic systems that have attained a state of hydrostatic or virial equilibrium.

3.6 Conclusion

The SED analyses of Cen A, Cen B, and NGC 6251 are quite similar to those of SYMA16, K13 and T12, respectively, who reported and modeled original data for these sources; for Cen A we adopted the separation of each lobe to three rectangular spatial regions defined by SYMA16. However, our treatment is appreciably different from those in previous works in the following respects: (i) we use a single EED, i.e. a truncated PL, throughout – whereas SYMA16 used a generalized exponentially-cutoff PL that did produce analytically different EEDs in different lobe regions, whereas K13 and T12 used broken PLs. Doing so allowed us to make a more direct mutual comparison of the radiative properties of the different lobe regions; (ii) we use a more recent EBL model (Franceschini & Rodighiero 2017; Acciari et al. 2019); and (iii) we fully account for the contribution of the host galaxy to the enhanced radiation field in the lobes. Our results confirm the main conclusions of the earlier analyses and favour a leptonic origin of the NT emission in the three lobe systems; for Cen A, whose SED is spatially resolved, a spectral evolution from the inner to the outer regions is clearly seen. The SEDs of the S1 and S3 regions of Cen A are sufficiently detailed for a spectral analysis to constrain the proton content to within few tens of eV cm^{-3} .

Note. The content of this chapter, except for the speculative section 3.4.3, is published in Persic & Rephaeli (2019b).

REFERENCES

- Abdalla H., et al. (HESS Collab.), 2018, A&A, 619, A71
 Abdo A.A., et al. (*Fermi*/LAT Collab.), 2010, Science, 328, 725
 Acciari V., et al. (MAGIC Collaboration), 2019, MNRAS, 486, 4233
 Ackermann M., et al. (*Fermi*/LAT Collab.), 2016, ApJ, 826:1
 Blandford R., Meier D., Readhead A., 2019, ARAA, 57, 467
 Bregman J.N., Snider B.A., Grego L., Cox C.V., 1998, ApJ, 499, 670
 Buzzoni A., Arnaboldi M., Corradi R.L.M., 2006, MNRAS, 368, 877
 Cooray A., 2016, Royal Society Open Science, 3, 150555
 Crane P., Stiavelli M., King I.R., et al., 1993, AJ, 106, 1371
 Day G.A., Thomas B.M., Goss W.M., 1969, Aust. J. Phys. Astrophys. Suppl., 11, 11
 Dermer C.D., Menon G., 2009, High Energy Radiation from Black Holes (Princeton, NJ: Princeton University Press)
 Dickey J.M., Lockman F.J., 1990, ARA&A, 28, 215
 Dufour R.J., van den Bergh S., Harvel C.A., et al., 1979, AJ, 84, 284
 Finlay F.A., Jones B.B., 1973, Aust. J. Phys., 26, 389
 Franceschini A., Rodighiero G., 2017, A&A, 603, A34 (and Erratum: 2018, A&A, 614, C1)
 Franceschini A., Rodighiero G., Vaccari M., 2008, A&A, 487, 837
 Gil de Paz A., Boissier S., Madore B., et al., 2007, ApJS, 173, 185
 Golombek D., Miley G.K., Neugebauer G., 1988, AJ, 95, 26
 Goss W.M., Shaver P.A., 1970, Aust. J. Phys. Astrophys. Suppl. 14, 1
 Hardcastle M.J., Cheung C.C., Feain I.J., Stawarz L., 2009, MNRAS, 393, 1041
 Harris G.L.H., Rejkuba M., Harris W.E., 2010, PASA, 27, 457
 Haslam C.G.T., Salter C.J., Stoffel H., Wilson W.E., 1982, A&AS, 47, 1
 Iodice E., Spavone M., Capaccioli M., et al., 2017, ApJ, 839:21
 Israel F.P., 1998, A&A Rev, 8, 237
 Jones P.A., Lloyd B.D., McAdam W.B., 2001, MNRAS, 325, 817
 Katsuta J., Tanaka Y.T., Stawarz L., et al., 2013, A&A, 550, A66 (K13)
 Kesteven M.J.L., 1968, Aust. J. Phys., 21, 369
 Komessaroff M.M., 1966, Aust. J. Phys., 19, 75
 Kraft R.P., Vazquez S.E., Forman W.R., et al., 2003, ApJ, 592, 129
 Krawczynski H., Böttcher M., Reimer A., 2012, in Relativistic Jets from Active Galactic Nuclei (eds. M. Böttcher, D.E. Harris, H. Krawczynski; Berlin: Wiley), p.215
 Mack K.-H., Klein U., O'Dea C.P., Willis A.G., 1997, A&AS, 123, 423
 Mathewson D.S., Healey J.R., Rome J.M., 1962, Aust. J. Phys., 15, 354
 McAdam W.B., 1991, Proc. Astron. Soc. Aust., 9, 255
 McKinley B., Briggs F., Gaensler B.M., et al., 2013, MNRAS, 436, 1286
 McKinley B., Yang R., López-Caniego M., et al., 2015, MNRAS, 446, 3478
 Mills B.Y., 1952, Aust. J. Sci. Res. 5, 266
 Mills B.Y., Slee O.B., Hill E.R., 1961, Aust. J. Phys., 14, 497
 Milne D.K., Hill E.R., 1969, Aust. J. Phys., 22, 211
 O'Sullivan S.P., Feain I.J., McClure-Griffiths N.M., et al., 2013, ApJ, 764:162
 Persic M., Rephaeli Y., 2007, A&A, 463, 481
 Persic M., Rephaeli Y., 2014, A&A, 567, A101
 Persic M., Rephaeli Y., 2019a, MNRAS, 485, 2001 (and Erratum: 2019, MNRAS, 486, 950)
 Persic M., Rephaeli Y., 2019b, MNRAS, 490, 1489
 Rephaeli Y., Persic M., 2015, ApJ, 805:111
 Romanishin W., 1986, AJ, 91, 76
 Sanders D.B., Mirabel I.F., 1996, ARAA, 34, 749
 Schreier E.J., Feigelson E., Delvaile J., et al., 1979, ApJ 234, L39
 Schröder A.C., Mamon G.A., Kraan-Korteweg R.C., Woudt P.A., 2007, A&A, 466, 481
 Seta H., Tashiro M.S., Inoue S., 2013, PASJ, 65, 106
 Shaver P.A., Goss W.M., 1970, Aust. J. Phys. Astrophys. Suppl., 14, 133
 Stawarz L., Tanaka Y.T., Madejski G., et al., 2013, ApJ, 766:48
 Sun X.-N., Yang R.-Z., McKinley B., Aharonian F., 2016, A&A, 595, A29 (SYMA16)
 Takeuchi Y., Kataoka J., Stawarz L., et al., 2012, ApJ, 749:66 (T12)
 Tashiro M., Kaneda H., Makishima K., et al., 1998, ApJ, 499, 713
 Willis A.G., Wilson A.S., Strom R.G. 1978, A&A, 66, L1
 Yang R.-Z., Sahakyan N., de Ona Wilhelmi E., Aharonian F., Rieger F., 2012, A&A, 542, A19
 Wilson A.S., Smith D.A., Young A.J., 2006, ApJ, 644, L9
 Wykes S., Croston J.H., Hardcastle M.J., et al., 2013, A&A, 558, A19

4 CHAPTER 4. NT EMISSION IN THE LOBES OF 3C 98, PICTOR A, DA 240, CYGNUS A, 3C 326, AND 3C 236

Abstract. Recent analyses of the broad-band emission SED of extensive lobes of local radio-galaxies have confirmed the leptonic origin of their *Fermi*/LAT γ -ray emission, significantly constraining the level of hadronic contribution. SED of distant ($D_L > 125$ Mpc) radio-galaxy lobes are currently limited to the radio and X-ray bands, hence give no information on the presence of NT protons but are adequate to describe the properties of NT electrons. Modeling lobe radio and X-ray emission in 3C 98, Pictor A, DA 240, Cygnus A, 3C 326, and 3C 236, we fully determine the properties of intra-lobe NT electrons and estimate the level of the related γ -ray emission from Compton scattering of the electrons off the CMB, EBL, and the source-specific radiation fields.

4.1 Introduction

Measurements of NT emission from the extended lobes of radio galaxies provide a tangible basis for modeling of the spectral distributions of energetic particles in these environments. Sampling the SED, even with only limited spatial information, yields valuable insight on the emitting electrons and possibly also on energetic protons whose pp interactions in the ambient lobe plasma and ensuing π^0 -decay could yield detectable $\gtrsim 0.1$ GeV emission. In addition to the intrinsic interest in physical conditions in radio lobes, modeling energetic particles and their emission processes in these environments can yield clues to the origin of NT particles in galaxy clusters.

Currently available spectral radio, X-ray, and γ -ray measurements of the lobes of four radio galaxies have provided an adequate basis for determining the emission processes, the SED of the NT emitting particles, and the mean value of the magnetic field when the superposed photon fields in the lobe region are properly accounted for (Fornax A: Chapter 2; Cen A, Cen B, and NGC 6251: Chapter 3). These SED analyses have confirmed the leptonic origin of the measured lobe *Fermi*/LAT γ -ray emission, constraining the level of hadronic contribution to within several percent.

In the present chapter we extend our SED analysis of radio-galaxy lobes to six relatively distant ($D_L > 125$ Mpc) sources with no available > 0.1 GeV *Fermi*/LAT fluxes: 3C 98, Pictor A, DA 240, Cygnus A, 3C 326, and 3C 236. Lacking γ -ray data, the available spectral measurements enable determination of the electron spectral distribution, but cannot directly constrain NT proton yields. Since the results presented here are based essentially on an identical treatment to that in Chapters 2 and 3, our discussion will be limited only to the most relevant observational data and to the results of our spectral modeling. In Section 4.2 we summarize the observational data and estimates of the radiation field densities in the lobes of the six galaxies. Results of the fitted SED models are detailed in Section 4.3 and discussed in Section 4.4. Our main conclusions are summarized in Section 4.5.

4.2 Emission and radiation fields in the lobes

The six radio galaxies included in this analysis have elliptical hosts and a double-lobe morphology, with (usually) a flat radio lobe surface brightness. In this section we briefly discuss the sources, observations of NT emission, the lobe superposed radiation fields.

4.2.1 Observations of NT emission

3C 98 ($z = 0.0306$; luminosity distance $D_L = 126$ Mpc; Fig.19) shows a double-lobe morphology with a flat surface brightness distribution and a total angular extent of $5' \times 2'$ (Leahy et al. 1997). Broad-band total flux densities from a variety of radio telescopes, compiled in the NASA Extragalactic Database (NED), are listed in Table 6. NT X-ray emission, detected from each lobe, is interpreted as arising from Compton scattering of CMB photons off radio emitting electrons (Isobe et al. 2005; *XMM-Newton* data). We assume a lobe radius $r = 30$ kpc and a galaxy to nearest lobe boundary distance $d = 26.5$ (see Isobe et al. 2005).

Pictor A ($z = 0.0342$; $D_L = 149$ Mpc; Fig.20) shows two symmetrical dim radio lobes with a bright compact hot spot on the far edge of the W lobe (connected with the radio nucleus by a faint jet) and two fainter, less compact spots on the E lobe (Perley et al. 1997). NT X-ray emission from the lobes, detected by Grandi et al. (2003, *XMM-Newton* data) and confirmed in its spatial extension by Hardcastle & Croston (2005, *Chandra* data; see also Hardcastle et al. 2016) and Migliori et al. (2007, *XMM-Newton* data), is interpreted as Compton/CMB radiation. The detected 0.2-200 GeV γ -ray emission is attributed to the jet (Brown & Adams 2012; *Fermi*/LAT data), based on its variability timescale ($\lesssim 1$ yr) and its incompatibility with the (well resolved) radio and X-ray emissions within a synchrotron self-Compton SED model of a prominent compact hotspot in the W lobe. Lobe NT SED data are reported in Table 7. We assume $r = 65$ kpc and $d = 15$ kpc (Perley et al. 1997).

DA 240 ($z = 0.03566$; $D_L = 152$ Mpc; $\theta \sim 35'$; Fig.21), 3C 326 ($z = 0.0895$; $D_L = 395$ Mpc; $\theta \sim 20'$; Fig.23), and 3C 236 ($z = 0.1005$; $D_L = 449$ Mpc; angular extent $\theta \sim 40'$; Fig.24) have 0.326-10.6 GHz data from the entire sources and from their individual components (Mack et al. 1997). NT X-ray emissions, detected from the E lobe of DA 240 and the W lobes of 3C 326 and 3C 236, is interpreted as Compton/CMB radiation (3C 236: Isobe & Koyama 2015; 3C 326: Isobe et al. 2009; DA 240: Isobe et al. 2011 – *Suzaku* data). Lobe SED data for the three sources are reported in Tables 8-10. We assume $r = 400$ kpc and $d = 850$ kpc for 3C 236 (Isobe & Koyama 2014), $r = 225$ kpc and $d = 515$ kpc for 3C 326 (see Ogle et al. 2007 and Isobe et al. 2009), and $r = 268.5$ kpc and $d = 190$ kpc for DA 240 (Isobe et al. 2011).

Cygnus A ($z = 0.0561$; $D_L = 237$ Mpc; Fig.22), with multi-frequency radio (VLA) and X-ray (*Chandra*) emissions available for both lobes separately (Yaji et al. 2010; de Vries et al. 2018), is the brightest radio galaxy in the sky (Birzan et al. 2004). NT X-ray emission from both lobes is interpreted as Compton scattering off the CMB and from synchrotron radiation from the lobes (Yaji et al. 2010; de Vries et al. 2018). Within the relative paucity of data, the lobe SEDs appear to be different, with that of the E-lobe

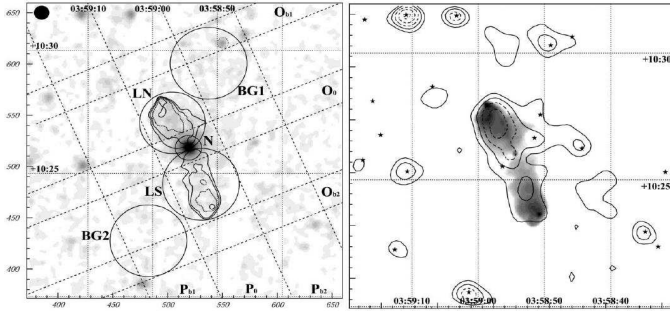


Figure 19. *Left.* Background-inclusive, exposure-uncorrected *XMM-Newton* EPIC MOS+PN image of 3C 98 at 0.2-12 keV (reproduced from Fig. 1 of Isobe et al. 2005). The image is binned into $2''$ and smoothed with a 2-D Gaussian having $\sigma = 5''$. The 4.86 GHz VLA contours are overlaid. Solid-line circles indicate integration regions for the signal (N, nucleus; LN, northern lobe; LS, southern lobe), and background spectra (BG1 with dotted-line circle excluded, and BG2). The filled circle at the top left shows the half-energy width PSF of the MOS and PSF ($r_{\text{PSF}} \sim 15''$). For more information, see Fig. 1 of Isobe et al. (2005). *Right.* EPIC MOS contour image of 3C 98 at 0.2-12 keV overlaid on the 4.86 GHz VLA contours (reproduced from Fig. 2 of Isobe et al. 2005). The image is binned into $10''$ and smoothed with a 2-D Gaussian having $\sigma = 20''$ after subtracting the contributions from the host galaxy and its nucleus. (Neither background subtraction nor exposure correction is performed.) Six contours are plotted in logarithmic scale between 2 and 5 counts per binned pixel. The stars indicate the sources detected in the pipeline data processing, excluding 3C 98.

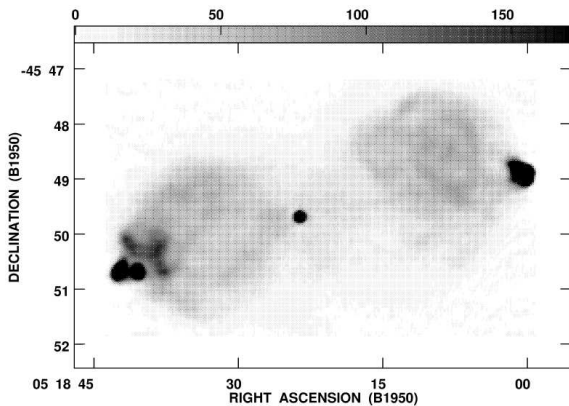


Figure 20. The FR-II radio galaxy Pictor A with its lobes: contours indicate the 20 cm brightness distribution at $7.5''$. Hotspots at the lobes' far ends are clearly visible. (Reproduced from Fig. 3 of Perley et al. 1997.)

steeper/flatter than that of the W-lobe at radio/X-ray frequencies (Yaji et al. 2010; de Vries et al. 2018). Lobe NT SED data are reported in Table 11. We assume $r = 16.3$ kpc and $d = 61.3$ kpc (Yaji et al. 2010).

4.2.2 Radiation fields

A precise determination of the ambient photon fields in the lobes is needed to predict X/ γ -ray emission from Compton scattering of radio-emitting electrons. Radiation fields in the lobes include cosmic and local components.

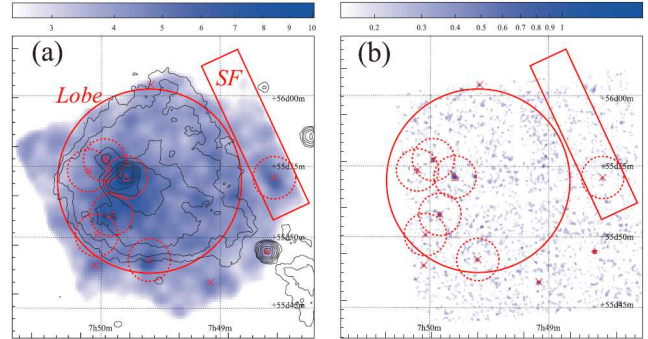


Figure 21. *Left.* Background-inclusive, exposure-uncorrected *Suzaku*/XIS image of the E lobe of DA 240 in the 0.5-10 keV range, heavily smoothed with a 2-D Gaussian with $20''$ radius (reproduced from Fig. 1a of Isobe et al. 2011). The 608.5 MHz radio contours are overlaid. The *Chandra* position of the nucleus (star), hot spot (triangle), and other X-ray point sources (crosses) are also shown. The XIS events in the E lobe and the X-ray background were accumulated within, respectively, the solid circle denoted as "Lobe" and the solid rectangle denoted as "SF" (areas in the dashed circles were removed from the analysis). *Right.* *Chandra*/ACIS image of the same sky field in the 0.3-10 band, smoothed with a 2-D Gaussian with $4''$ radius (reproduced from Fig. 1b of Isobe et al. 2011). Positions of *Chandra* X-ray sources and spectral integration regions for *Suzaku*/XIS are shown like in left panel.

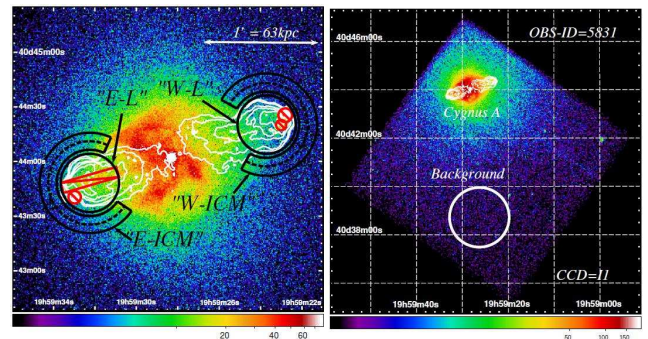


Figure 22. X-ray *Chandra*/ACIS images of Cyg A (reproduced from Fig. 2 of Yaji et al. 2010). *Left.* ACIS image in the 0.7-7 keV band, with 1.3 GHz VLA contour overlaid. The integration regions relevant to spectral analysis are: (i) the areas enclosed by black solid-line circles, i.e. the lobe regions; (ii) the red solid-line circle and rectangle, denoting excluded hotspots and jet regions; and (iii) the areas enclosed by solid-line concentric annuli, i.e. the regions surrounding the lobes. *Right.* Raw ACIS-I1 data of one individual observation (see Yaji et al. 2010 for details), binned into 4×4 ACIS pixels. The 1.3 GHz contour is overlaid. The area enclosed by the solid-line circle denotes the background region.

Cosmic radiation fields include the CMB and the EBL. The CMB is a pure Planckian with $T_{\text{CMB}} = 2.725$ K and energy density $u_{\text{CMB}} = 0.25(1+z)^4 \text{ eV cm}^{-3}$ (e.g., Dermer & Menon 2009). The EBL, originating from direct and dust-reprocessed starlight integrated over the star formation history of the universe (e.g., Franceschini & Rodighiero 2017; Acciari et al. 2019), can be represented as a suitable combination of diluted Planckians (see Chapter 3).

Table 6. Emission from the lobes of 3C 98.

Frequency Log(ν /Hz)	Flux Density [Jy]						
7.167	480 ± 110	7.934	94.3 ± 2.2	8.875	16.7 ± 0.3	9.699	3.29
7.223	420 ± 80	8.204	49.1 ± 6.4	8.875	16.0 ± 0.8	9.699	4.97 ± 0.25
7.301	390 ± 66	8.250	44.0 ± –	9.146	10.2 ± 0.5	9.699	4.94 ± 0.25
7.301	289 ± 29	8.250	48.8 ± 3.9	9.146	10.3 ± 0.3	9.700	4.73 ± 0.31
7.347	312 ± 43.3	8.250	51.4 ± 2.6	9.146	9.75 ± 0.2	9.700	3.39 ± 0.12
7.348	312 ± 30	8.250	35.5 ± 2.8	9.146	9.9 ± 0.5	9.903	3.08 ± 0.07
7.398	260 ± 52	8.250	50.6 ± 2.5	9.146	11.1	10.029	2.82 ± 0.12
7.398	285 ± 34	8.250	47.2 ± 4.7	9.149	12.0 ± 0.3	10.029	3.01 ± 0.13
7.420	215 ± 18	8.502	29.7 ± 1.1	9.423	7.30 ± 0.20	10.362	1.35 ± 0.20
7.420	218 ± 17	8.611	26.9	9.431	7.01 ± 0.35	10.362	1.20 ± 0.12
7.580	147 ± 22	8.611	21.3 ± 0.9	9.431	7.09 ± 0.10	10.519	1.10 ± 0.10
7.580	160 ± 7.2	8.611	24.2 ± 4.6	9.431	7.17 ± 0.35	10.613	0.7 ± 0.2
7.580	173 ± 8.7	8.611	27.5	9.431	6.10	10.795	0.3 ± 0.3
7.778	132 ± 30	8.670	26.7 ± 1.5	9.679	2.70	10.973	0.1 ± 0.5
7.869	98 ± 1.1	8.803	20.9 ± 0.4	9.686	3.13 ± 0.43	17.383	(15.6 ± 2.5) E–9
7.903	90 ± 13	8.875	16.7 ± 0.8	9.686	5.05 ± 0.76		
7.903	83 ± –	8.875	17.7 ± 0.3	9.699	4.93 ± 0.12		

Data: NED (radio), Isobe et al. (2005; X-rays). Unspecified flux errors are assumed to be at the 10% level.

Table 7. Emission from the lobes of Pictor A.

Frequency Log(ν /Hz)	East Lobe [Jy]	West Lobe [Jy]
7.869	237	213
8.515	86.3	94.3
9.166	27.4	32.9
9.699	8.77	12.0
17.383	(55 ± 2) E–9	(55 ± 2) E–9

Data: Perley et al. (1997; radio), Hardcastle & Croston (2005; X-rays – see also Hardcastle et al. 2016). Errors on radio fluxes are assumed to be at the 10% level.

Table 8. Emission from the W lobe of DA 240.

Frequency Log(ν /Hz)	Flux Density [mJy]	Frequency Log(ν /Hz)	Flux Density [mJy]
8.513	10299.0 ± 120.4	9.677	1186.6 ± 23.4
8.785	5688.7 ± 78.1	10.023	749.3 ± 27.8
9.431	1809.6 ± 31.2	17.383	(51.5 ± 7.0) E–6

Data: Mack et al. (1997; radio), Isobe et al. (2011; X-rays).

Local radiation fields (that constitute the GFL) arise from the elliptical host galaxies, whose SEDs usually show two thermal humps, IR and optical.

(i) 3C 98’s host galaxy has a bolometric IR luminosity $L_{\text{IR}} < 4.1 \cdot 10^{43}$ erg s^{–1}, as implied by *IRAS* flux densities at 12, 25, 60 and 100 μ m (Golombek et al. 1988)¹². The optical

¹² The total IR (8–1000 mm) flux is $f_{\text{IR}} = 1.8 \cdot 10^{-11} (13.48 f_{12} + 5.16 f_{25} + 2.58 f_{60} + f_{100})$ erg cm^{–2}s^{–1} (Sanders & Mirabel 1996), where f_{12} , f_{25} , f_{60} , f_{100} are the *IRAS* flux densities at the indicated wavelengths (in μ m).

Table 9. Emission from the lobes of Cygnus A.

Frequency Log(ν /Hz)	East Lobe [Jy]	West Lobe [Jy]
9.129	594 ± 36	429 ± 29
9.231	463 ± 29	357 ± 24
9.656	129 ± 10	122 ± 9
9.699	115 ± 9	108 ± 9
17.383	(71 ± 10) E–9	(50 ± 13) E–9

Data: Yaji et al. (2010; radio), de Vries et al. (2018; X-rays).

Table 10. Emission from the W lobe of 3C 326.

Frequency Log(ν /Hz)	Flux Density [mJy]	Frequency Log(ν /Hz)	Flux Density [mJy]
8.513	1534.6 ± 22.9	9.677	232.1 ± 2.4
8.785	982.5 ± 18.8	10.023	114.1 ± 5.6
9.431	933.6 ± 43.7	17.383	(19.4 ± 4.4) E–6

Data: Mack et al. (1977; radio), Isobe et al. (2009; X-rays).

Table 11. Emission from the W lobe of 3C 236.

Frequency Log(ν /Hz)	Flux Density [mJy]	Frequency Log(ν /Hz)	Flux Density [mJy]
8.513	588.1 ± 22.3	9.677	36.4 ± 14.4
8.785	348.6 ± 18.3	10.023	40.3 ± 16.3
9.431	153.0 ± 18.3	17.383	(12.3 ± 2.8) E–6

Data: Mack et al. (1997; radio), Isobe & Koyama (2014; X-rays).

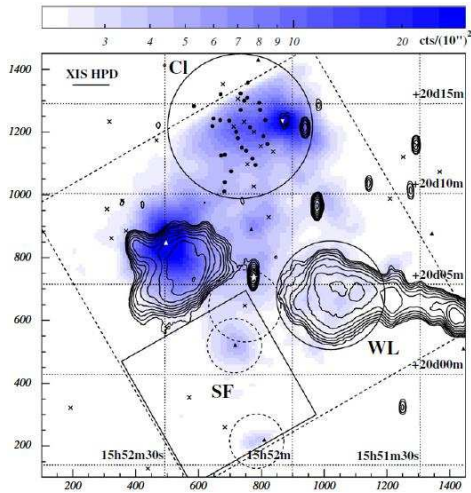


Figure 23. *Suzaku*/XIS image of 3C 326 in the 0.5-5 keV band, smoothed with a 2-D Gaussian with a $20''$ radius, with overlaid 1.4 GHz contours (reproduced from Fig. 1 of Isobe et al. 2009). The scale bar on the top indicates the integrated X-ray counts within a $10'' \times 10''$ bin. The dashed square denotes the XIS FOV. The solid line (top left corner) shows the XIS PSF, with a typical half-power diameter of $\sim 2'$. The white filled star marks the position of the 3C 326 host galaxy. Black crosses, filled circles, black triangles, white (upwards and downwards) triangles indicate various types of source (see Isobe et al. 2009). Signals of the W lobe, source-free region, and the cluster WARP J1552.2+2013 were accumulated from regions "WL", "SL" (with regions in the dotted circles, corresponding to known sources, removed), and "CI", respectively.

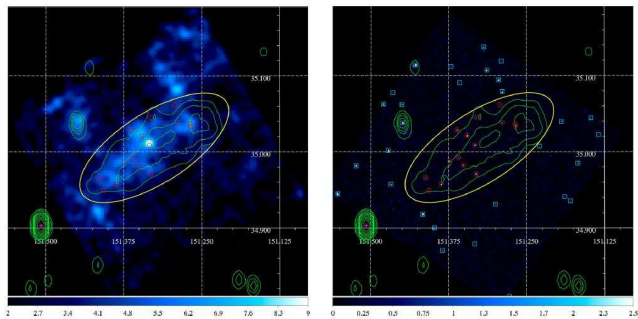


Figure 24. X-ray images of the W lobe of 3C 236 (reproduced from Fig. 1 of Isobe & Koyama 2015). *Left.* Background-inclusive *Suzaku*/XIS image in the 0.5-5 keV band, smoothed with a 2-D Gaussian with a $30''$ radius and uncorrected for exposure, with overlaid the 608.5 MHz radio contour. The scale bar on the bottom indicates the integrated X-ray counts within a $10'' \times 10''$ bin. The XIS spectrum spectrum of the W lobe was accumulated from the solid ellipse. Circles mark the contaminating *Chandra*/ACIS sources, that were taken into account in the XIS spectral analysis. *Right.* Background-inclusive *Chandra*/ACIS image in the 0.5-7 keV band, smoothed with a 2-D Gaussian with a $4''$ radius. The scale bar on the bottom indicates counts within a $2'' \times 2''$ bin. ACIS-detected X-ray sources are indicated with circles and boxes, respectively, inside and outside the elliptical XIS integration region. For more information see Isobe & Koyama (2015).

bolometric luminosity $L_{\text{opt}} \sim 2.3 \cdot 10^{44} \text{ erg s}^{-1}$ is derived from $V = 14.12$ mag (Smith & Heckman 1989a) applying the bolometric correction ($BC_V = -0.85$, Buzzoni et al. 2006), so that $m_{\text{opt}}^{\text{bol}} = V + BC_V$ (see Chapter 2).

(ii) Pictor A's host has $L_{\text{IR}} \sim 1.3 \cdot 10^{44} \text{ erg s}^{-1}$, estimated from the f_{12} , f_{25} , f_{60} (Singh et al. 1990) and f_{100} (inferred from f_{60} , see Lisenfeld et al. 2007) *IRAS* flux densities; and $L_{\text{opt}} \sim 1.2 \cdot 10^{44} \text{ erg s}^{-1}$, estimated from $B = 15.95$, $(B-V) = 0.73$ (from NED) applying the bolometric correction.

(iii) DA 240's host has $L_{\text{opt}} \sim 5 \cdot 10^{45} \text{ erg s}^{-1}$, estimated from $R = 10.7$ mag (Peng et al. 2004) converted to V mag using $(B-V) = 0.90$ ¹³ and applying the bolometric correction. $L_{\text{IR}} \sim 6 \cdot 10^{45} \text{ erg s}^{-1}$ is estimated from L_B through Bregman et al.'s (1998) FIR-B relation assuming $L_{\text{IR}} \sim 2 L_{\text{FIR}}$ (Persic & Rephaeli 2007).

(iv) Cygnus A's host has $L_{\text{IR}} \sim 1.9 \cdot 10^{45} \text{ erg s}^{-1}$ (Golombek et al. 1988), and $L_{\text{opt}} \sim 1.5 \cdot 10^{45} \text{ erg s}^{-1}$ estimated from $V = 13.46$ (total, extinction corrected; Smith & Heckman 1989b) applying the bolometric correction. The IR emission is (Privon et al. 2012) mostly ($\sim 90\%$) torus-reprocessed radiation by an optically obscured ($A_V > 50$ mag, Imanishi & Ueno 2000) AGN (Antonucci et al. 1994; Carilli et al. 2019) with additional contributions from a dust-enshrouded starburst ($\gtrsim 6\%$) and a synchrotron jet ($\lesssim 4\%$).

(v) 3C 326's host has $L_{\text{IR}} \sim 1.3 \cdot 10^{43} \text{ erg s}^{-1}$ (Ogle et al. 2007), and $L_{\text{opt}} \sim 1.2 \cdot 10^{44} \text{ erg s}^{-1}$ derived from L_B which is deduced from $L_{\text{FIR}} \sim 1/2 L_{\text{IR}}$ (e.g. Persic & Rephaeli 2007) through a FIR-B relation (Bregman et al. 1998).

(vi) 3C 236's central galaxy has $L_{\text{IR}} < 4.1 \cdot 10^{43} \text{ erg s}^{-1}$ (see Golombek et al. 1988), and $L_{\text{opt}} \sim 6.9 \cdot 10^{44} \text{ erg s}^{-1}$ derived from $V = 15.72$ mag (Smith & Heckman 1989b) applying the bolometric correction.

These IR and optical parameters allow us to model the GFL; in our calculations we take $T_{\text{gal,OPT}} = 2900 \text{ K}$ and $T_{\text{gal,IR}} = 29 \text{ K}$ (see Chapter 2). The lobe X-ray data are spatial averages, so we correspondingly compute volume-averaged Compton/GFL yields, based on the fact that lobe radii and projected distances (from central galaxies) are much larger than the corresponding central-galaxy radii¹⁴, we treat galaxies as point sources (see Chapter 3).

4.3 Modeling lobe NT emission

Radio emission in the lobes is by electron synchrotron in a disordered magnetic field whose mean value B is taken to be spatially uniform, and X- γ emission is by electron Compton scattering off the CMB and optical radiation fields. The calculations of the emissivities from these processes are standard (see Chapter 2). Assuming steady state, the electron energy distribution (EED) is assumed to be a time independent, spatially isotropic and truncated-PL distribution in the electron Lorentz factor, $N_e(\gamma) = N_{e0} \gamma^{-q_e}$ in the interval $[\gamma_{\text{min}}, \gamma_{\text{max}}]$, with a finite γ_{max} .

In all cases but Cyg A, the photoelectrically absorbed

¹³ www.aerith.net/astro/color_conversion.html

¹⁴ Effective radii estimated from B-luminosities (Romanishin 1986), or isophotal radii (Smith & Heckman 1989a).

¹⁵ 1 keV flux density is used to determine N_{e0} assuming the emission is Compton/CMB. Cyg A is a notable exception because, due to its much higher magnetic field (than the other sources studied here, and in Chapters 2 and 3), as revealed by its very high radio to X-ray emission ratio, the synchrotron energy density in its lobes ($u_s = 0.55$ eV cm⁻³, in the range 10⁵-10¹¹ Hz) exceeds the CMB energy density, such that synchrotron-self-Compton (SSC) radiation contributes to the 1 keV flux even more than that of Compton/CMB. In calculating the SSC yield (see Eq. 18 in Chapter 2) we used an analytical expression for the synchrotron photon density field (deduced from a fit to the radio synchrotron spectrum ¹⁶), $n_s(\epsilon) = N_{s,0} (\epsilon/\epsilon_0)^{-(\alpha+1)} e^{-\epsilon/\epsilon_0}$ cm⁻³ erg⁻¹, with $N_{s,0} = (r_s/c) A_s$ and ϵ_0 the photon energy corresponding to 7 GHz (combined lobes), 6 GHz (E lobe), and 9 GHz (W lobe) and $\alpha = (q_e - 1)/2 = 0.75$. Given $n_s(\epsilon)$ and $n_{\text{CMB}}(\epsilon)$, we determined N_{e0} for Cyg A by fitting the combination of predicted SSC and Compton/CMB emissions to the measured 1 keV flux.

Matching the synchrotron prediction to the radio spectrum yields q_e (from its featureless PL portion) and γ_{max} from the (hint of) spectral turnover at high energies. The minimum electron energy, γ_{min} , can be estimated directly from the 1 keV Compton/CMB data: $\gamma_{\text{min}} = 100$, corresponds to the transition between Coulomb and synchrotron-Compton losses (Chapter 3). With the electron spectrum fully specified, normalization of the predicted synchrotron spectral flux to the radio measurements yields B . The model SED and data are shown in Fig. 25.

As is apparent from Fig. 25, the radiative (synchrotron and Compton) yields of energetic electrons in the lobe SEDs analyzed here account for the currently available radio and X-ray data. This basic result of our spectral analyses strengthens a similar conclusion reached in earlier analyses (see Section 4.2.1).

4.4 Discussion

The main conclusions of our analysis of the lobe SEDs of 3C 98, 3C 236, 3C 326, DA 240, Cygnus A, and Pictor A are quite similar to those presented in earlier papers where the original data for these sources were reported (see Section 4.2.1). However our treatment, presented in Chapter 2, differs appreciably from those in previous analyses. We provide model SEDs for all sources using one simple EED (i.e., a single truncated PL) – whereas previous studies did not explicitly model the SED (3C 98, Isobe et al. 2005; 3C 236, Isobe & Koyama 2015; 3C 326, Isobe et al. 2009; DA 240, Isobe et al. 2011), or did so using a broken PL (Cygnus A, Yaji et al. 2010 and deVries et al. 2018; Pictor A, Hardcastle & Croston 2005). Our essentially uniform treatment allows us

¹⁵ 3C 98: $N_H = 1.17 \cdot 10^{21}$ cm² (Isobe et al. 2005); 3C 236: $N_H = 0.93 \cdot 10^{20}$ cm² (Hardcastle et al. 2016); 3C 326: $N_H = 3.84 \cdot 10^{20}$ cm² (Dickey & Lockman 1990); DA 240: $N_H = 0.49 \cdot 10^{21}$ cm² (Isobe et al. 2011); Cygnus A: $N_H = 0.31 \cdot 10^{22}$ cm² (De Vries et al. 2018); Pictor A: $N_H = 0.42 \cdot 10^{21}$ cm² (Hardcastle & Croston 2005).

¹⁶ The synchrotron emissivity we used to fit the radio flux spectrum is analytically given by $\eta(\nu) = A_s (\nu/\nu_*)^{-\alpha} e^{-(\nu/\nu_*)}$ erg s⁻¹ cm⁻³ Hz⁻¹, with (for total lobe emission) $A_s = 10^{-34.65}$ and $\nu_* = 7$ GHz.

to compare the radiative properties of different lobes more directly and in a less constrained way.

The electron energy density is determined by integration over their spectral distribution with PL index $q_e - 1$ at energies below the characteristic value at which Coulomb losses are roughly equal to radiative losses, $\gamma < \gamma_{\text{min}}$, and with index q_e for $\gamma > \gamma_{\text{min}}$ (e.g., Rephaeli & Persic 2015). In Table 12 we list estimated values of the electron and magnetic energy densities for the lobes under study. The electron to magnetic energy density ratios are in the range $\mathcal{O}(10-100)$, suggesting a particle-dominated NT energy budget in the lobes. As mentioned, we cannot directly constrain proton contents in this lobes (unlike the case of Centaurus A, see Chapter 3), however the energy density of NT protons is probably much higher than that of NT electrons (see Chapter 3 and Persic & Rephaeli 2014). If so, this further substantiates the validity of the result that most of the lobe NT energy density is in energetic electrons and protons.

Our analysis indicates that a GFL contribution to the predicted Compton yields in the *Fermi*/LAT band ¹⁷ is negligible in 3C 236 and 3C 326, dominant in Cyg A, and comparable to the EBL contribution in 3C 98, DA 240, and Pic A. The case of Cyg A is similar to that of Fornax A; in the lobes of both systems the dominant radiation field is the GFL, not the EBL. Note that γ -ray emission from the Fornax A lobes was measured by *Fermi*/LAT (see Chapter 2).

The lobes of Cyg A appear to have somewhat different SEDs, as was already noted (Yaji et al. 2010). In our simple truncated-PL characterization the difference is described by different EED high-energy cutoffs and magnetic fields. The radio spectrum shows a high-end spectral turnover at lower frequency in the E lobe than in the W lobe (Fig. 26). The shortest electron lifetime in the lobes, $\tau = 10^{11} \left(\frac{4}{3} \frac{\sigma_T}{m_e c} \gamma_{\text{max}} \frac{u_{\text{mag}} + u_{\text{syn}} + u_{\text{CMB}}}{u_{\text{CMB}}} \right)^{-1}$ s (for the assumed isotropic electron distribution), is 0.26 Myr in the E lobe ($u_{\text{syn}}^{\text{E}} = 0.75$ eV cm⁻³) and 0.18 Myr in the W lobe ($u_{\text{syn}}^{\text{W}} = 0.37$ eV cm⁻³). If the electron spectrum has attained a steady-state, possibly by *in situ* re-acceleration, then the different lifetimes would imply that the process is more efficient in the W lobe.

The γ -ray emission of Pic A observed by *Fermi*/LAT is unlikely to be related to the radio and X-ray emissions of a prominent compact hotspot in the W lobe because a synchrotron self-Compton SED model linking the emissions in all three bands proves impossible (Brown & Adams 2012). Indeed, the possibility that this γ -ray emission has a diffuse origin in the lobes can essentially be ruled out based on the following considerations: Lobe origin would require an EED normalization, N_{e0} , higher by an order of magnitude than in the no- γ -ray case. Such a high value of N_{e0} would require an unusually high low-energy cutoff, $\gamma_{\text{min}} = 2500$, to account for the 1 keV flux, and obviously a low magnetic field, $B = 0.37$ μ G, to fit the radio spectrum (see Fig. 27). The combination of high N_{e0} and low B would imply $u_e/u_B \sim 1.8 \cdot 10^4$, an unusually high value in radio lobes (see Table 12, and Table 5 in Chapter 3).

The predicted Compton/(EBL+GFL) γ -ray emission in the *Fermi*/LAT band is well below the LAT sensitivity, $\sim 10^{-12}$ erg s⁻¹ at 1 GeV (5σ detection for 10 yr sky-survey

¹⁷ We use projected galaxy-to-lobe distances (inclinations are unknown), so inferred GFL densities are strict upper limits.

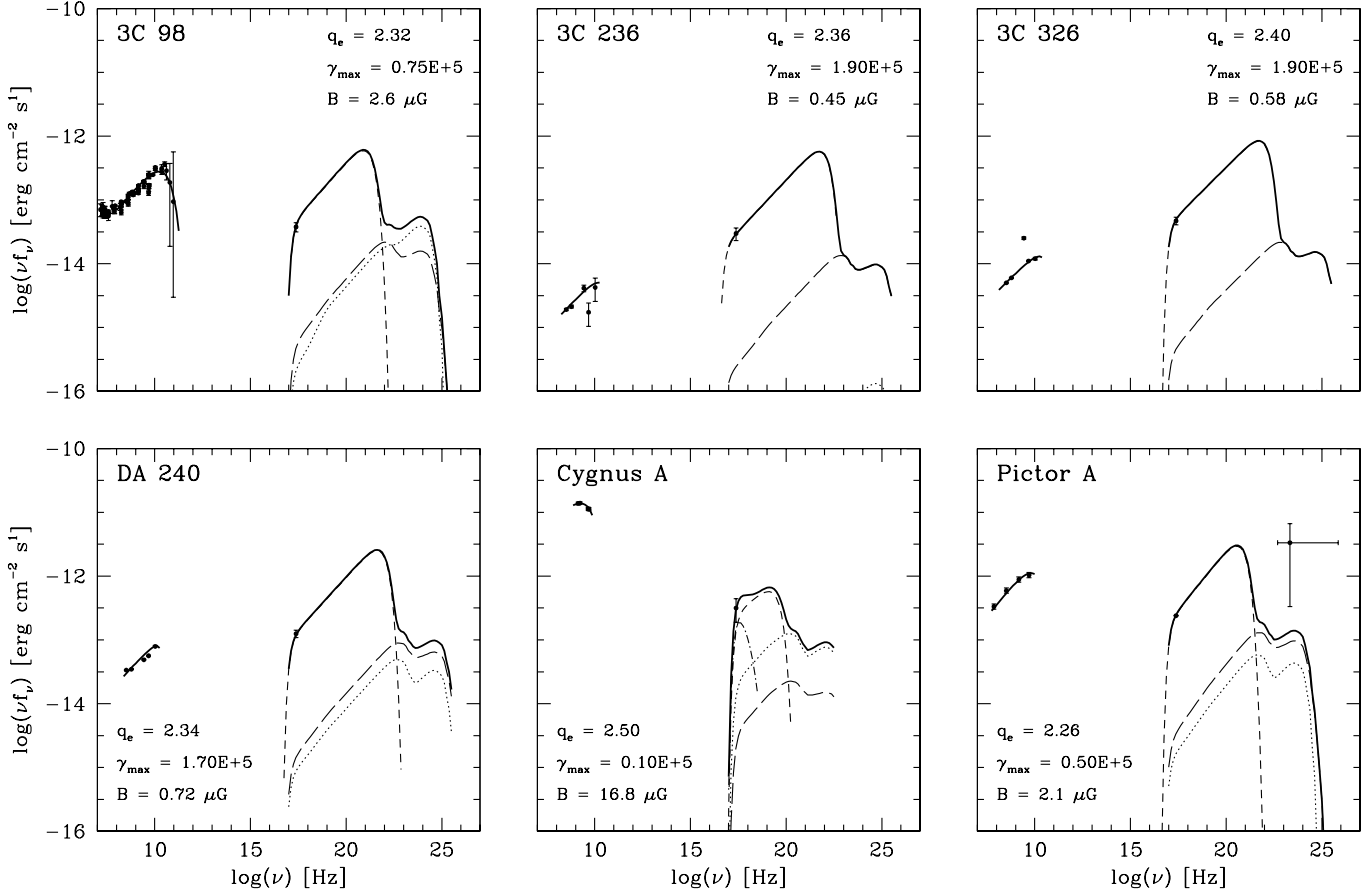


Figure 25. Data are denoted by dots (with error bars). Emission component curves are: synchrotron, solid; Compton/CMB, short-dashed; SSC, dot-dashed (Cyg A); Compton/EBL, long-dashed; Compton/GFL, dotted; total Compton: thick solid. Indicated in each panel are the values of the EED parameters. For Cygnus A we show total lobe SED; the separate lobe SEDs are displayed in Fig. (26). In Pictor A’s SED we also show the lowest detected γ -ray flux (Brown & Adams 2012). Upper limits to IR luminosities (see Section 4.2.2) are treated as nominal IR luminosities.

exposure at high Galactic latitude; Principe et al. 2018) in all cases considered here. The average γ -ray to radio flux ratio, ϕ , at their respective peaks (in νf_ν units) is $\phi \sim 1$ for 3C 236, 3C 326, and DA 240, $\phi \sim 0.1$ for 3C 98 and Pic A, and $\phi \sim 0.01$ for Cyg A; and it is $\phi \sim 1$ for Fornax A, Cen A, Cen B, and $\phi \sim 100$ for NGC 6251 (Chapter 3). Low ϕ -ratios are a consequence of low γ_{max} : for example Cyg A, with $\gamma_{max} = 10^4$ (lowest value in the set), has the lowest ϕ , whereas NGC 6251, with $\gamma_{max} = 1.1 \cdot 10^6$ (highest value in the sample), has the highest- ϕ ; and other sources (e.g., Fornax A, Cen A) with intermediate values ($\gamma_{max} \sim 10^5$) have $\phi \sim 1$. If, hypothetically, the radio data for Cyg A required $\gamma_{max} \sim 10^5$, the predicted γ -ray flux would be $\gtrsim 10^{-12}$ erg s^{-1} at 1 GeV, detectable with *Fermi*/LAT. Thus, it appears that, apart from the obvious geometrical dimming, the predicted very low γ -ray fluxes reflect intrinsic properties of the electron populations in the halos.

Cyg A is of particular interest with regard to the feasibility of γ -ray detection. Due to the low value of γ_{max} the Compton/(EBL+GFL) hump cuts off at $\log(\nu) \sim 22.5$, i.e. ~ 100 MeV, just short of the *Fermi*/LAT range. If so, we would expect any detectable emission above this energy to be of pionic origin. This situation, along with the rel-

atively high value of the thermal gas density in the lobes (Yaji et al. 2010)¹⁸, make the lobes of Cyg A interesting sources of pion-decay γ rays. The issue, of course, is the level of such emission. Consider a proton energy distribution, $N(E_p) = N_{p0}(E_p/\text{GeV})^{-q_p}$ with $q_p = 2.2$ and $E_p^{max} = 50$ GeV. The former value is suggested by considerations of a moderately strong non-relativistic acceleration mechanism ($q_p = (R + 2)/(R - 1)$, with compression ratio $R \sim 3.5$), and of relatively low proton energy losses in the lobe environment (cf. the inelastic pp -interaction cross section in the relevant energy range, $\sigma_{pp} \sim 30$ mbarn; e.g. Kelner et al. 2006). The value of E_p^{max} is not crucial; lower (higher) values in the range ~ 5 -100 GeV just make the pion hump somewhat narrower (broader). The energy density of the relativistic electrons, 1440 eV cm^{-3} , corresponds to a rel-

¹⁸ The lack of internal depolarization in the lobes implies $n_H < 2 \cdot 10^{-4} \text{ cm}^{-3}$, assuming no field reversals in the lobes (Dreher et al. 1987). This results is clearly inconsistent, by 2 orders of magnitude, with the result of Yaji et al. (2010) who fit the X-ray spectra from the Cyg A lobes with a thermal + PL model. As suggested by Yaji et al., the discrepancy could be explained by a tangled field morphology.

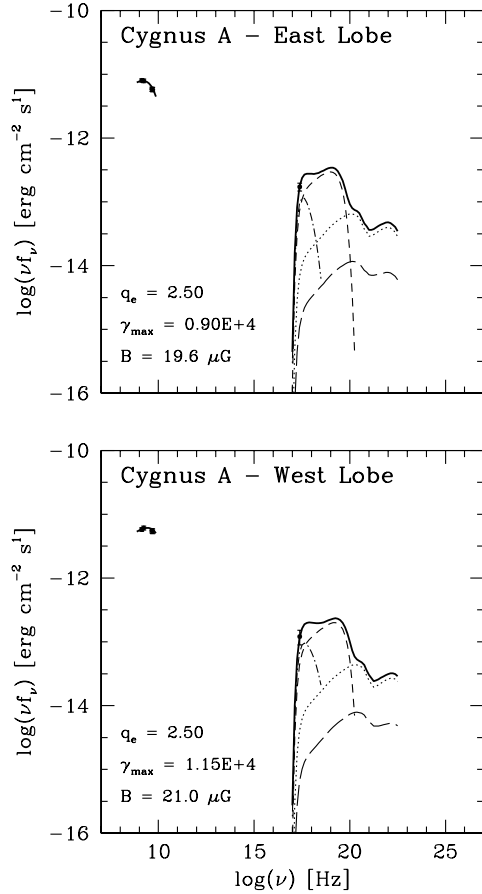


Figure 26. The SEDs of the E lobe (top) and the W lobe (bottom) of Cyg A. Symbols are as in Fig.(25).

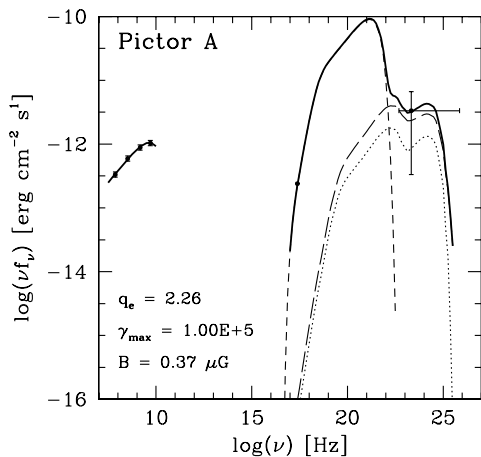


Figure 27. The SED of Pic A assuming the lowest γ -ray flux measured by *Fermi*/LAT (Brown & Adams 2012) is diffuse lobe emission. Symbols are as in Fig. (25).

ativistic electron pressure of $p_e = u_e/3 = 7.7 \cdot 10^{-10}$ dyn cm^{-2} . To this we add the thermal pressure in the lobes, $p_{th} = n_H k_B T = 0.7 \cdot 10^{-10}$ dyn cm^{-2} (from $n_H \sim 1.4 \cdot 10^{-2}$ cm^{-2} and $k_B T = 5.11$ keV; Yaji et al. 2010). As magnetic pressure is negligible, the (spectrally derived) total pressure is $p = p_e + p_{th} = 8.4 \cdot 10^{-10}$ dyn cm^{-2} . The latter value may be compared with the pressure, $p = 8.6 \cdot 10^{-10}$ dyn cm^{-2}

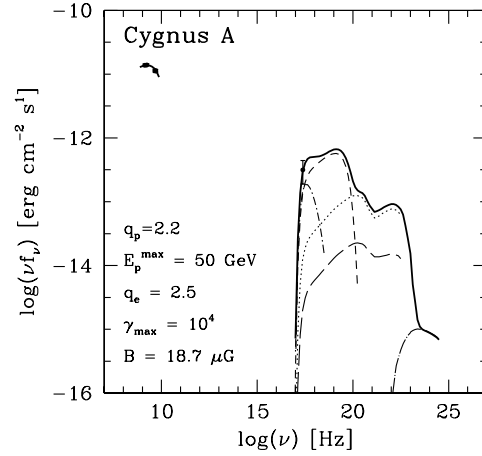


Figure 28. The lepto-hadronic model of the total lobe SED of Cyg A. Data are denoted by dots (with error bars). Emission component curves are: synchrotron, solid; Compton/CMB, short-dashed; SSC, dot-short-dashed; Compton/EBL, long-dashed; Compton/GFL, dotted; pionics, dotted-long-dashed; total Compton and pionics: thick solid. Indicated are the values of the proton and electron spectral parameters.

Table 12. Energy densities (eV cm^{-3}) in the lobes.

$u_{e,B}$	3C 98	3C 236	3C 326	DA 240	Cyg A	Pic A
u_e	19.5	0.044	0.377	0.107	1439	8.21
u_B	0.168	0.005	0.008	0.013	8.70	0.132
$\frac{u_e}{u_B}$	116	8.69	45.0	8.27	165.5	74.3

(Snios et al. 2018), in the surrounding "X-ray cocoon" (a.k.a. "X-ray cavity": Wilson et al 2006) that envelopes Cyg A. Assuming the lobes to be in pressure equilibrium with the cocoon (e.g. Mathews & Guo 2010), we derive a NT proton pressure $p_p = 0.2 \cdot 10^{-10}$ dyn cm^{-2} : the corresponding energy density is $u_p = 3p_p = 30$ eV cm^{-3} . Hence, $N_{p0} = 1.1 \cdot 10^{-8}$ cm^{-3} . The derived low proton content suggests that the relativistic fluid in the Cyg A lobes consists mainly of electron pairs, rather than a relativistic electron-proton plasma (e.g., Mathews 2014). This would indicate that energetic particles were transferred to the lobes by a "light" jet whose matter component consists largely of pair plasma (e.g., English et al. 2016; Snios et al. 2018). The resulting lepto-hadronic model is plotted in Fig. 28, which clearly demonstrates that, even if weak, π^0 -decay emission is likely to dominate emission in the *Fermi*/LAT band.

4.5 Conclusion

Spectral distributions of energetic electrons in lobes of radio galaxies can be directly determined from radio and X-ray measurements. Only weak upper limits can be set on energetic protons when there are no γ -ray measurements of the lobes.

Modeling radio and X-ray measurements from several such lobes (3C 98, Pictor A, DA 240, Cygnum A, 3C 326, and 3C 236 – located at $D_L > 125$ Mpc) as having synchrotron and Compton origin, we fully determine the spectral properties of the emitting electrons.

The main conclusion of the present analysis is that when NT X-ray emission measured for these sources is interpreted as Compton/CMB (including SSC, in the case of Cyg A) radiation, the ensuing SED (leptonic) models are essentially the same as those for sources whose observational SEDs extend to the *Fermi*/LAT γ -ray band (see Chapter 2 and 3). We confirm similar earlier suggestions on the Compton/CMB nature of the diffuse X-ray emission from the original data papers. However, our treatment differs from those in previous analyses: we model all SEDs using a truncated single-PL EED, whereas the earlier studies either did not explicitly model the SED or did so using a broken PL. Our uniform treatment allows us to compare properties of different lobe SEDs in a more unbiased and direct way.

We predict the Compton emission in the lobes using a recent EBL model (Franceschini & Rodighiero 2017; Acciari et al. 2019) and by accounting for the host galaxy contribution to the superposed radiation fields in the lobes. Very low Compton fluxes in the *Fermi*/LAT band are predicted from sources whose radio spectra imply EEDs with low γ_{max} . For Cyg A we predict the Compton emission to be negligible at energies $\gtrsim 100$ MeV, so any detectable emission in this spectral band would be of pionic origin.

Note. The content of this chapter is published as Persic & Rephaeli (2020).

REFERENCES

- Acciari V., et al. (MAGIC Collab.), 2019, MNRAS, 486, 4233
 Antonucci R., Hurt T., Kinney A., 1994, Nature, 371, 313
 Birzan L., Rafferty D.A., McNamara B.R., Wise M.W., Nulsen P.E.J., 2004, ApJ, 607, 800
 Bregman J.N., Snider B.A., Grego L., Cox C.V., 1998, ApJ, 499, 670
 Brown A.M., Adams J., 2012, MNRAS, 421, 2303
 Buzzoni A., Arnaboldi M., Corradi R.L.M., 2006, MNRAS, 368, 877
 Carilli C.R., Perley R.A., Dhawan V., Perley D.A., 2019, ApJ, 874:L32
 Dermer C.D., Menon G., 2009, High Energy Radiation from Black Holes (Princeton, NJ: Princeton University press)
 De Vries M.N., Wise M.W., Huppenkothen D., et al., 2018, MNRAS, 478, 4010
 Dickey J.M., Lockman F.J., 1990, ARA&A, 28, 215
 Dreher J.W., Carilli C.L., Perley R.A., 1987, 316, 611
 English W., Hardcastle M.J., Krause M.G.H., 2016, MNRAS, 461, 2025
 Franceschini A., Rodighiero G., 2017, A&A, 603, A 34 (and Erratum: 2018, A&A, 614, C 1)
 Golombek D., Miley G.K., Neugebauer G., 1988, AJ, 95, 26
 Grandi P., Guainazzi M., Maraschi L., et al. 2003, ApJ, 586, 123
 Hardcastle M.J., Croston J.H., 2005, MNRAS, 363, 649
 Hardcastle M.J., Lenc E., Birkinshaw M., et al., 2016, 455, 3526
 Imanishi M., Ueno S., 2000, ApJ, 525, 626
 Isobe N., Koyama S., 2015, PASJ, 67, 77
 Isobe N., Makishima K., Tashiro M., Hong S. 2005, ApJ, 632, 781
 Isobe N., Seta H., Tashiro M.S. 2011, PASJ, 63, S947
 Isobe N., Tashiro M.S., Gandhi P., et al., 2009, ApJ, 706, 454
 Kelner S.R., Aharonian F.A., Bugayov V.V., 2006, Phys Rev D, 74(3), 034018
 Lisenfeld U., Verdes-Montenegro L., Sulentic J., et al. 2007, A&A, 462, 507
 Leahy J.P., Black A.R.S., Dennett-Thorpe J., et al., 1997, MNRAS, 291, 20
 Mack K.-H., Klein U., O’Dea C.P., Willis A.G., 1997, A&AS, 123, 423
 Mathews W.G., 2014, ApJ, 783:42
 Mathews W.G., Guo F., 2010, ApJ, 725, 1440
 Migliori G., Grandi P., Palumbo G.G.C., et al., 2007, ApJ, 668, 203
 Ogle P., Antonucci R., Appleton P.N., Whysong D., 2007, ApJ, 668, 699
 Peng B., Strom R.G., Wei J., Zhao Y.H., 2004, A&A, 415, 487
 Perley R.A., Röser H.-J., Meisenheimer K., 1997, A&A, 328, 12
 Persic M., Rephaeli Y., 2007, A&A, 463, 481
 Persic M., Rephaeli Y., 2014, A&A, 567, A 101
 Persic M., Rephaeli Y., 2019a, MNRAS, 485, 2001 (and Erratum: 2019, MNRAS, 486, 950) (Paper I)
 Persic M., Rephaeli Y., 2019b, MNRAS, 490, 1489 (Paper II)
 Persic M., Rephaeli Y., 2020, MNRAS, 491, 5740
 Principe G., Malyshev D., Ballet J., Funk S., 2018, A&A, 618, A22
 Privon G.C., Baum S.A., O’Dea C.P., et al., 2012, ApJ, 747:46
 Rephaeli Y., Persic M., 2015, ApJ, 805:111
 Romanishin W., 1986, AJ, 91, 76
 Sanders D.B., Mirabel I.F. 1996, ARAA, 34, 749
 Singh K.P., Rao A.R., Vahia M.N., 1990, MNRAS, 246, 706
 Smith E.P., Heckman T.M., 1989a, ApJ, 341, 658
 Smith E.P., Heckman T.M., 1989b, ApJS, 69, 365
 Snios B., Nulsen P.E.J., Wise M.W., et al. 2018, ApJ, 855:71
 Wilson A.S., Smith D.A., Young A.J., 2006, ApJ, 644, L9
 Yaji Y., Tashiro M.S., Isobe N., et al., 2010, ApJ, 714, 37

5 CHAPTER 5. CONCLUSION

5.1 Discussion

This thesis deals with the NT emission in the lobes of radio galaxies. For all such sources with clear lobe detection and spectral measurements available at radio and X/ γ -ray frequencies, the emitted radiation SEDs have been modeled carrying out exact calculations of all relevant radiative yields in their astrophysical environments. The lobes analyzed here had already been variously studied by groups who published the original data. However, my approach rests on a uniform treatment that includes one same analytic EED for all sources and updated information about the radiation fields in the lobes.

5.1.1 Electrons

Assuming the simplest, truncated single-PL, EED was pivotal to providing a uniform background for SED modeling of all sources. By contrast, earlier studies had not explicitly modeled SEDs or had done so using a broken PL. My synchrotron modeling successfully fit the radio SEDs of all lobes, including the high-frequency cutoffs. High-energy truncation energies were found to be mostly $\gamma_{max} \sim 10^5$, but also as low as $\sim 10^4$ (Cyg A) and as high as $\sim 10^6$ (NGC 6251). Low-energy truncation energies are $\gamma_{min} \sim 10^2$, as estimated from Compton/CMB modeling of the measured NT X-ray emission: given the typical densities of ambient gas and of radiation and magnetic energies prevailing in lobes, this value signals the transition from the synchrotron/Compton-loss regime of the electron spectrum to the Coulomb-loss regime of the electron spectrum.

5.1.2 Radiation fields

Ambient radiation fields in the lobes were accounted for in detail to allow accurate modeling of relevant Compton yields to be made. For isotropic radiation fields (CMB, EBL) a constant intensity was used in the lobe volume. For an anisotropic field (GFL), its variation within the lobe volume was taken into account in the Compton calculations. The EBL model used in this thesis is based on a recent determination based on galaxy counts modified to incorporate a slight optical enhancement suggested by γ -ray data. The GFL model is, obviously, source specific and is based on photometric properties of the lobes' host galaxy. If the latter's size was small compared with the galaxy-to-lobe distance, the galaxy was treated as a point source. If not, a detailed calculation accounting for the field's variation as a function of galactocentric radius was carried out. A case in point is Fornax A, whose central galaxy's (NGC 1316) bright and very extended surface brightness distribution (Iodice et al. 2017) required deprojection and a double volume integration to calculate the average GFL photon energy density in the lobes.

Compton yields could explain γ -ray measurements for all sources with available *Fermi*/LAT data: Cen A (in its spatially sectionalized SED), Cen B, Fornax A, and NGC 6251. The EBL turns out to be more important than the GFL in Cen A, and to be comparable with it in Cen B. The bright,

extended optical light distribution of the host galaxy in Fornax A largely dominates over the EBL, and its Compton yield saturates the LAT data. Finally, the LAT spectrum of NGC 6251 can be modeled as a virtually pure Compton/CMB emission.

5.1.3 Protons

As an important aim of this thesis, I searched the data for quantitative evidence of energetic protons in lobes. (Understanding properties of protons in radio lobes would have important implications also on our understanding of the origin of cluster radio halos.) The spectral signature of hadronically produced (through π^0 decay following pp interactions) radiation occurs at >0.1 GeV γ rays. However, the obligatory Compton/(EBL+GFL) emission appears in that spectral band, too. Thus a detailed account of the latter is crucial to assess the presence of a detectable level of hadronic γ -ray emission.

Due to their proximity, lobe brightness, and adequate SED sampling, Cen A and Fornax A proved to be the most suitable sources for such a study in this thesis. By adequately accounting for the EBL and the GFL, our main result is that the *Fermi*/LAT measurements are, in both cases, consistent with the predicted flux from Compton scattering off the optical radiation field, which is dominated by the EBL in Cen A and by the central galaxy in Fornax A. Thus, our conclusion is that there is no apparent need for an additional hadronic component at a level comparable to current observations. In the case of Fornax A, this conclusion contradicts earlier claims by McKinley et al. (2015) and Ackermann et al. (2016).

Limits on the spectral parameters of NT protons were investigated by assuming a truncated single-PL PED and selecting its spectral index and maximum energy to be close to the values that would be implied from fitting a pionic component to the *Fermi*/LAT data. For Fornax A this consideration suggested $q_p = 2.2$ and $E_p^{max} = 50$ GeV: adding the corresponding pionic component to the Compton yields and gradually increasing it to the point of overproducing the data, an upper limit to the proton energy density was obtained, $u_p \lesssim 10$ eV cm $^{-3}$ – i.e., $\sim 1/5$ of what would be required if the measured γ -ray emission were of pionic origin (45 eV cm $^{-3}$, Ackermann et al. 2016). For Cen A, the shape of the LAT-measured emission clearly reflects the double-hump shape of the EBL: any appreciable pionic component was shown to blur such shape, either by filling the central trough (if $q_p = 2.0$) or by overproducing the low-energy LAT data (if $q_p = 2.8$): either way, $u_p \lesssim 20$ eV cm $^{-3}$. Therefore, only upper limits could be set to the proton contents of lobes from spectral considerations of the γ -ray lobe SEDs.

A potentially interesting case of γ -ray detectability was discussed for Cygnus A. The low γ_{max} in the EED causes the Compton/(EBL+GFL) hump to cutoff at ~ 100 MeV, just short of the *Fermi*-LAT range. However, the thermal gas density is sufficiently high (Yaji et al. 2010) that π^0 -decay yield may be relevant – the pionic hump from decaying π^0 's just straddles the LAT range. The issue is the NT proton content in the lobes. Assuming $q_p = 2.2$ and $E_p^{max} = 50$ GeV (the latter assumption is not crucial), if the lobes are in pressure equilibrium with the surrounding environment the PED normalization is low, $N_{p0} = 1.1 \cdot 10^{-8}$ cm $^{-3}$. Although

weak, this level of π^0 -decay yield still dominates emission in the *Fermi*/LAT band, so any detected flux here would be of pionic origin.

5.1.4 Magnetic fields

Magnetic field intensities were determined as an outcome of spectral fitting. No equipartition (or minimum energy) arguments were used in this thesis because of lack of knowledge of two theoretical pre-requisites to them: (i) the proton to electron energy density ratio, κ , in lobes (that appears in the expression of B_{eq}); and, perhaps even more importantly, (ii) the very applicability of the notion of field vs. particles equipartition to radio galaxy lobes, as it is quite doubtful that lobes even reached any form of equilibrium.

SED modeling returned field intensities in the range $0.4 \leq B/\mu\text{G} \leq 3$ for all lobes – with the notable exception of Cyg A’s high field, $B \sim 20\mu\text{G}$.

5.1.5 Energy densities

Electron energy densities were computed from the $\gamma > \gamma_{\text{min}}$ SED-emitting electrons (spectral index: q_e) and the $\gamma < \gamma_{\text{min}}$ electrons affected by non-radiative Coulomb losses (index: $q_e - 1$; see Rephaeli & Persic 2015). Resulting values of u_e span, across the set of sources studied in this thesis, three orders of magnitude, $0.02 \lesssim u_e/(\text{eV cm}^{-3}) \lesssim 20$ (up to $u_e = 1440 \text{ eV cm}^{-3}$ in Cyg A).

Magnetic energy densities span the range $0.004 \lesssim u_B/(\text{eV cm}^{-3}) \lesssim 0.2$ (up to $u_B \sim 9 \text{ eV cm}^{-3}$ in Cyg A).

The ensuing electron-to-magnetic energy density ratios are in the range $u_e/u_B \sim \mathcal{O}(1-100)$, suggesting a particle-dominated NT energy budget in most lobes. (The only exceptions, $u_e/u_B < 0.5$, are the innermost lobe regions of Cen A.) The energy density of NT protons, although constrained to be $u_p \lesssim \text{few} \times 10 \text{ eV cm}^{-3}$, is probably much higher than that of NT electrons – as suggested by arguments of electric neutrality of the NT plasma at injection and of lobe internal vs. external pressure. Thus we suggest particle dominance in the lobes’ NT energy budget.

Thermal energy densities, earlier deduced from thermal bremsstrahlung emission in the X-ray spectra of the lobes of Fornax A, Cen A, and Cyg A, are generally low, $u_{\text{th}} < 0.5 \text{ eV cm}^{-3}$.

So, this thesis suggests that the condition $u_B + u_e + u_p > u_{\text{th}}$ is probably a general feature in lobe energetics. The main underlying reason may be that lobes originate in the highly non-equilibrium phenomenon of AGN jets, and their evolution is very different from that of older galactic systems (e.g., clusters of galaxies) that have attained a state of hydrostatic or virial equilibrium where thermal energy contrasts gravitation and dominates the internal energy budget.

5.1.6 Accuracy of results

To assess the accuracy of the quantitative results obtained in this thesis we focus on the impact of the main observational and modeling uncertainties. Key parameters are the electron number normalization and endpoints of the energy range, which were determined from radio and X-ray data. Specifically, $N_{e,0}$ and γ_{min} were deduced from the measured

NT 1 keV flux, interpreted as Compton/CMB radiation. Any uncertainty in the NT fraction of the 1 keV flux density directly impacts $N_{e,0}$ – and hence B , through the synchrotron fit to the radio data.

Any uncertainty in the spectral shape of the X-ray data results in some level of parameter degeneracy. For example, different combinations of $N_{e,0}$ and γ_{min} may still reproduce the 1 keV flux density, but other parameters of the radiative model would be affected by the chosen values of those two parameters. E.g., a higher γ_{min} would cause a steeper rise of the predicted $\sim 1 \text{ keV}$ flux, which would call for a correspondingly higher $N_{e,0}$, that would in turn cause a lower magnetic field B .

As to radio data, the value of γ_{max} , constrained by the high-frequency turnover of the radio spectrum, is affected by the observational error on q_e : even in the relatively well sampled radio SED of Fornax A, the relative error on q_e (at 1σ confidence level) turned out to be $\sim 4\%$.

A point worth discussing concerns how our results on protons in lobes are affected by uncertainties in the steps that, in our procedure, have lead to constraining u_p .

(i) In addition to measurement errors, uncertainties in the EBL density arise also from the fact that the latter is based on large datasets with inhomogeneous error estimates (in addition to other systematic uncertainties, such as redshift-dependent galaxy luminosity functions); the main EBL components, the IR and optical humps, have an estimated $\sim 30\%$ uncertainties (Cooray 2016; Franceschini & Rodighiero 2017; Acciari et al. 2019). Furthermore, γ -ray based analyses suggest a slight enhancement of the EBL optical peak. These uncertainties on the EBL have, as a direct consequence, that a higher/lower COB power implies a lower/higher $N_{e,0}$ if the latter is determined via Compton/EBL modelling of *Fermi*/LAT data (e.g., the S1 region of Cen A); this in turn implies a higher/lower B in the synchrotron fit to the radio spectrum.

(ii) The GFL suffers from observational uncertainties in the galaxy light distribution, and from a modeling uncertainty that results from the monochromatic to bolometric flux conversion required to compute the dilution factor of the GFL blackbody model (which describes the optical radiation field sourced by the host galaxy). The bolometric conversion, based on stellar population synthesis models, accounts for a factor of ~ 5 in the estimation of the optical FGL field intensity hence it is crucial for a correct estimation of the Compton yield. A major uncertainty in computing the FGL stems from the unknown inclination of the lobe-to-lobe axis to the line-of-sight to the observer. In this thesis we always used projected galaxy-to-lobe distances: thus the computed FGL energy densities are, strictly speaking, upper limits.

A case in point that illustrates the effect of these uncertainties on the estimated upper limit to the proton density is Fornax A. Our estimate of its GFL photon field density relies on nominal magnitude, color, and band-to-band magnitude conversion values adopted from the literature. The resulting nominal Compton/(EBL+GFL) flux very slightly exceeds (within error bars) the nominal *Fermi*/LAT fluxes. As a result, the formally deduced upper limit, $u_p \lesssim 10 \text{ cm}^{-3}$ is (formally) biased low; correcting for this, results in a weaker bound, $u_p \lesssim 40 \text{ eV cm}^{-3}$ for $q_p = 2.1$.

5.2 Summary

The main conclusions of this thesis (contained in Persic & Rephaeli 2019a, 2019b, 2020) are briefly summarized here.

- We have provided model SEDs for all sources using a truncated single-PL EED. No need has emerged for more complex EEDs. This uniform treatment allowed for an unbiased, direct comparison of the radiative properties of different lobes.
- Values of EED parameters in our resulting SED models are $\gamma_{min} \sim 10^2$, $\gamma_{max} \sim 10^5$, and $B \sim 1\text{--}3 \mu\text{G}$. Outstanding exceptions are the relatively compact lobes of Cyg A ($\gamma_{max} = 10^4$, $B \sim 20 \mu\text{G}$) and the very extended lobe of NGC 6251 ($\gamma_{max} \sim 10^6$, $B = 0.4 \mu\text{G}$).
- Interpreting the measured NT X-ray emission as Compton/CMB (plus SSC if $u_{syn} \sim u_{CMB}$) radiation, and properly accounting for the optical photon fields in the lobes to compute the Compton yields in the *Fermi*/LAT band, the ensuing leptonic radiative models successfully reproduce the lobes' broad-band SEDs from radio to γ rays (in all cases where the latter are available), in agreement with some earlier suggestions. In detail, we conclude that the LAT-measured emissions are dominated by Compton/EBL in Cen A, by Compton/(EBL+GFL) in Cen B, by Compton/GFL in Fornax A, and by Compton/CMB in NGC 6251. The sectionalized SED modeling of each lobe of Cen A reveals a spectral evolution from the inner to the outer regions in the form of an outwardly increasing magnetic field and high-energy EED truncation (the EED spectral index remains constant). Furthermore, modelling the radio/X-ray SEDs of several distant ($D_L > 125$ Mpc) lobes (3C 98, Pictor A, DA 240, Cyg A, 3C 326, and 3C 236) as synchrotron and Compton/CMB radiation (with an SSC contribution in the case of Cyg A), we predict the Compton/(EBL+GFL) γ -ray emission of these sources in the LAT band to be well below the LAT sensitivity. As to Pictor A, we offer an argument, in addition to those already suggested in the literature, against the possibility that the γ -ray emission measured from this source has a diffuse origin in the lobes (instead of a nuclear origin). Lobe origin would require a very high EED normalization and low-energy cutoff and a correspondingly low B , that would imply $u_e/u_B \sim 1.8 \cdot 10^4$, an unusually high value in radio lobes.
- We probed the data for evidence of relativistic protons in lobes. The SEDs of the outermost and innermost regions of Cen A's southern lobe (denoted as S1 and S3, respectively) proved to be sufficiently detailed for a spectral analysis to constrain the proton energy density to within few tens of eV cm^{-3} . A similar limit was found in Fornax A: after fully accounting for the local radiation fields in the lobes, it was found that the Compton/GFL saturates the LAT-measured emission, thus considerably weakening previous published claims of latter's hadronic origin. However, if NT protons comply with our spectrally-deduced upper limits ($u_p \lesssim 20 \text{ eV cm}^{-3}$) and with the lower limits suggested by the lobes' pressure balance with their surrounding medium (e.g., $u_p > 5 \text{ eV cm}^{-3}$ for Cen A; Wykes et al. 2013), they still contain most of the total (NT and thermal) energy density in lobes. Thus, since the thermal energy density is low, $u_{th} < 0.5 \text{ eV cm}^{-3}$ (in sources for which it is known), we conclude that the condition $u_B + u_e + u_p > u_{th}$ probably describes a general feature of lobe energetics, i.e. the latter is dominated

by NT phenomena. Depending on the NT proton content of its lobes, Cygnus A may be an interesting candidate for unambiguous detection of pionic emission, because its (low) Compton yield occurs at energies $\lesssim 0.1$ GeV whereas its estimated π^0 -decay emission straddles the $\sim 0.1\text{--}10$ GeV energy band.

5.3 Outlook

This thesis has used all available SEDs of radio lobes that are resolved at the frequencies of interest. However, the radio spectra of several sources are only sampled sparsely or over a limited bandwidth. When better-quality radio data become available, an updated analysis will help improve the determination of the EED parameters and the magnetic fields. Improved knowledge of the EBL and (mainly for some sources, e.g. 3C 98 and Cyg A) of the host galaxy surface brightness in the optical band would improve the Compton predictions.

A topic worth investigating is the full energy budget of lobes, composed of the total emission radiated over the (estimated) lobe age, the mechanical $p dV$ work done by the intra-lobe plasma against the external pressure to inflate the lobe, and the energies stored in (NT and thermal) particles, magnetic field, and possibly Alfvén plasma waves. Some of these energy components are sparsely discussed in the literature: e.g., $p dV$ work was discussed for Cyg A and Cen A (Wilson et al. 2006; Wykes et al. 2013), thermal energy was discussed for Fornax A and Cen A (Seta et al. 2013; Stawarz et al. 2013), NT energy was discussed in this thesis and in (some of) the cited data papers. A uniform assessment of the issue can provide an integral estimate of the total energy stored in lobes, which may in turn be compared with the total jet energy pumped into them.

One important source is missing from this thesis and still needs attention. Virgo A, a nearby ($D_L = 22.2$ Mpc) radio galaxy associated with the giant elliptical M 87 (see Chapter 1), is a morphologically complex radio source (see Fig. 3). The E lobe is considered to be the result of an ongoing phase of jet activity – whereas the one almost perpendicular to it likely dates to an earlier activity phase (e.g., Blandford et al. 2019). Radio data (De Gasperin et al. 2012) and X-ray data (Belsole et al. 2001) are available for the E lobe, albeit with different extraction regions. At GeV energies, the extraction region of its *Fermi*/LAT-measured γ -ray emission, centered close to the core, encompasses most of the E lobe within its 68% point spread function radius of $3'.2$ (Abdo et al. 2009). The LAT signal is clearly dominated by the jet emission, so estimating the level of emission from the lobe itself is virtually impossible. A fresh analysis of LAT data, with the extraction region centered on the E lobe, would be necessary to gain a better estimate of the lobe emission in that spectral region. At TeV energies, an M 87-centered MAGIC detection has provided spectral data in the 0.1–2 TeV band (Aleksic et al. 2012): although this emission is interpreted as spine/sheath-jet emission, an upper limit to a possible isotropic, much fainter, flux of radiation from the lobe could be estimated within the errors. Given the wealth of data available for this source, comparing detailed radiative and energetic properties of the jet and the lobe could give us valuable information about Virgo A's current outburst.

REFERENCES

- Abdo A.A., et al. (*Fermi*/LAT Collab.), 2016, ApJ, 707, 55
- Acciari V., et al. (MAGIC Collab.), 2019, MNRAS, 486, 4233
- Ackermann M., et al. (*Fermi*/LAT Collab.), 2016, ApJ, 826:1
- Aleksic J., et al. (MAGIC Collab.), 2012, A&A, 544, A96
- Belsole E., Sauvageot J.L., Böhringer H., et al., 2001, A&A, L188
- Blandford R., Meier D., Readhead A., 2019, ARAA, 57, 467
- Cooray A., 2016, Royal Society Open Science, 3, 150555
- De Gasperin F., Orrú E., Murgia M., et al., 2012, A&A, 547, A56
- Franceschini A., Rodighiero G., 2017, A&A, 603, A 34 (and Erratum: 2018, A&A, 614, C 1)
- Iodice E., Spavone M., Capaccioli M., et al., 2017, ApJ, 839:21
- McKinley B., Yang R., López-Caniego M., et al., 2015, MNRAS, 446, 3478
- Persic M., Rephaeli Y., 2019a, MNRAS, 485, 2001 (and Erratum: 2019, MNRAS, 486, 950)
- Persic M., Rephaeli Y., 2019b, MNRAS, 490, 1489
- Persic M., Rephaeli Y., 2020, MNRAS, 491, 5740
- Rephaeli Y., Persic M., 2015, ApJ, 805:111
- Seta H., Tashiro M.S., Inoue S., 2013, PASJ, 65, 106
- Stawarz L., Tanaka Y.T., Madejski G., et al., 2013, ApJ, 766:48
- Yaji Y., Tashiro M.S., Isobe N., et al., 2010, ApJ, 714, 37
- Wilson A.S., Smith D.A., Young A.J., 2006, ApJ, 644, L9
- Wykes S., Croston J.H., Hardcastle M.J., et al., 2013, A&A, 558, A19